

Aerodynamic and Structural Analysis of the Kaman K-16B

A Major Qualifying Project Report
Submitted to the Faculty of the
WORCESTER POLYTECHNIC INSTITUTE
in Partial Fulfillment of the Requirements for the
Degree of Bachelor of Science
in Aerospace Engineering

by

Andrew Carlton
Andrew Carlton

Shannon Daly
Shannon Daly

Elizabeth Healy
Elizabeth Healy

Naoki Heginbotham
Naoki Heginbotham

Cyril Ogbebor
Cyril Ogbebor

Viren Punjabi
Viren Punjabi

Douglas Shirakura
Douglas Shirakura

Akhilesh Yarlagadda
Akhilesh Yarlagadda

March 22, 2024

Approved by:

John J. Blandino

John J. Blandino, Advisor
Professor, Aerospace Engineering Department
Worcester Polytechnic Institute

This report represents the work of one or more WPI undergraduate students submitted to the faculty as evidence of completion of a degree requirement. WPI routinely publishes these reports on the web without editorial or peer review.

Abstract

The Kaman K-16B was an experimental aircraft that was significant in the development of aircraft capable of Vertical or Short Takeoff and Landing (V/STOL). In the 1950s, the K-16B was developed by the Kaman Corporation in partnership with the United States Navy as a prototype to test the ability of a propeller with flaps on each blade, partially tilting main wing, and full-span wing flaps to achieve and improve upon common V/STOL performance problems of the time. The only existing K-16B is stored at the New England Air Museum (NEAM) in Windsor Locks, CT. This work presents a study to evaluate the thrust performance of the K-16B's unique "rotoprops" as well as the induced stresses on the rotoprop blades when operating over a range of blade pitch and collective flap deflection angles. The thrust analysis was performed using a computational fluid dynamic (CFD) simulation whereas the structural analysis was performed using finite element analysis (FEA).

The fact no digital model of the rotoprops exist posed a unique challenge as one had to be created to perform the CFD and FEA. The methodology used to create the solid models used a combination of archival plans, that were photographed and imported into SolidWorks as 2D "sketches," in addition to onsite measurements of key components. These 2D digital sketches were then used to create the 3D geometry for the solid model.

The solid model was imported into Ansys Fluent, where the thrust was evaluated at blade pitch angles of 15, 30, and 45 degrees, collective flap angles of 0 and 13 degrees, and a rotational velocity of 725 rpm. Results support a finding that the K-16B with its tilted wing could have produced sufficient thrust to takeoff over a short distance with the blade pitch set at 30 and 45 degrees, regardless of the collective flap angle. Results also showed that the thrust decreases with collective flap angles of 7 and 13 degrees. These findings are presented and discussed.

For the structural analysis, we calculated the equivalent stresses in simplified rotoprop blade model that included a central, metal actuator control rod with a primary blade structure and collective flap made of spruce. Stresses were evaluated using a combination of static pressure loads, calculated in the Fluent simulations, and centrifugal stresses on the material due to the blade rotation. Considering the combined effects of pitch angle and collective flap angle on the stress

distribution, the least stress-inducing case from the seven cases run was the 30-degree pitch angle and 7-degree collective flap angle. These results, including the location of peak stresses for each case are presented and discussed.

In addition to the results of numerical analysis using CFD and FEA, an analysis of the takeoff performance of the K-16B was attempted using a standard analytical methodology. Despite access to numerous archival reports documenting the aircraft performance and test history, we were not able to locate all the performance coefficients that would be needed to apply the analytical approach to this unique aircraft, specifically because of complexity related to the tilted wing, large wing flaps, and unknown thrust coefficients for the rotoprop.

Finally, we evaluated the use of 3D scanning technology as an alternative approach to create a solid model of structures several feet in length and completed the preliminary design of a translating tripod for blueprints (TTB). The need for a TTB became evident as the team photographed large format blueprints onsite at the museum using a conventional tripod. This work is summarized in the report.

Acknowledgements

On behalf of the entire MQP team, we extend our gratitude to the various parties who helped make this project possible.

- ◆ The New England Air Museum (NEAM) staff, for allowing us to work with them on this project and for helping us access a portion of their extensive and invaluable archive collection. In particular, we would like to thank Carl Cruff, Rick Centore, Lou Palshaw, and Bob Vozzola for their enthusiastic help with handling the K-16B and its rotoprop blade, locating several valuable documents and blueprints, and generally welcoming our team with excitement.
- ◆ Dr. Adrianna Hera, for offering helpful advice when working with Ansys Fluent and for teaching the Ansys introduction classes taken by team members.
- ◆ Nicholas Orlovsky, for meeting with several of our team members and offering valuable insight into running CFD simulations in Ansys Fluent.
- ◆ Most of all, project advisor Professor John Blandino, for guiding the project and providing key insight and guidance. Professor Blandino's advice was crucial for gathering the results, after numerous unsuccessful methods. We are extremely grateful for everything he has taught us, and we will take these lessons with us for all our future endeavors.

Table of Contents

1.	Introduction.....	15
1.1	Project Objectives and Approach.....	16
1.2	Team Structure	17
2.	Background and Literature Review	18
2.1	Kaman K-16B	18
2.2	New England Air Museum.....	24
2.3	Finite Element Analysis	25
2.3.1	Governing Equations for Structural Analysis.....	26
2.3.2	Ansys Static	29
2.4	Computational Fluid Dynamics	30
2.4.1	Ansys Fluent	31
2.4.2	Finite Volume Method.....	31
2.5	Computer-Aided Design (CAD)	34
2.6	3D Scanning	35
3	Methodology for Takeoff Analysis.....	40
3.1	Equations to Calculate Takeoff Distance for K-16B	40
3.2	Implementing Data from Historical Documents	44
3.3	Change in Method to Analyze Takeoff Capabilities.....	49
3.4	Results	52
4	Methodology of Digitally Reconstructing KAMAN K-16B Rotoprop.....	54
4.1	3D Scanner Experimentation	54
4.2	3D Scanner Results	58
4.3	Creating a CAD Model of the Rotoprop	58
4.3.1	Implementing Data from Historical Documents.....	58
4.3.2	Photographing Blueprints	60

4.3.3	Photographing the Kaman K16-B Rotoprop.....	62
4.3.4	Using ImageJ	65
4.3.5	SolidWorks	65
5	Methodology of Computational Fluid Dynamics	70
5.1	Single-Rotoprop Boundary Condition Approach	70
3.5	5.2 Full Rotoprop Rotating Mesh Approach.....	70
5.2.1	Geometry.....	71
5.2.2	Meshing.....	78
5.2.3	Ansys Fluent Simulation Setup.....	91
5.2.4	Full Rotoprop Approach Conclusion.....	98
5.3	Single-Blade Approach.....	100
5.3.1	Geometry.....	100
5.3.2	Creating A Mesh.....	104
5.3.3	Setup	107
5.4	Results.....	111
6	Methodology for the Structural Analysis.....	119
6.1	Practice with Ansys Static and Sample Model	119
6.2	Material Assignment.....	124
6.3	Meshing: Issues and Final Mesh.....	126
6.4	Applied Loads.....	127
6.5	Stress Results and Discussion.....	130
7.	Summary and Recommendations	146
7.1	Project Summary.....	146
7.2	Project Recommendations.....	147
7.3	Team Recommendations	148

8	Conclusion	150
9	References	152
	9.1 General References	152
	9.2 NEAM Archive Sources	155
	Appendices.....	156
	Appendix A: Takeoff Analysis MATLAB Code.....	156
	Appendix B: Preliminary Design of the Translational Tripod for Blueprints (TTB).....	158

Table of Tables

Table 1: Largest Contributors to each Subteam.....	17
Table 2: Variables used in governing equations of CFD.....	32
Table 3: List of identified variables used in takeoff analysis.	41
Table 4: K16-B special characteristics to incorporate into takeoff analysis equations.	43
Table 5. Values obtained from the 1959 and 1967 Kaman K-16B Reports [2] [10].....	47
Table 6: STOL performances obtained from the results portion of 1967 K-16B report [10].....	49
Table 7: Mesh Sizing Used in Each Simulation	105
Table 8: Results of the Single-Blade Thrust with Approximation of Full Rotoprop Thrust	114
Table 9: Moment on the Blade about the Center of Rotation	115
Table 10: Definitions of the parameter cases run for structural analysis.....	131
Table 11: NEAM Archive Sources	156

Table of Figures

Figure 1: K-16B in 40-by-80-foot wind tunnel at the NASA Ames Research Center [21].	21
Figure 2: 3/4 front view of the K-16B in 40-by-80-foot wind tunnel at the NASA Ames Research Center [22].	21
Figure 3: General Arrangement of the final K-16B design from the 1967 report [10], alongside a labeled photo of the rotoprops taken by a team member.	23
Figure 4: Photograph of K-16B in the restoration hangar at NEAM.	24
Figure 5: Degrees of Freedom for 2D beam element [29].	28
Figure 6: Basic diagram of how triangulation scanning works [25] © 2024 Hermary.	36
Figure 7: Diagram of structured light scanning [28] © 2017 ARC Metrologia.	37
Figure 8: Example of a point cloud produced from a Revopoint 3D Scanner [28] © 2023 Revopoint 3D.	37
Figure 9: 1967 report STOL characteristics plot for gross liftoff weight of 12,000 lbs. [10].	48
Figure 10: Bracket tested with 3D scanner on turntable and results of scan on screen.	55
Figure 11: Battery tested on turntable with results of scan on laptop screen.	55
Figure 12: Airfoil tested on turntable with inconsistent scanning results due to concentration displayed.	55
Figure 13: 3D-printed airfoil being scanned on turntable with scan results shown.	55
Figure 14: General arrangement of the K-16B from the 1959 estimated flying qualities report [2].	60
Figure 15: Photo of blueprint showing cross sections of the blade with center of rotation and material structure shown [NA2].	61
Figure 16: Perpendicular view of the underside of the rotoprop blade used to generate the CAD model.	63
Figure 17: Perpendicular view of the leading edge of the rotoprop blade used to generate the CAD model.	63
Figure 18: 45-degree view of the rotoprop blade used as a reference to generate the CAD model.	63
Figure 19: Sample photo of measurement of hinge on flap.	64
Figure 20: Picture of the nose cone.	64
Figure 21: Image of the control surface linkage SolidWorks assembly created using photographs.	66

Figure 22: Image of the planes where airfoil cross-sections were sketched.....	67
Figure 23: Image of the rotoprop blade with collective flap deflection based on blueprint cross sections.	68
Figure 24: Image of the rotoprop hub.....	68
Figure 25: Image of the assembled rotoprop.....	68
Figure 26: Image of the simplified rotoprop blade.....	68
Figure 27: Isometric View of the rotoprop in Ansys Design Modeler.....	71
Figure 28: Tree Outline of the geometry in the Ansys user interface.....	72
Figure 29: Cylinder Generation over the Rotoprop.....	73
Figure 30: Cylinder Generation Details View in the Ansys user interface.....	74
Figure 31: Box Enclosure containing the rotoprop and cylinder.....	74
Figure 32: Box Enclosure Details View.....	75
Figure 33: Rotating Domain Boolean.....	76
Figure 34: Rotating Domain Detail View in the Ansys user interface.....	76
Figure 35: Static Domain Boolean.....	77
Figure 36: Static Domain Boolean Detail View in the Ansys user interface.....	77
Figure 37: Final Design Modeler Tree Outline in the Ansys user interface.....	78
Figure 38: Inserting Face Sizing in the Ansys user interface.....	79
Figure 39: Face Sizing Geometry.....	79
Figure 40: Face Sizing Detail View in the Ansys user interface.....	80
Figure 41: Mesh Detailed View in the Ansys user interface.....	80
Figure 42: Mesh Isometric Section View.....	81
Figure 43: Mesh Section View.....	82
Figure 44: Ansys Meshing Quality Worksheet 1 in the Ansys user interface.....	82
Figure 45: Ansys Meshing Quality Worksheet 2 in the Ansys user interface.....	82
Figure 46: Ansys Fluent Meshing Start Up in the Ansys user interface.....	84
Figure 47: Ansys Fluent Meshing Import Geometry in the Ansys user interface.....	84
Figure 48: Face Sizing Detail View in the Ansys user interface.....	85
Figure 49: Generated Surface Mesh.....	86
Figure 50: Generated Surface Mesh Section Plane.....	86

Figure 51: Fluent Meshing Describe Geometry in the Ansys user interface.	87
Figure 52: Fluent Meshing Update Boundaries in the Ansys user interface.	88
Figure 53: Fluent Meshing Update Regions in the Ansys user interface.	89
Figure 54: Fluent Meshing Adding Boundary Layers in the Ansys user interface.	90
Figure 55: Generated Volume Mesh and Quality in the Ansys user interface.	91
Figure 56: General Solver Setup.....	92
Figure 57: Viscous Model Definition.	92
Figure 58: Fluent Setup Materials in the Ansys user interface.	93
Figure 59: Fluent Setup Cell Zone Conditions in the Ansys user interface.....	93
Figure 60: Boundary Conditions Setup in the Ansys user interface.	94
Figure 61: Report Definitions Setup in the Ansys user interface.	95
Figure 62: Solution Models Setup in the Ansys user interface.....	96
Figure 63: Fluent Simulation Initialization in the Ansys user interface.	97
Figure 64: Run Simulation Setup in the Ansys user interface.	97
Figure 65: Ansys Meshing Thrust Solution.....	98
Figure 66: Fluent Meshing Solution Error.....	99
Figure 67: Ansys Fluent Terminated Solution.....	99
Figure 68: Top-Down View of Setting the 30° Blade Pitch relative to the root.....	101
Figure 69: Dimensions of the Enclosure Sketch.....	102
Figure 70: Extruded Enclosure	103
Figure 71: Final Geometry of the Simulation with the Top Face Hidden	104
Figure 72: Bottom Face of Accurately Meshed Blade set at 30° Pitch and 0° Flap Angles.....	106
Figure 73: Example of Successfully Meshed Full Enclosure	106
Figure 74: Frame Motion Options under Cell Zone Conditions in the Ansys user interface.	108
Figure 75: Boundary Condition Options for the Inlet.....	109
Figure 76: Standard Initialization Window Computed from the Inlet.....	110
Figure 77: Sample “Run Calculation” Window.....	111
Figure 78: Force vs. Iterations Plot for the Blade at the 30° Pitch and 7° Flap Angles	112
Figure 79: Force vs. Iterations Plot for the Blade at the 30° Pitch and 13° Flap Angles	112
Figure 80: Pressure Contours of the Blade at the 15° Pitch and 0° Flap Angles.....	116

Figure 81: Pressure Contour of the Blade at 30° Pitch and 13° Flap Angles	117
Figure 82: Pressure Contour of the Blade at 45° Pitch and 13° Flap Angles	117
Figure 83: Mesh used for sample model in practice static analysis.....	120
Figure 84: Uniform pressure load applied to sample model in practice static analysis.....	120
Figure 85: Single-part model of flap used to test deformation in Ansys Static.....	121
Figure 86: Rotational velocity load applied to sample blade model in practice static analysis.....	122
Figure 87: Fixed support applied to sample model during practice static analysis.	123
Figure 88: Von Mises stress plot for practice static analysis.....	123
Figure 89: Material properties of spruce inputted into Ansys Static engineering data.....	125
Figure 90: Elastic properties of spruce added to Ansys Static engineering data.	126
Figure 91: Meshed model of single blade including linkage in Ansys Static.....	127
Figure 92: Fixed support load applied to proper blade face on the 0-degree flap deflection model in Ansys Static.	128
Figure 93: Imported static pressure distribution from Fluent in Static for 15° pitch angle and 0° flap angle parameter case.....	129
Figure 94: Rotational velocity of 75.9 radians per second applied 0.313 meters from fixed face of blade.	130
Figure 95: Von Mises stress contour plot without flap shown for 15° pitch angle and 0° flap angle case with a case-unique contour.	132
Figure 96: Von Mises stress contour plot of blade with flap (top and bottom surfaces) for 15° pitch angle and 0° flap angle case with a case-unique contour.	132
Figure 97: Von Mises stress contour plot focused on rod for 15° pitch angle and 13° flap angle case with a case-unique contour.	133
Figure 98: Von Mises stress contour plot of blade (top and bottom surface) for 15° pitch angle and 13° flap angle case with a case-unique contour.....	133
Figure 99: Von Mises stress contour plot focused on rod for 30° pitch angle and 0° flap angle case with a case-unique contour.	134
Figure 100: Von Mises stress contour plot of blade (top and bottom surface) with flap for 30° pitch angle and 0° flap angle case with a case-unique contour.	134
Figure 101: Von Mises stress contour focused on rod for 30° pitch angle and 7° flap angle case with a	

case-unique contour.	135
Figure 102: Von Mises stress contour of blade (top and bottom surface) with flap for 30° pitch angle and 7° flap angle case with a case-unique contour.	135
Figure 103: Von Mises stress contour without flap shown for 30° pitch angle and 13° flap angle case.	136
Figure 104: Von Mises contour plot for blade (top and bottom surface) for 30° pitch angle and 13° flap angle case.	136
Figure 105: Von Mises stress contour plot without flap shown for 45° pitch angle and 0° flap angle case with case-unique contour.	137
Figure 106: Von Mises stress contour plot of blade (top and bottom surface) for 45° pitch angle and 0° flap angle case with case-unique contour.	137
Figure 107: Von Mises stress contour plot without flap shown for 45° pitch angle and 13° flap angle case with case-unique contour.	138
Figure 108: Von Mises stress contour plot of blade (top and bottom surface) for 45° pitch angle and 13° flap angle case with case-unique contour.	138
Figure 109: Von Mises stress contour plot of blade top and bottom surface for 15° pitch angle and 0° flap angle case with uniform contour.	139
Figure 110: Von Mises stress contour plot of blade top and bottom surface for 15° pitch angle and 13° flap angle case with uniform contour.	139
Figure 111: Von Mises stress contour plot of blade top and bottom surfaces for 30° pitch angle and 0° flap angle case with uniform contour.	139
Figure 112: Von Mises stress contour plot of blade top and bottom surfaces for 30° pitch angle and 7° flap angle case with uniform contour.	140
Figure 113: Von Mises stress contour plot of blade top and bottom surfaces for 30° pitch angle and 13° flap angle case with uniform contour.	140
Figure 114: Von Mises stress contour plot of blade top and bottom surfaces for 45° pitch angle and 0° flap angle case with uniform contour.	140
Figure 115: Von Mises stress contour plot of blade top and bottom surfaces for 45° pitch angle and 13° flap angle case with uniform contour.	141
Figure 116: Von Mises stress results with no pressure applied for fifteen-degree pitch angle and zero-	

degree flap angle 143
Figure 117: Alternate View of Model with Mount 159

1. Introduction

The Kaman K-16B was an experimental aircraft that was significant in the development of aircraft capable of Vertical or Short Takeoff and Landing (V/STOL). In the 1950s, the K-16B was developed by the Kaman Corporation in partnership with the United States Navy as a prototype to test the ability of a propeller with flaps on each blade, partially tilting main wing, and full-span wing flaps to achieve and improve upon common V/STOL performance problems of the time [10]. However, after limited wind tunnel and tethered testing, this initiative was abandoned, and the K-16B project was canceled before the first test flight could be completed.

Currently, the only example of the K-16B built resides in the New England Air Museum (NEAM) in Windsor, CT. The museum is currently working on restoring the K-16B for preservation purposes and is currently located in the museum's restoration hangar. The museum staff is restoring the prototype to seal and preserve the aircraft for outdoor display until a full restoration is possible. A lingering question after the cancellation of the project is whether the K-16B could have taken off in a short distance, demonstrating its V/STOL capabilities as originally intended. Attempting to answer this question through analysis was the first goal of the present project. Answering this question required an analysis of the thrust produced by the aircraft's unique "rotoprops" (a hybrid rotor and propeller) over a range of operating conditions. Estimating this thrust was a second goal for the project.

Additional goals for this project were to provide the NEAM staff with an assessment of the structural and aerodynamic capabilities of the K-16B, which implies an in-depth analysis of the aircraft's rotoprops. By creating a Computer-Aided Design (CAD) model of the rotoprops, the team was able to simulate various operational conditions using computational fluid dynamics (CFD), implemented with the commercially available Ansys Fluent suite of software. In addition, the rotoprops were investigated using Finite Element Analysis (FEA) to evaluate the stress distribution under different loading conditions. This was implemented using the Ansys Workbench software suite. The methodology and findings of this work are presented in this report, including the team's answer to the question of whether the K-16B would have been able to successfully take flight.

1.1 Project Objectives and Approach

Goal 1: Assess whether the aircraft could have achieved takeoff and flight over a short distance as originally intended.

Objective 1: Accurately model the aircraft's take-off performance.

Goal 2: Evaluate the thrust capability of the rotoprops over a range of operating conditions.

Objective 1: Collect and understand information on the K-16B rotoprops and review propeller theory.

Objective 2: Define the range of rotoprop operating conditions, e.g. RPM, pitch, actuator deflection, etc. the team will examine and analyze.

Objective 3: Investigate and understand the wing and rotoprop control system used on the aircraft.

Objective 4: Investigate and understand the tilt-wing system and theory of operation.

Goal 3: Evaluate the induced stresses throughout a rotoprop blade over a range of operating conditions.

Objective 1: Perform Finite Element Analysis on the blade structure.

Objective 2: Investigate the design and operation of the control surface used on the rotoprops and estimate the aerodynamic loads on the control surface during operation.

Goal 4: Evaluate the efficacy of 3D scanning as part of a workflow to generate solid models and fabricate any missing parts needed for restoration.

Objective 1: Learn to use the Revopoint Pop 2 3D scanner.

Objective 2: Evaluate reversible methods to maximize the reflectivity of the object.

Objective 3: Generate CAD models from scans.

Objective 4: Design digital models to replicate missing or damaged parts for NEAM.

Goal 5: Provide students with specialized training in and the opportunity to apply software tools, MATLAB and the Ansys Workbench suite - Ansys Static Structural and Ansys Fluent.

Objective 1: Take SESA for research training seminars to learn software.

Objective 2: Learn and adjust software techniques as the team gains experience throughout the project.

1.2 Team Structure

To best accomplish the goals and objectives stated above, the team decided to split into subteams that would each focus on a specific goal. There were originally four subteams created to focus on creating the CAD models, conducting CFD simulations, conducting structural analysis, and analyzing the takeoff capabilities of the Kaman K-16B. The Historic Research subteam was created as it became increasingly clear that historical accuracy, proper understanding of how the aircraft operates, and understanding the failures experienced by the original development program in the 1950s was important to defining test conditions for the simulations undertaken as part of this work. The students in each subteam are shown in Table 1.

Subteams	Largest Contributors
CAD	Cyril Ogbebor & Akhilesh Yarlagadda
CFD	Andrew Carlton & Douglas Shirakura
Historic Research	Shannon Daly
Structural Analysis	Elizabeth Healy & Shannon Daly
Takeoff Analysis	Shannon Daly, Elizabeth Healy, Naoki Heginbotham, Cyril Ogbebor

Table 1: Largest Contributors to each Subteam

2. Background and Literature Review

One of the project goals was to accurately model the capabilities of the K-16B. The use of engineering reports and incomplete historical data collection combined with the capabilities of modern simulation software allowed the team to complete this goal. The inclusion of two elements is imperative within the team's methodology. Firstly, a comprehensive understanding of the K-16B's design, aircraft testing procedures, and the decision to discontinue the project by the United States Navy is essential. Secondly, a thorough comprehension of the tools required for various project aspects and simulations is necessary. For instance, the application of Finite Element Analysis (FEA) emerges as a pivotal tool enabling the analysis of fluid dynamics and structural integrity of the rotors, crucial to the K-16B's takeoff performance. Background knowledge concerning the effective utilization of tools such as FEA for the K-16B informed the team's approach, culminating in a well-informed determination regarding the K-16B's takeoff capabilities.

2.1 Kaman K-16B

Charles Kaman, the founder of the Kaman Corporation, sought to push the boundaries of helicopter design. As an established and award-winning aerospace engineer, Kaman's work with experimental concepts in helicopter technology and pioneering designs was integral in creating the modern idea of the helicopter and similar aircraft [19]. Kaman was responsible for the design of several innovative helicopters, including the experimental K-225 which utilized intermeshing rotors, an example of which can be seen in the NEAM collection [18]. As defined in the Egerton and Fitzpatrick report from 1967, V/STOL aircraft are designed to bridge the gap between the capabilities of conventional aircraft and helicopters [10]. A V/STOL aircraft was sought by Kaman that would fill the gap between short hover capabilities including the ability to withstand winds at or above 30 knots, and cruise below 400 knots [10].

An initial design proposal was created for a V/STOL rotor concept that would solve the problems that the V/STOL concepts of the time were facing. The concept the team developed was

implementing flaps on each blade to provide normal propeller blade efficiency at cruise conditions (non-deflected), and an increased camber at V/STOL and hover conditions [10]. This combines the different intended design characteristics for each mission into one design that can transform to suit the needs of its current operating condition.

After the development of the concept, named the rotoprop, a proposal was submitted by Kaman Corporation to the Navy Air System Command on the 20th of September 1955. Impressed by the submitted proposal, a contract between the Navy and Kaman was created which called for whirl stand testing¹ of a single rotor-propeller (rotoprop) prototype [6]. Satisfied with the successful test results, the contract was amended to cover a more sophisticated concept evaluation including a ground test. The test program included load and stress analyses of the transmission mount structure and the drive system and a torsional dynamic analysis of the drive system. The ground test included the consideration of the rotoprop/nacelle/wing/flap combination [6]. This test was also successful and encouraged the Navy to fund the project to proceed with developing a full-scale research vehicle in June 1958. With the full-scale research vehicle, the Navy became interested in the dynamic operation of the rotor along with the power and drive system.

Under contract NOa(s) 56-549c given by the Air Systems Command, Department of the Navy [24], the development of a propulsive rotor suitable for V/STOL was initiated by the Kaman Corporation using their internal funding [6]. The design, which later became the Kaman K16-B, consisted of two, three-blade rotoprops, each powered by General Electric YT58-GE8 turboshaft engines mounted on a tilting wing [10]. The fuselage for the prototype was taken from a JRF-5 Grumman Goose. The use of two counterrotating rotoprops counteract each other's rotational torque on the structure, which negates the need for a tail rotor when producing vertical thrust as required on conventional helicopters.

This aircraft was designed to test the feasibility of a control surface (in this case, a blade flap) on each blade to allow for camber to vary as flight conditions change, while improving both

¹ Whirl stand testing allows for centrifugal testing helicopter rotors or propellers where the rotor hub is mounted on a tower and rotated at a certain RPM [25].

efficiency in cruise flight, and maximum thrust and controllability in a hover without added power or control systems [10]. In the final report of the K-16B written by Egerton and Fitzpatrick in 1967, the authors refer to this blade flap in many different ways, most broadly as the blade flap, while when referring to the specific control inputs the flaps are either referred to as the collective flaps or the cyclic flaps to avoid confusion; for consistency they will be referred to the same way as they appear in the report from 1967 [10]. The collective flap and the cyclic flap are the same control surface (the blade flap). The deflections of the collective flaps reduce the necessary rotational speed and increase the mean coefficient of lift without stalling the blades [10]. The collective flaps are operated by the collective, which like a helicopter deflects the flap on each blade by the same angle, changing the camber of the blades to decrease necessary rotational speed, change the stall angle, and therefore increase thrust capabilities [10]. The cyclic flaps are simultaneously operated by a cyclic control system to provide control moments [10]. “Cyclic deflection of the flaps results in cyclic lift control in a manner duplicating the hovering control of a helicopter” [10]. In a more common helicopter configuration, the rotor blades have no flaps, and the collective rotates each blade at the same angle, and the cyclic provides the control moments by rotating each blade accordingly. The major difference between a standard helicopter operation and the K-16B concept rotoprops is that a helicopter operates by imposing control moments and collective control by adjusting the angle of attack of its rotor blades, but the K-16B’s rotoprops induced control moments and collective control through adjusting the blade’s camber.

After the full-scale K-16B was built, a functional tie-down test was performed on the aircraft, it was then shipped to NASA Ames Research Center for full scale wind tunnel testing. Here, a static thrust stand testing was performed on the aircraft in a 40-foot x 80-foot wind tunnel, as shown in Figure 1 and Figure 2 [6].

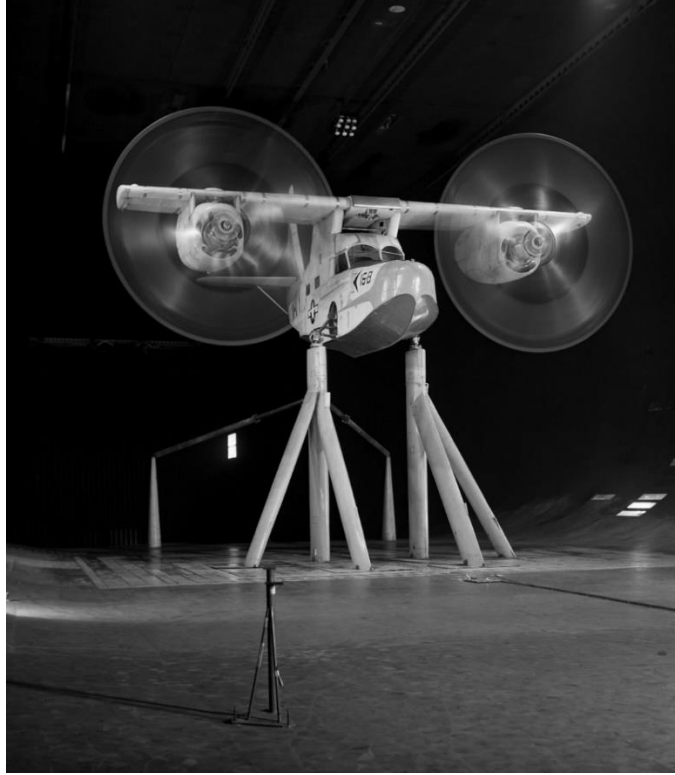


Figure 1: K-16B in 40-by-80-foot wind tunnel at the NASA Ames Research Center [21].



Figure 2: 3/4 front view of the K-16B in 40-by-80-foot wind tunnel at the NASA Ames Research Center [22].

Following the wind tunnel test at the NASA Ames Research Center, the development of the K-16B concept was terminated in 1962 due to several problems found during the program. “The configuration tested proved to have insufficient thrust for vertical flight as its instrumented test gross weight; lateral and directional control power was deficient; severe wing and horizontal tail stall were encountered in portions of the transition region; and a number of detail design deficiencies became evident” [10]. Testing also uncovered “several mechanical problems, principally with oscillating bearings in the blade-flap control system” [10]. Further, the compatibility issues substantially encouraged the discontinuation of funding due to the consistency of these problems from the beginning of the project [6]. Additionally, the development of a second-generation V/STOL aircraft caused funding limitations that prevented the flight research from continuing. The XC-142A was a constructed and tested prototype developed by the US Army, Navy, and Air Force during the 1960s [8]. Along with the Bell X-22, a tilted-duct aircraft that the Navy developed in the 1960s [3], the funds for the K-16B project were substantially limited [10]. The project was subsequently canceled by the US Navy in 1962 [6]. Although the K-16B never had a first flight, key design elements that were integrated into the K-16B and tested during the development of this aircraft can be seen in today’s V/STOL aircraft, such as the tiltrotor concept in the Osprey aircraft.

Basile, Fitzpatrick, and Zon in February 1959 prepared an estimated flying qualities report (number G-113-4) that presents the calculated performances of the K-16B in hover and transitional flight, as well as high speed conditions [2]. Transitional flight is where the aircraft is between a hover and fixed wing configuration where both styles of flight controls are used (helicopter and conventional airplane controls) [2]. This report is one of the many reports created during the project which reflects some differences from the final test model of the K-16B that can be seen at NEAM. This does however give a detailed view of the theory of the time that was employed to predict real life behaviors of the K-16B.

Egerton and Fitzpatrick in 1967 wrote the final summery report (number G-113-36) of the research and development of the K-16B [10]. This document details the final configuration, analysis, test results and conclusions after the cancelation of the contract. The most up to date assumptions, dimensions and performances are in this report. The document is of suboptimal

quality, resulting in segments that are illegible or low enough quality that values, or information are uncertain. One example of this poor quality is the final General Arrangement schematic shown in Figure 3. To add some clarity to the schematic and the terminology of this report, we added a photo of the rotoprops blade taken in storage with the various parts labeled; note that each of the two rotoprops mounted on either wing contain three of these blades.

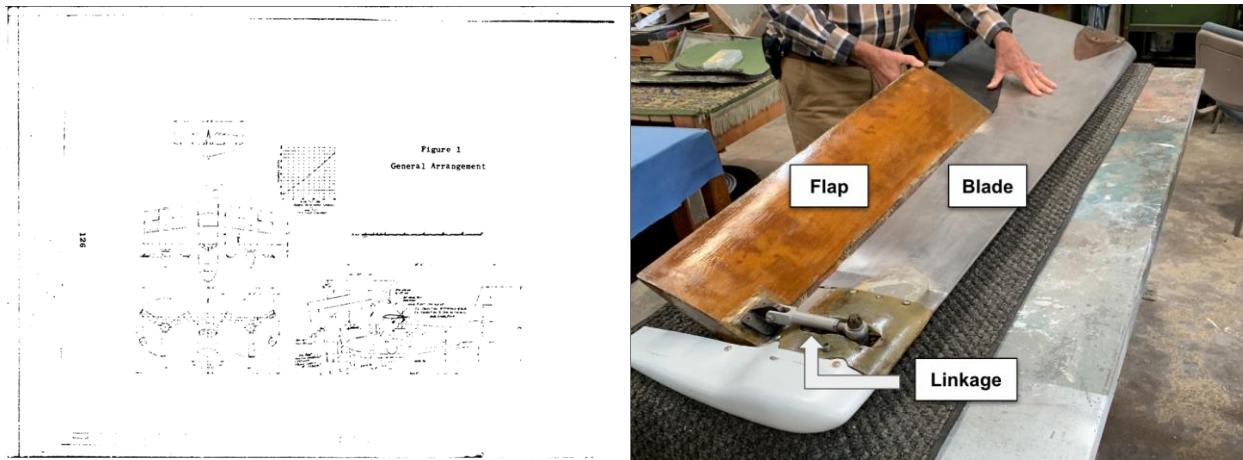


Figure 3: General Arrangement of the final K-16B design from the 1967 report [10], alongside a labeled photo of the rotoprops taken by a team member.

In 1978, M. A. Bowes wrote a historical review of multiple Kaman Corporation aircraft designs for AVRADCOM, including the Kaman K16-B [6]. This document provides an interesting perspective on this 1950's project from a 1978's technological viewpoint. Bowes stated that incompatibility problems with these design elements of the K-16B likely stemmed from a lack of understanding of the inherent nature of the design of helicopters, specifically the dynamic modeling and vibratory excitations, resulting in the failure of several helicopter prototypes at the time, including the K-16B [6].

Today, the Kaman K-16B aircraft prototype resides in the restoration hanger of the New England Air Museum (NEAM) in Windsor, CT which can be seen in Figure 4 below. As the NEAM staff work to restore the aircraft to a preserved condition for historical purposes, many questions remain unanswered as to the aircraft's ability to takeoff and fly as intended as a V/STOL aircraft.



Figure 4: Photograph of K-16B in the restoration hangar at NEAM.

2.2 New England Air Museum

The New England Air Museum (NEAM) was founded in 1960 with the mission of collecting, restoring, and presenting aircraft that illustrate the progress of aviation since the birth of flight [23]. Since 1960, the museum has collected over 100 aircraft to restore and display for guests. The museum's staff often choose to restore the aircraft not only to their original state but sometimes to different periods of that aircraft's life. NEAM's work with restoration is integral to the displays and exhibits they offer since they often receive aircraft in poor condition that have gone years without maintenance. As a result, NEAM seeks to preserve the history of aircraft through its restoration efforts.

Currently, NEAM houses the sole Kaman K-16B prototype in their restoration hangar. For each aircraft the museum restores, they must determine the level to which they will repair or

reconstruct the aircraft. For the Kaman K-16B, NEAM is aiming for a less intensive restoration process to preserve the aircraft and store it outdoors, rather than a full restoration process. This preservation goal means that the aircraft exterior will be visually restored to its original condition, however, the interior and other parts of the aircraft will be secured to prevent deterioration from weather or animals.

The value of the study undertaken as part of this MQP is to gain a better understanding of what the potential of the aircraft would have been. This investigation is possible only because of our access to modern computational tools for aerodynamic and structural analysis.

2.3 Finite Element Analysis

Finite Element Analysis (FEA) is one approach used to solve PDEs over a discretized domain. Other approaches include finite volume and finite difference. Ansys Fluent uses a finite volume solver whereas Ansys Mechanical uses a finite element approach. In COMSOL, the CFD solver uses finite volume, so different tools use different approaches. The finite volume method (FVM) can be used on all types of differential equations and can be written in divergence form. This allows the integrals to be integrated over volume before applying Gauss's theorem to convert the volume integral into a surface integral with boundaries [26]. This transforms the integration technique from integrating the differential of the dependent variable in the cells to integrating surface integrals of the fluxes of dependent variables. This method is analogous to mass conservation written using Gauss's theorem, since that approach assumes all mass that would diverge out of the control volume will pass through the control volume's boundary at some point in time [26]. The FVM imposes conservation on the dependent variable by monitoring fluxes across the cell's boundary. The finite difference method (FDM), in contrast, approximates the differentials of the differential equation to produce a set of algebraic equations that reflect the changes of the dependent variable across the cell [26]. The FEA method involves a simulation of a physical process using a numerical approach known as Finite Element Method (FEM) and is a key method used when developing simulation software. Unlike the FDM, which approximates the differentials in the governing PDEs, the FEM approximates the unknown function over the domain elements

[12]. These approximate functions constitute a system of algebraic equations that are then solved by minimizing an error function for the entire system. FEA allows engineers to replace physical prototypes with virtual experiments which can optimize their designs. This is the leading mathematical technique for complex problems where solutions of many equations are required [11]. The first mention of this technique dates to the work of Schellbach in 1851 with the beginning and application of the technique associated with the mathematician Euler around the 16th century. FEA is commonly used in structural analysis to predict how a part or assembly will behave under certain loading conditions. It solves the partial differential equations to compute structural quantities such as stress and strain with varying loads and gives an approximate solution to the problem [36]. The main benefit of FEA is its ability to help engineers detect design flaws. Tools that use FEA can be used to analyze individual parts and to determine the behavior of an assembly of objects. In post processing, different color mapping is often used to show the different values on each part of the object. One such example is pressure distribution in structures [36].

2.3.1 Governing Equations for Structural Analysis

In structures, each node in the finite element mesh will have a certain number of degrees of freedom. This will depend on the specific problem. If the problem entails two-dimensional stress analysis, there will be three degrees of freedom, translation about the x and y axis and rotation about the z axis. If the problem deals with thermal analysis, there will be one degree of freedom which represents the nodal temperature. For each element in the mesh, a vector $\{u\}$ is defined to store the scalar components describing each degree of freedom of an element. For example, a 2D beam element analysis will have 6 degrees of freedom, 3 on each node, so the $\{u\}$ vector is as shown in Eq. 1 [29].

$$\{u\} = \begin{bmatrix} u_1 \\ v_1 \\ \theta_1 \\ u_2 \\ v_2 \\ \theta_2 \end{bmatrix} \quad (1)$$

In this equation, there are 6 degrees of freedom, for the first degree of freedom u_1

represents the x-axis translational of element one of the beams, v_1 represents the y-axis translation of element one of the beams, and θ_1 represents the z-axis rotation of element one of the beams. For the second degree of freedom u_2 represents the x-axis translational of element two of the beams, v_2 represents the y-axis translation of element two of the beam, and θ_2 represents the z-axis rotation of element two of the beams [29]. The subscripts identify one of two nodes. The elements also have a stiffness matrix $[k]$. Since each element has stiffness and the load on each node will determine the displacement, Eq. 2 is used to represent the relationship between the applied stress, the stiffness of the nodes, and the displacement.

$$\{f\} = [k]\{u\} \quad (2)$$

The $\{f\}$ is the force or applied load on the element, the $[k]$ is the elemental stiffness matrix of the nodes, and $\{u\}$ is the displacement of the nodes. This is the tensor form of Hooke's law since the displacement depends on the load and stiffness of the element. The element stiffness depends on the element being used. For a 2D beam analysis, the resulting stiffness matrix is as shown in Eq. 3, with E representing the Young's Modulus, A representing the cross-sectional area of the beam, L representing the length of the beam element, and I representing the second moment of Inertia of the beam cross section [29].

$$\begin{bmatrix} \frac{AE}{L} & 0 & 0 & -\frac{AE}{L} & 0 & 0 \\ 0 & \frac{12EI}{L^3} & \frac{6EI}{L^2} & 0 & -\frac{12EI}{L^3} & \frac{6EI}{L^2} \\ 0 & \frac{6EI}{L^2} & x & x & -\frac{6EI}{L^2} & \frac{2EI}{L} \\ -\frac{AE}{L} & 0 & 0 & \frac{AE}{L} & 0 & 0 \\ 0 & -\frac{12EI}{L^3} & -\frac{6EI}{L^2} & 0 & \frac{12EI}{L^3} & -\frac{6EI}{L^2} \\ 0 & \frac{6EI}{L^2} & \frac{2EI}{L} & 0 & -\frac{6EI}{L^2} & \frac{4EI}{L} \end{bmatrix} \quad (3)$$

One thing to note is that the stiffness matrix is a square matrix, so the rows and columns correspond to the number of degrees of freedom of the element. The stiffness matrix is derived from the equilibrium equations that define the behavior of the element. Below is a diagram

demonstrating the degrees of freedom for a 2D beam element.

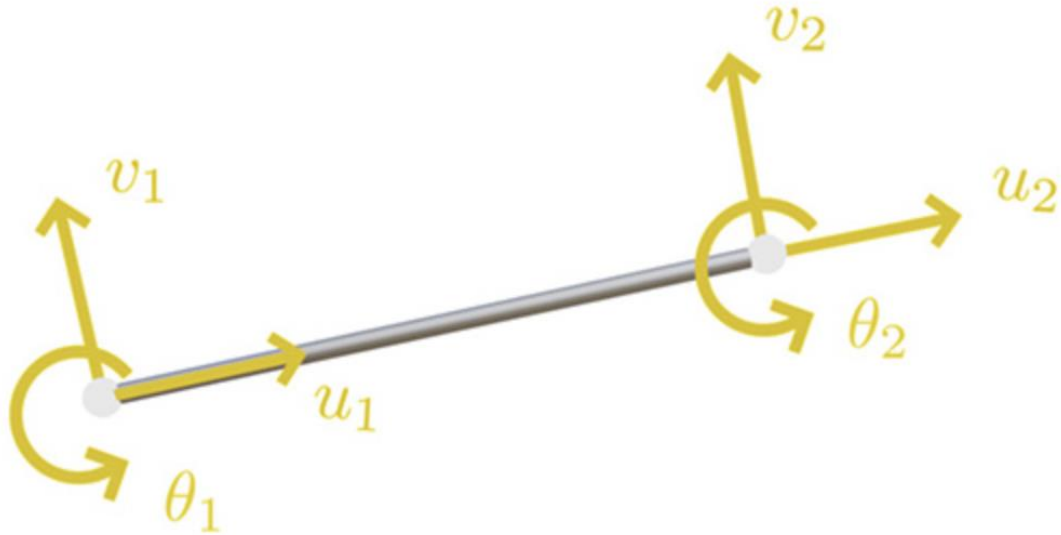


Figure 5: Degrees of Freedom for 2D beam element [29]

For the beam deflection example, Eq. 4 describes the differential equation that must be solved for beam deflection. In this equation, E represents the Modulus of Elasticity or Young's Modulus, I is the second moment of Inertia, $v(x)$ is the deflection and $q(x)$ is the load. The applied load is calculation with respect to beam deflection shown below.

$$\frac{EId^4v(x)}{dx^4} = q(x) \quad (4)$$

In some cases, the governing equations are expressed in weak form, meaning the differential equation is represented as an integral, which makes it much easier to solve more complex differential equations. To derive and solve weak form differential equations, the Principle Minimum Potential Energy and Galerkin Method of Weighted Residuals are used [29]. To apply these methods, there needs to be a way to define displacements and variables like stress and strain within the element instead of just at the nodes. Shape functions allow us to interpolate values at the nodes to calculate values anywhere on the element. The shape functions are polynomials and are easy to use to compute values accurately [29]. Once the stiffness matrix for all the elements in a mesh has been defined, they can be combined to form a global stiffness matrix. The resulting matrix

represents the stiffness matrix of the entire structure. Eq. 5 is then considered for the whole structure:

$$F = [K]\{X\} \quad (5)$$

F is the vector of nodal forces, [K] is the global stiffness matrix, and {X} is the one being solved for. To do this, the initial displacement or conditions must be filled in with other boundary conditions. Inverting the stiffness matrix is one way to solve it, however due to the stiffness matrix being very large, this will be too complex and pose challenges, therefore the conjugate gradient method is used to solve for the displacement. Solving the equation will give the translations and rotations at each node (displacement) which can then be used to solve for strain, principal stresses, and pressure distribution [29]. Von Mises Stress is a value used to determine if a material will yield or fracture. This calculation allows engineers to determine the high possible load that can be applied to a material before it yields or fractures [38]. The following equation is used to determine von Mises stress:

$$\frac{1}{6}[(\tau_{11} - \tau_{22})^2 + (\tau_{22} - \tau_{33})^2 + (\tau_{33} - \tau_{11})^2 + 6(\tau_{12}^2 + \tau_{23}^2 + \tau_{13}^2)] = k^2 \quad (6)$$

In the equation above, τ represents the stress tensor and k is a constant. The equation above shows that if the stress components are greater than the threshold of the body, the body will fracture [38].

2.3.2 Ansys Static

Ansys Static is an analysis type within the Ansys Suite (Ansys, Inc.) that uses FEA to calculate stresses and strains and other desired quantities in different structural simulations. There are two types of static analysis, linear and nonlinear [19]. In the first case, the structure is assumed to behave linearly, which means there is a linear relationship between deformation and the applied load. This analysis is most common for simple geometric structures and is commonly used to analyze trusses, beams, and frames. For more complex geometries, nonlinear static analysis is more beneficial. Nonlinear static analysis is more common for structures with a larger deformation, which means there is a nonlinear relationship between the applied load and the deformation. For

these cases, the behavior of the structure changes as load increases. This analysis is better for more complex geometries and provides more accurate results than linear static analysis [19].

An important characteristic of Ansys Static is how rotational loads are modeled. Rotational motion induces centripetal forces so that the resulting stresses include centripetal stress. In a rotating system, centripetal forces contribute a significant amount to the resulting stresses a structure experiences. This is just one way that Ansys Static defines how loads are applied to generate the most accurate results.

2.4 Computational Fluid Dynamics

Computational Fluid Dynamics (CFD) refers to the solution of an appropriate set of governing equations for a fluid problem over a discretized domain. In one common implementation, CFD solves the Navier-Stokes equations applied to a single-phase, incompressible fluid flow. Other forms of the Navier-Stokes equations incorporate effects of compressibility and turbulence. In the 1930s, these equations were already being implemented to solve many fluid problems, but due to the lack of computational tools solutions were mainly limited to 2D representations. Until the late 1950s, CFD problems were solved by hand. However, once computing technology evolved, algorithms were created to implement CFD. The first CFD computer simulation model was created in 1957 at the Los Alamos National Lab [8]. The Los Alamos team spent 10 years working on those methods, which serve as a foundation for modern programs used today. By 1967, Douglas Aircraft had created a functional 3D CFD analysis method. This method was initially developed for fluid flows on airfoils but later became known as the panel method with the geometry being simplified to make computation easier [17].

The evolution of CFD is due largely to the mathematical and computational improvements by corporations. Boeing was one of the first corporations with such advancements as they incorporated full potential equations into CFD in the 1970s [8]. Euler transonic flow equations were implemented into coding languages in 1981. By the 1990s with technology and computing ability being far more advanced than before, CFD was used heavily in automotive design.

Companies such as General Motors and Ford used the technology in 1995 to make cars that had improved aerodynamic properties compared to the boxy designs seen in the 1980s. Major organizations such as NASA, Boeing, and other corporations have improved CFD analysis to make it one of the most powerful simulation software tools available for engineers today [8].

2.4.1 Ansys Fluent

Ansys Fluent is part of the Ansys Workbench software package that uses CFD to simulate the flow of fluid, the heat transfer that takes place within a fluid, and the interactions between a fluid and the structure it flows through or over [17]. Ansys Fluent uses a method called the Finite Volume Method to solve the governing equations for different classes of fluid flow; this will be further discussed in Section 2.4.2. The finite volume method consists of “dividing the domain of the simulation into a series of small, interconnected control volumes or cells” [17]. By calculating the desired values (i.e., temperature) for each of these cells, Ansys Fluent can arrive at a converged solution through iterative algorithms [17]. This process makes Ansys Fluent a very versatile tool that can solve various classes of problems such as multiphase flows or flows with heat transfer.

To solve these iterative algorithms and to arrive at a solution for a desired parameter, Ansys Fluent requires the user to define a simulation case for which to calculate values of velocity, pressure, temperature, etc. Designing a simulation for Fluent consists of defining a geometry, meshing this geometry, and defining boundary conditions for the simulation [17]. Another aspect of the simulation that must be defined before Fluent can solve for a simulation case is the set of fluid and material properties [17]. Once setup of the simulation case has been completed, Ansys Fluent can solve the system and generate the desired values, making Ansys Fluent a valuable tool for simulating fluid dynamics.

2.4.2 Finite Volume Method

As mentioned previously, Ansys Fluent uses a finite volume method to solve fluid flows. At each time step, Fluent solves a set of equations that account for conservation of momentum and

conservation of mass:

$$\frac{\partial \rho}{\partial t} + \rho(\nabla \cdot \vec{v}) = 0 \quad (7)$$

$$\rho \left[\frac{\partial \vec{v}}{\partial t} + (\vec{v} \cdot \nabla) \vec{v} \right] = -\nabla p + \nabla \cdot \left(\mu (\nabla \vec{v} + (\nabla \vec{v})^T) - \frac{2}{3} \mu (\nabla \cdot \vec{v}) \bar{I} \right) + \nabla \cdot \overline{\overline{Re_T}} \quad (8)$$

Symbol	Definition
ρ	Fluid density
\vec{v}	Velocity
\bar{I}	Identity matrix
p	Pressure
μ	Fluid viscosity
$\overline{\overline{Re_T}}$	Reynolds stress
$\sigma_k, C_\mu, C_{\epsilon 1}, C_{\epsilon 2}, f_1, f_2$	Experimentally determined constants

Table 2: Variables used in governing equations of CFD.

It is assumed that temperature is held constant, and therefore properties that depend on temperature stay constant.

The SIMPLE algorithm guesses solutions and checks them repeatedly. The algorithm starts by guessing a pressure field. Then, it repeats the following procedure:

Solve momentum equation (Eq. 7) → Solve pressure correction equation (Eq. 8) without Re_T → Correct pressure and velocity → Solve for transport of other properties. Other properties usually include pressure-dependent terms such as viscosity and temperature. Our model assumes no other properties such as viscosity.

The velocity field, v^* , is found using the momentum equation and the guessed pressure field. Since there is no other equation to link pressure and velocity, the continuity equation is used to evaluate the total mass flux in/out of each cell. Then, cells with a positive total flux across all surfaces have their pressure, p^* , decreased, and vice versa. Next, the velocity is corrected using the new pressure terms. Finally, the corrected velocity and pressure fields from the previous steps

are checked to see if they satisfy the momentum and continuity equation. If not, the process is started again, starting with the latest guesses of p and v .

The choice of turbulence model can have a significant effect on the results of a CFD simulation. There is no exact mathematical model for turbulence, as many of the effects are on a molecular scale. Therefore, approximations are made based on empirical observations. There are many different turbulent models available in Fluent. Though each model generally has pros and cons, it seems to be the common consensus that the only way to verify the best turbulence model for any situation is by experimentation.

The k- ε model solves the following equations to approximate turbulence:

$$\frac{\partial(\rho k)}{\partial t} + \frac{\partial(\rho u_j k)}{\partial x_j} = P - \rho\varepsilon + \frac{\partial}{\partial x_j} \left[\left(\mu + \frac{\mu_t}{\sigma_k} \right) \frac{\partial k}{\partial x_j} \right] + P_k \quad (9)$$

$$\frac{\partial(\rho\varepsilon)}{\partial t} + \frac{\partial(\rho u_j \varepsilon)}{\partial x_j} = C_{\varepsilon 1} f_1 \frac{\varepsilon}{k} P - C_{\varepsilon 2} f_2 \frac{\rho\varepsilon^2}{k} + \frac{\partial}{\partial x_j} \left[\left(\mu + \frac{\mu_t}{\sigma_\varepsilon} \right) \frac{\partial \varepsilon}{\partial x_j} \right] + \rho L_\varepsilon \quad (10)$$

where

$$P = \tau_{ij} \frac{\partial u_i}{\partial x_j} \quad (11)$$

$$\tau_{ij} = \mu_t \left(2S_{ij} - \frac{2}{3} \frac{\partial u_k}{\partial x_k} \delta_{ij} \right) - \frac{2}{3} \rho k \delta_{ij} \quad (12)$$

K describes the turbulent kinetic energy, and ε describes the decay rate of k . Turbulence is modeled as random variations in the velocity of the fluid at every time step, with the magnitude of this determined by k .

$\sigma_k, C_\mu, C_{\varepsilon 1}, C_{\varepsilon 2}, f_1, f_2$ are experimentally determined constants that are built into Fluent. These can be changed in the settings, but it is highly recommended to keep these at the default values. The Wilcox k- Ω changes Eq. 10 to the following [41]:

$$\frac{\partial(\rho\omega)}{\partial t} + \frac{\partial(\rho u_j \omega)}{\partial x_j} = \gamma \frac{\omega}{k} P - \beta \rho \omega^2 + \frac{\partial}{\partial x_j} \left[\left(\mu + \sigma_\omega \frac{\rho k}{\omega} \right) \frac{\partial \omega}{\partial x_j} \right] + \frac{\rho \sigma_d k}{\omega} \frac{\partial k}{\partial x_j} \frac{\partial \omega}{\partial x_j} \quad (13)$$

Where Ω is now the turbulent kinetic energy dissipation rate instead of ε . Finally, Reynolds stress is computed with this equation:

$$Re_T = \frac{\rho k}{\mu \omega} \quad (14)$$

The team originally used the k- ε model. This is a very popular, generic model that works for most applications. With this model, turbulence is best modeled away from any boundary layers. k- ε models k , turbulent kinetic energy and ε , turbulent dissipation rate.

The second and final model the team used for the final simulation is the k- Ω model. The k- Ω model is much better in dealing with turbulence near boundaries.

2.5 Computer-Aided Design (CAD)

CAD allows engineers to create highly detailed 3D representations of complex machinery and engineered parts. Once designed, these models can be easily integrated into software such as any of the various Ansys tools, facilitating comprehensive simulation and analysis. Two primary methods were investigated to create a CAD model from an existing physical object for this project: 3D scanning and manual measurement from blueprint references. 3D scanning employs technology to reflect light and capture the geometry of the scanned object, which is then transformed into a high-fidelity CAD model accurately replicating the physical geometry. This process has the advantage of significantly reducing the time needed to create the initial model. Alternatively, engineers can opt to use manual measurements, which involve meticulously recording critical dimensions, either through physical measurements or by referencing blueprints and technical drawings to design the model within the CAD application itself. Although this process demands great attention to detail and precision, it offers greater control of the design process.

CAD has revolutionized the way that engineers create and advance designs. CAD models allow engineers to be more productive by cutting the need to meticulously create sketches and designs by hand [1]. CAD allows engineers to seamlessly implement design elements and tools and save them digitally, ensuring the design is protected. CAD can also significantly reduce the likelihood of errors since manual input is only required for model creation [1]. CAD reduces mistakes by minimizing the chances of introducing human error, allowing for direct design transfer

and quick prototyping, and making it easy to add alterations to a design [1]. Lastly, CAD models can be stored in files that are easy to share and review with partners, fostering better communication among engineers and field professionals [1]. In general, CAD models enable engineers and designers to foresee errors and test potential simulations through experimental model creation, produce high-quality models increase efficiency and productivity, and generally both expedite the design process and widen it by increasing the number of potential designs [1]. However, the process for creating these models is not limited to creating parts with features (e.g. extrusions, cuts, chamfers, etc.) in a design program. Engineers and designers can avoid the time-consuming process of creating models of an existing part from scratch by utilizing 3D scanning technology.

2.6 3D Scanning

3D scanning is a well-established technology that can be utilized for a multitude of applications, including 3D modeling, reverse engineering, planning prototypes, and marketing or educational practices [31]. Laser scanning technology implements a 3D scanner that captures an object's shape and uses this data to create a "point cloud" of those geometric samples [33]. A point cloud is a set of data points each with their own three-dimensional position, that when combined can be used to represent an object or shape [35]. There are two main types of 3D scanners on the market: time-of-flight and triangulation. Time-of-flight scanners are often used for larger objects and can scan from a considerable distance, as these scanners act similarly to devices that employ Light Detection and Ranging (LiDAR). LiDAR systems determine precise surface coordinates of an object by emitting laser light and measuring the time it takes for the light to reach the object's surface and return to the sensor [31]. Time-of-flight scanners also emit light toward the object and measure the time it takes for the light to reflect to the sensors. With the speed of light being constant, the scanner is then able to determine the distance between the scanner and the object. This measurement process is then rapidly repeated as the laser light is moved over the object until the scanner has mapped out the geometry of the scanned object. Triangulation is more commonly used for close-up (i.e. scanner-object distance less than about 400 millimeters) scans and as a result it is much more accurate than time-of-flight scanning. Triangulation scanners utilize a laser source that emits light toward the object, as shown below in Figure 6. The emitted laser is then reflected

off the object and captured by an imaging sensor. This sensor enables the laser scanner to measure both the distance and angle between the scanner and the object.

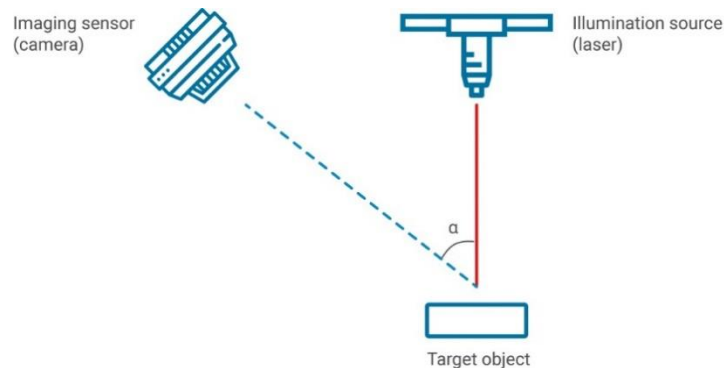


Figure 6: Basic diagram of how triangulation scanning works [25] © 2024 Hermary.

The scanner that was evaluated for this project, a Revopoint Pop 2 [28], utilizes a form of triangulation scanning called structured light. Specific details of Revopoint Pop 2 will be further discussed in Section 2.6.1. Structured light works by emitting light from a projector in a known pattern on an object while an offset camera captures the reflected light, as seen in Figure 7[25]. The geometry of the object can be found using triangulation by decoding the deformed pattern of the light reflected from the object. The distance between the light source and the camera forms the baseline of the triangulation. Between this known data and the information from decoding the pattern, the scanner can precisely determine the object's geometry. There are some limitations to using structured light. One challenge with structured light scanning is that highly reflective surfaces tend to bounce structured light off the surface in an unpredictable manner, which then makes it difficult for the scanner to detect the distorted light pattern. Structured light scanners also work best when utilized at short distances as the projected patterns can only be accurate up to a certain range; short-range is considered less than about 400 millimeters for 3D scanning. Given the restrictions with structured light, these types of scanners should be used indoors, under uniform lighting (i.e. diffused lighting), and on stationary objects.

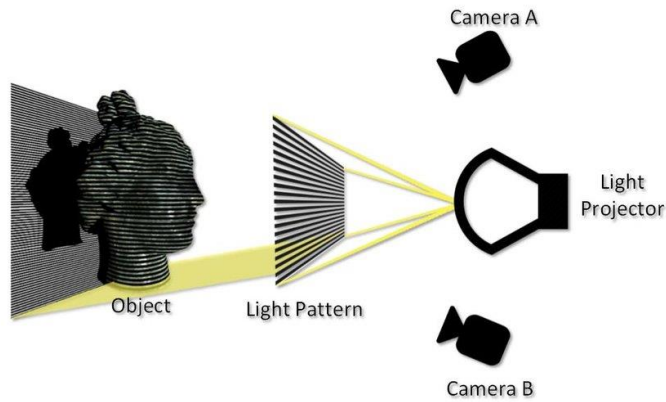


Figure 7: Diagram of structured light scanning [28] © 2017 ARC Metrologia.

A primary use of the 3D scanner can be to create computer-generated “solid” models. 3D scanners accomplish this by combining the millions of data points that represent a surface in three dimensions into a “point cloud” [31], as shown in Figure 8. Each data point is a result of a triangulation calculation with a known coordinate in some reference system. With such a large number of data points, the point clouds can resolve features with incredible precision; the Revopoint Pop 2 can detect objects with a precision of 0.05 mm [28]. Once a point cloud has been created, it can then be converted into a solid model.

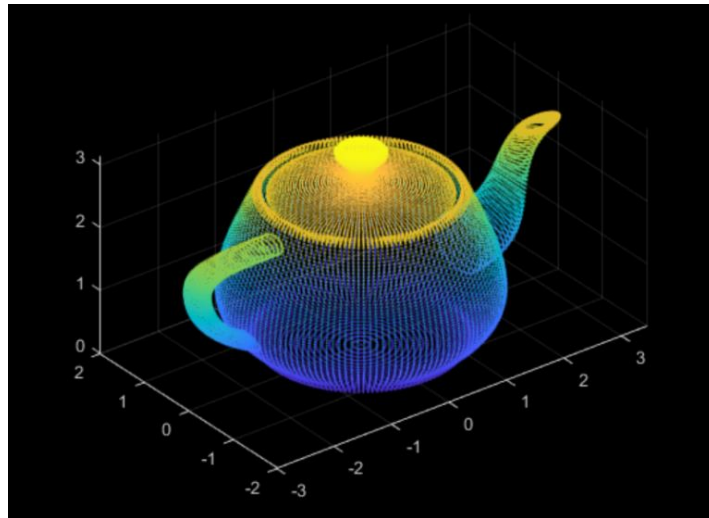


Figure 8: Example of a point cloud produced from a Revopoint 3D Scanner [28] © 2023 Revopoint 3D.

3D scanners have some limitations with respect to the surface of the material of the object

being scanned. Due to the fact 3D scanners rely on reflected light to determine the geometry of the object, the surface properties of the object are of critical importance. The ideal material surface for scanning is a matte, diffusely-reflecting, uniform surface. Any departure from this material and the scanner begins to have a more challenging time scanning. The least ideal materials are shiny, transparent, and dark materials. These material challenges can be avoided by utilizing 3D scanning sprays. These sprays, such as AESUB spray [28], are aerosol sprays that can be applied to a material to increase its optical properties to improve scanning. The AESUB sprays also completely sublime within a few hours to a day; therefore, they are ideal for increasing scan accuracy while leaving the material unchanged, unlike a paint.

The Revopoint Pop 2 implements binocular and structured light (i.e. a known light pattern), rather than infrared light or a direct laser, to capture the features of the scanned object [14]. This scanner acquires 3D point cloud data efficiently, making it a good choice for 3D scanning. A proprietary micro-projecting chip allows the scanner to have extremely high precision as well, with the highest single-frame spatial resolution reaching up to 0.05mm. This scanner implements the triangulation method, allowing the scanner to capture the object in close detail. This scanner is also embedded with a 6-degree-of-freedom (DOF) gyroscope to make spatial positioning faster and more accurate, reduce stitching errors, increase the scanner's smoothness, and enhance overall operation [25].

The process of accurately capturing all an object's features with the scanner and translating these features in detail into a CAD model is often difficult. We examined the work of the MQP team that analyzed the Burnelli CBY-3 Loadmaster and DC-3 [7], as the Loadmaster MQP team initially attempted to implement 3D scanning to create CAD models of the aircraft with which they were working. However, three major issues, described below, arose when attempting to create CAD models using this technology, leading them to create CAD models from blueprints and drawings of the aircraft.

The first issue the Loadmaster MQP team encountered was the stability of the scanner and the effect of jitter, or vibration, on scans. If the scanner was being used by hand, any sudden movements would cause it to lose focus of its target and result in errors in the scan. The Loadmaster

MQP team reported that using a rotating turntable to place the object on was a solution to this problem. However, this issue remains when a target too large for a turntable needs to be scanned, as the only option to scan such targets is the hand-held method.

Another problem that the Loadmaster MQP team documented in their final report is the impact that different colors had on the quality of a scan. The geometry of darker-colored surfaces was difficult for the scanner to capture, a conclusion this team arrived at after attempting to scan the CBY-3 Loadmaster wind tunnel model. The Loadmaster MQP team did not find a solution to this issue and instead chose to abandon their attempts to scan the wind tunnel model.

A third issue the Loadmaster MQP team had with the 3D scanning process was that the team needed to scan a bracket whose structure partially resided inside the aircraft wing. Therefore, a full scan of the bracket was impossible, and the team had to simply capture a partial scan. An attempt to complete the partial model in the CAD software was unsuccessful due to the bracket's complex structure. The team was unable to create a full model of the bracket due to this issue.

3 Methodology for Takeoff Analysis

The team created a framework to perform a takeoff analysis. The goal was to assess the takeoff ability of the K-16B and decide whether the aircraft could have taken off based on the result.

3.1 Equations to Calculate Takeoff Distance for K-16B

The first step of the takeoff analysis for the K-16B was to document and organize the necessary equations to calculate the horizontal takeoff distance, or the distance required for the K-16B to travel on the ground before it can take off. Aircraft Design by Daniel P. Raymer [27] was the teams' primary source for this sequence of takeoff analysis equations described below. Table 3 lists the variables that are used in the takeoff analysis as defined in Aircraft Design [27]:

Variable Symbol	Definition	Units
T	Thrust	N
D	Drag	N
W	Weight (Force)	N
L	Lift	N
a	Acceleration	$\frac{m}{s^2}$
g	Gravitational acceleration	$\frac{m}{s^2}$
$\mu = 0.05$	Rolling friction coefficient	Unitless
T_V	Vertical thrust	N
T_H	Horizontal thrust	N
ρ	Air density	$\frac{kg}{m^3}$
S	Wing area	m^2
C_{D0}	Parasitic drag coefficient	Unitless
k	Drag due to lift	N

C_L	Lift coefficient	Unitless
V	Aircraft speed	$\frac{m}{s}$
k_{eff}	Effective drag due to lift due to ground effect	N
V_i	Initial aircraft speed	$\frac{m}{s}$
V_f	Final aircraft speed	$\frac{m}{s}$
S_G	Ground roll/takeoff distance	m
K_T	Ground roll term containing thrust terms	Unitless
K_A	Ground roll term containing aerodynamic terms	$\frac{kg}{Nm}$
h	Wing height above ground	m

Table 3: List of identified variables used in takeoff analysis.

Raymer lays out a takeoff analysis beginning with an equation based simply on Newton's 2nd Law in Eq. (9) :

$$F = ma \quad (9)$$

This law can be written to define the point-mass acceleration in terms of aerodynamic forces and the rolling friction coefficient μ to simulate the takeoff condition, as shown in Eq. (10):

$$a = \frac{g}{w} [T - D - \mu(W - L)] \quad (10)$$

The above equation can be adjusted to express lift and drag in terms of aerodynamic coefficients as shown in Eq. (11):

$$a = g \left[\left(\frac{T}{W} - \mu \right) + \frac{\rho}{2W} (-C_{D0} - KC_L^2 + \mu C_L) V^2 \right] \quad (11)$$

To obtain the ground-roll distance, which the team has defined as the takeoff distance, required integration of the velocity divided by acceleration as shown in Eq. (12):

$$S_G = \int_{V_i}^{V_f} \frac{V}{a} dV = \frac{1}{2} \int_{V_i}^{V_f} \frac{1}{a} d(V^2) \quad (12)$$

To simplify analysis, Raymer defines the following two constants that separate terms into the thrust terms and aerodynamic terms defined in Eq. (13) and Eq. (14).

$$K_T = \frac{T}{W} - \mu \quad (13)$$

$$K_A = \frac{\rho}{2 \left(\frac{W}{S} \right)} (\mu C_L - C_{D0} - KC_L^2) \quad (14)$$

Substituting these values back into the derivative for S_G results in Eq. (15):

$$S_G = \frac{1}{2g} \int_{V_i}^{V_f} \frac{d(V^2)}{K_T + K_A V^2} = \left(\frac{1}{2gK_A} \right) \ln \left(\frac{K_T + K_A V_f^2}{K_T + K_A V_i^2} \right) \quad (15)$$

Raymer's derivation [27] results in Eq. (15) which defines the ground, or takeoff in this case, distance as an integral from an initial velocity to a final velocity. For our analysis, the initial velocity is zero and the final velocity is the takeoff velocity.

The next step was to consider the special characteristics and circumstances for the K-16B to take off. There were three different characteristics that the team determined were necessary to incorporate into the takeoff analysis, as shown in Table 4:

Characteristic 1: Ground effect, which is the substantial reduction in drag due to lift due to the proximity of the aircraft wing to the ground [27]

Characteristic 2: The multiple components of thrust due to the V/STOL nature of the K16-B, which

splits thrust into a horizontal thrust and vertical thrust components

Characteristic 3: The large deflection and downward turning angle of thrust provided by the flaps to achieve the designed hover configuration

Table 4: K16-B special characteristics to incorporate into takeoff analysis equations.

With these special characteristics identified, the standard takeoff equations needed to be modified to reflect the three characteristics given above to make the takeoff simulation representative of the unique features of the K16-B. To adjust for the diverted thrust due to the tilted-wing design of the K-16B, the team planned to separate the thrust force into horizontal and vertical components and apply each component accordingly. Note that these components of thrust are different between the thrust resulting from the deflected flow over the large wing flap; this component of thrust is incorporated into the lift coefficient. To account for the large deflection caused by the flaps, the lift coefficient C_L needed correction. We had planned to incorporate Figure 16.6 in Section 16.3 of *Aircraft Design* [27], which showed a plot of how the lift is affected by plain flaps at a small deflection for flaps that have a flap chord of up to 50% of the wing chord. Flaps increase lift generated by the wings both by increasing the wing planform area, and by increasing the camber of the airfoil. To incorporate ground effect, the team planned to calculate an effective K , or an effective drag due to lift, based on the standard drag due to lift using Eq. (16) [27].

$$K_{effective} = K \cdot \frac{33 \left(\frac{h}{b}\right)^{1.5}}{1 + 33 \left(\frac{h}{b}\right)^{1.5}} \quad (16)$$

Note that at this step, the team realized that there would be a significant impact on lift due to ground effect, not just drag. Attempting to define this change in lift due to ground effect revealed that our current method to determine takeoff ability was not applicable to the specific design of the K-16B, which will be discussed further in the takeoff methodology.

Upon review of the documents and collected information, the team realized it was missing parameters and data necessary for our analysis such as various lift and drag coefficients, thrust coefficients, wing, and flap area, and other data. To find this necessary data, the team turned to a historical review. Using the derivations of Newton's second law shown to define ground distance,

intended flight and test conditions, and the calculated and test results graphs, the team planned to fill the gaps to perform our analysis. This attempted process is further discussed in the next section.

3.2 Implementing Data from Historical Documents

A significant part of determining the K-16B's takeoff ability was to fill in any gaps in the knowledge of specific terms and parameters used in the takeoff equations. These gaps could include certain constants such as lift and drag coefficients, thrust coefficients, etc. given the unique design of the K-16B with its tilting wing and large flaps. The team needed to either identify suitable values for these parameters from research or to calculate them to complete the takeoff analysis.

Using various tables and graphs of given and calculated values provided in the G-113-4 report [2] and the equations provided in the report documenting the performance analysis undertaken during the aircraft development, the team attempted to back calculate and thereby estimate some of the original design parameters. The team also used the 1967 G-113-36 report [10] in a similar matter to interpret from their graphs of collected test data at their tested and intended flight conditions to determine representative performance values for the K16-B. It is also important to note that this report does include equations that were used to design the K-16B, but they might not be accurate given today's knowledge of aircraft design and may be missing information or rely on assumptions that are no longer true. Some of the equations of interest were the ones used to calculate thrust coefficient, pitching-moment coefficients, lift coefficients, and more. These equations can be used in some cases to back calculate original results to get original parameters.

One part of this process consisted of obtaining documents from NEAM. The team visited the museum after requesting several different documents and blueprints so that the team could review these documents and photograph them for later use. In the 1967 K-16B report [10], the team was able to obtain several final geometric properties of the aircraft that assisted the takeoff analysis. Other needed information that was not present in the 1967 report was found in the 1959 G-113-4 report [2], which by their absence may or may not have remained the same in the final

version but should be noted as dimensions that were possibly out of date by the end of the Program. Table 5 lists the values obtained from these reports [10] [2] (note that not all of these were used in the takeoff analysis but were valuable to document). The third column indicates which report the parameter was taken from:

Parameter	Value	Report
General:		
Normal gross weight, lbs.	9,300	[10]
Wing:		
Area, ft ²	231	[10]
Span, ft	34	[10]
M.A.C., in	82.3	[10]
Aspect ratio	5.18	[2]
Taper ratio	0.738	[2]
Root chord, in	96	[10]
Tip chord, in	67	[10]
Dihedral, deg.	0	[2]
Incidence angle, deg.	0	[10]
Airfoil section, root	NACA 23012	[2]
Airfoil section, tip	NACA 23012	[2]
Wing Flaps (Fowler)		
Area, ft ²	71	[10]
Chord, % M.A.C.	40%	[2]
Span, % b _w	61%	[2]
Flap extended wing MAC, in	112.2	[10]
Max. deflection, deg.	50	[10]
Hull		
Length Beam Ratio	5.4	[2]
Horizontal Tail		

Area ft ²	76	[10]
Span ft	17.25	[2]
Incidence, deg.	-1.0	[2]
Elevator area (behind hinge line)	31.7	[2]
Balance area ft ²	5.2	[2]
Trim tab area ft ²	1.67	[2]
Max. Elevator def. Deg.	±25	[10]
Vertical Tail		
Area ft ²	58	[10]
Span, from top of hull, ft.	7.95	[2]
Rudder area, ft ² (behind hinge line)	21.08	[2]
Balance area, ft ²	3.4	[2]
Horn balance area, ft ²	2.08	[2]
Max. Rudder deflections, deg.	±15	[10]
Rotor		
Disc. Area ft ²	181	[10]
Dia. Ft	15.17	[10]
Blade chord in (AV)	18	[10]
Flapping hinge offset in.	8.5	[2]
Solidity	0.18	[10]
Number of blades	3	[10]
Blade flap chord, in	9.85	[10]
Blade flap span, in	38.19	[10]
Blade section (modified in flap area)	NACA 16-50g	[10]
Blade pitch, deg.	15 to 45	[10]
Blade flap max. collective	13	[10]

deflection, deg.		
Blade flap cyclic deflection, deg.	±25	[10]
Max. RPM	725	[10]
Spoilers		
Span % b _w	55.7	[2]
Area ft ²	5	[10]
Max. deflection, deg.	50	[10]
Chord % M.A.C.	10.4	[2]
Max. Projection, % M.A.C.	0.09	[2]
Energizer chord % M.A.C.	23.4	[2]

Table 5. Values obtained from the 1959 and 1967 Kaman K-16B Reports [2] [10].

The data in Table 5 from these two references was helpful in filling in gaps in not just the takeoff analysis but also other aspects of the project such as CAD model creation. While not every value presented in Table 5 was used in the takeoff analysis, this table of values is presented for completeness, to reflect some of the useful and important data collected from the reports.

Figure 9 is a plot of results taken directly from the 1967 report and contains some of the calculated STOL performance of the K-16B presented in their results of the project [10]. The quality of the plot available to the team was poor as can be seen in Figure 9. The plot shows wing tilt angle in degrees on the Y axis and distance in feet on the X axis. The different curves represent different cases corresponding to a single wing flap angle, one line for distance to leave ground and one for distance to clear an altitude of 50 feet. The dashed line indicates a wing flap angle of 40 degrees, the solid line indicates a wing flap angle of 20 degrees. The single points are varied angles (tilting the wing up as the aircraft is taking off). The circles on some of the lines indicate where the wing tilt angle is at the ideal 19 degrees.

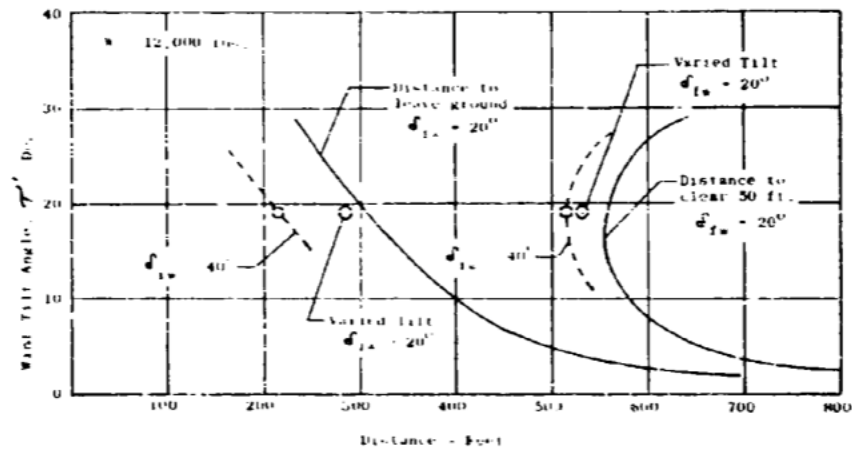


Figure 9: K-16B STOL Take-Off

Figure 9: 1967 report STOL characteristics plot for gross liftoff weight of 12,000 lbs. [10].

Table 6 shows the interpretation of the ideal takeoff conditions taken from Figure 9. It is important to note that their test results showed that a 19-degree wing tilt angle showed shorter distances for ground roll than other wing tilt angles, and a better lift-to-drag ratio is present at about a wing flap angle of 20 degrees [10]. The 40-degree wing flap deflection creates more lift, but also more drag. “With the 40-degree flap deflection, however, the greater lift resulted in so much shorter ground run (95 feet shorter) that the 50-foot altitude was cleared in 42 feet less” [10].

K-16B STOL Performances			
Parameter	Symbol	Value	Report
Takeoff with best lift-to-drag ratio:			
Weight, lbs.		12,000	[10]
Wing tilt angle, deg.		19	[10]
Wing flap angle, deg.		20	[10]

RPM		725	[10]
Approximate distance, ft		305	[10]
Takeoff with shortest distance at 19-degree wing tilt:			
Weight, lbs.		12,000	[10]
Wing tilt angle, deg.		19	[10]
Wing flap angle, deg.		40	[10]
RPM		725	[10]
Approximate distance, ft		210	[10]
Shortest possible takeoff tested with 40-degree wing flap angle:			
Weight, lbs.		12,000	[10]
Approximate wing tilt angle, deg.		25	[10]
Wing flap angle, deg.		40	[10]
RPM		725	[10]
Approximate distance, ft		165	[10]

Table 6: STOL performances obtained from the results portion of 1967 K-16B report [10].

3.3 Change in Method to Analyze Takeoff Capabilities

The team realized that many forces were not incorporated into the equation for takeoff distance derived from Newton's Second Law that would impact the ability of the K-16B to takeoff. One force we identified that would impact the K-16B's takeoff and would therefore need to be

quantified was the ground effect due to the tilted wing. Additionally, we concluded that since the wing is entirely in air downwash of the propeller. Once this was recognized, the team began to work on how to quantify the entirety of the conditions that the wing and rotoprops of the K-16B would undergo during takeoff.

One significant issue with quantifying these values was the ground effect. Raymer's text [27] provided an adjusted drag due to lift that incorporated ground effect, $K_{effective}$; however, this value does not incorporate the impact that ground effect has on the lift since the wing would be tilted when the K-16B takes off. As the team attempted to quantify this value, the team realized that the tilted wing would result in a lift contribution that could not be realistically quantified; in addition to this, the wing tilt induced horizontal contributions in both the direction toward which the K-16B is taking off and the opposite direction (i.e., in the positive and negative horizontal directions). Attempts to quantify these values were also unsuccessful, as we were unable to find a quantitative definition for this ground effect or to derive one ourselves.

The second issue, too significant for a valid numerical analysis approach such as the derivation from Newton's Second Law to be valid, was the propeller's position with respect to the wing. Because the propeller of the K-16B is attached to the front of the wing, the wing is entirely in downwash air from the propeller. Because of this downwash air, the takeoff analysis based on Newton's Second Law calculate takeoff distance are not valid for the engine arrangement used on the K-16B. So, even if the team was able to directly quantify all aspects of ground effect and incorporate the numerical value of ground effect into Eq. (12), Eq. (12) would not consider the downwash air which is too unpredictable to model numerically.

Because of these two issues, and after more research on the wing being in the downwash air of the propeller, the team decided to shift to CFD to gather the necessary data to determine the K-16B's takeoff ability. The team then attempted to use the CFD analysis to gather lift and drag data to assess the takeoff capabilities of the K-16B.

The team planned to use Fluent to simulate the lift and drag forces on the wing during takeoff. This was to be done by exporting from Fluent the resultant force on the aircraft at increments of freestream velocity. This plan was for these results to be exported into MATLAB,

where the rest of the takeoff calculations would be done. See Appendix A for the full MATLAB takeoff code that was completed. This was intended to solve the problems the team was having when attempting to accurately predict and quantify the behavior of the air downwash of the propeller by using CFD to incorporate these effects.

The team planned to write multiple functions once the results were exported into MATLAB. These functions are:

Function 1: This function would take the exported resultant forces and freestream velocities from Fluent and create a plot of the data.

Function 2: This function would separate each resultant force into its horizontal and vertical components using basic trigonometry.

Function 3: This function would use “fsolve” with the vertical component of the resultant force to find the point where this vertical force, or lift, is equal to the weight of the K-16B, and then to find what the velocity is at this point. This velocity would correspond to the takeoff velocity.

Function 4 (“takeoff_distance”): This function would use the ODE45 solver with the takeoff velocity as an input to calculate the K-16B’s velocity and horizontal distance as a function of time. This function would then find the first point where the velocity surpasses the takeoff velocity input into the function and then subsequently the time and horizontal distance traveled at this point. This time and horizontal distance would be the takeoff time and takeoff distance.

While the subteam of students working on the takeoff analysis waited for the Fluent subteam to obtain CFD results, the team wrote Function 4 mentioned above. The team defined Function 4 that used ODE45 with the initial velocity and horizontal position of the K-16B to calculate the K-16B’s velocity and horizontal distance at each time step.

The next function that needed to be written would be Function 3 that calculates the takeoff velocity using the MATLAB command “fsolve”. The takeoff velocity calculated from finding the velocity when lift is equal to weight will be an input to Function 4. With this input, “Function 4 identified the first point where the K-16B’s velocity surpassed the takeoff velocity input. Then,

Function 4 found the time and horizontal distance at this indexed point which would be the takeoff time and distance since this index represented the point where the K-16B is able to take off.

While waiting for results from the Fluent subteam, the takeoff subteam tested Function 4 twice, first with the placeholder values of 1 Newton for a horizontal force and 1 kilogram for the K-16B's mass. The subteam was able to verify the results provided by Function 4 by hand using placeholders of 1 where necessary and confirm that the ODE45 solver was working correctly. The team then tested this function by researching net thrust and takeoff mass values for the Eurofighter Typhoon so that the function would be using more realistic values, and once again the ODE45 solver functioned as expected.

The programming of the other necessary functions, Function 1 and Function 2, to complete the takeoff analysis were stopped once the full K-16B model failed to mesh in Fluent and the team decided for multiple reasons that the takeoff analysis would not be feasible.

3.4 Results

The new takeoff analysis approach was entirely dependent on running the model of the entire K-16B in Ansys Fluent and obtaining results for the net force on the K-16B through CFD analysis. However, the full model of the aircraft was unable to be meshed. Because of the various meshing issues and given the time constraint of the project, the team determined that the team could not confirm analytically that the K-16B could have taken off and that the first goal of the project would not be met. Instead, the team chose to use the remaining project time to go through our originally planned analysis process in Fluent, but simply with the rotoprops alone. Since the rotoprops model was much simpler to mesh and meshed in Fluent successfully, the analysis could be carried out on the rotoprops.

However, based on this plan of action, the team would not be able to determine the takeoff abilities of the K-16B. It is reasonable to assume that if results from CFD were able to be obtained, then the analysis approach, using MATLAB, outlined in Section 3.3 would have been successful in determining a takeoff time and distance.

So, while the takeoff analysis was unsuccessful in achieving Goal 1 and answering whether the K-16B could have taken off, the team learned valuable lessons about the necessary steps in the takeoff analysis process, the potential for CFD to capture accurately a takeoff simulation, and the ability to use programming to interpret and further process Ansys results. If the team had started the CFD method of takeoff analysis sooner in the project and had more time to overcome meshing problems with the full K-16B model, the takeoff analysis might have been completed. Future MQP teams should allot as much time as possible to meshing complex models so that enough time is available to run the models and interpret the results.

4 Methodology of Digitally Reconstructing KAMAN K-16B Rotoprop

The methodology that the team used to create the rotoprop model evolved through multiple iterations as the project progressed. The team began with 3D scanner testing and experimenting with ImageJ to measure rotoprop images. ImageJ [16] is a free online platform that allows users to upload and measure images to scale based on a known distance in the photo. The team ended up using the aircraft's blueprints to create 2D digital sketches of the airfoil cross-sections, which were then lofted together in SolidWorks to create a 3D model. Using the cross-sections depicted in the blueprints, the team was able to get accurate dimensions to construct a high-fidelity, digital model of the rotoprop.

4.1 3D Scanner Experimentation

Creating an accurate CAD model of the rotoprop was key to the subsequent analysis of rotoprop thrust and induced stresses, which was the initial motivation for the team to implement 3D scanning technology. The primary issue that the team encountered when 3D scanning was reflectivity. When scanning objects with reflective surfaces, a significant amount of outlier data points is detected in the point cloud. As a result, the 3D scanner was unsuccessful in detecting and scanning the entire object accurately.

Another difficulty that the team encountered was scanning objects above a certain size by hand. To scan a large object like a rotoprop, one must hold the 3D scanner in their hand and sweep the object slowly with the scanner. The scanner uses triangulation to project a pattern onto the part's surface, and the surface geometry is captured through the distortion of the pattern [25]. This process proved to be prone to errors if the hand holding the scanner was even slightly unsteady; as a result, the 3D scanner was not able to accurately capture anything that was tested of a size comparable to the K-16B rotoprop blade.

The team conducted various tests to resolve these problems before traveling to NEAM to scan the rotoprop. The results are shown in figures below:

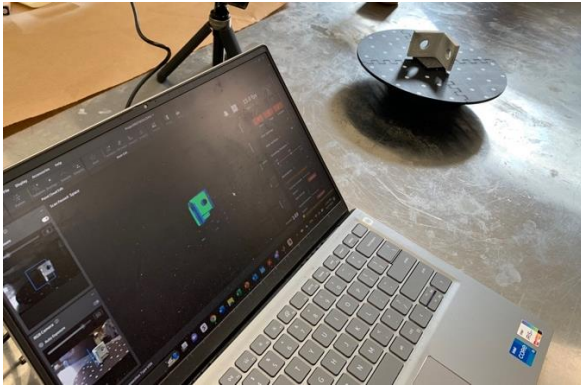


Figure 10: Bracket tested with 3D scanner on turntable and results of scan on screen.

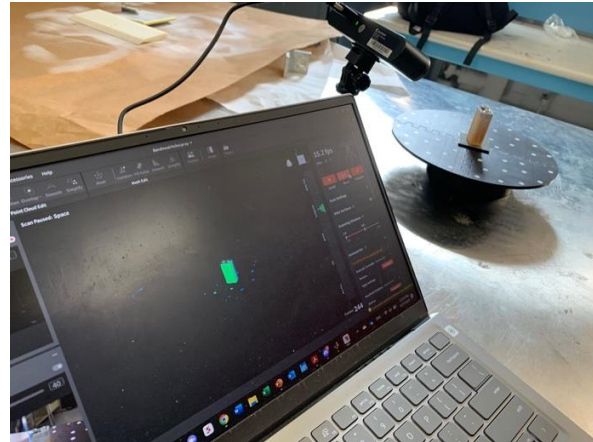


Figure 11: Battery tested on turntable with results of scan on laptop screen.

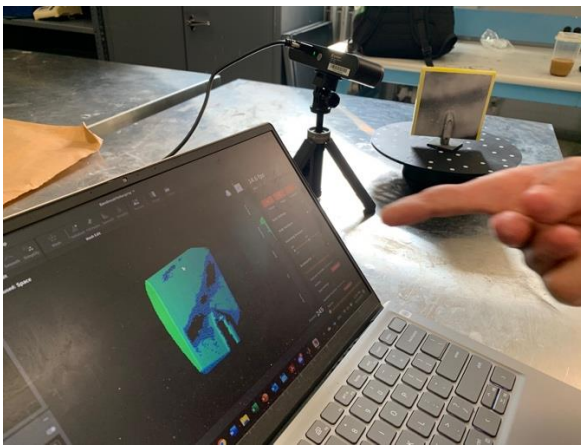


Figure 12: Airfoil tested on turntable with inconsistent scanning results due to concentration displayed.

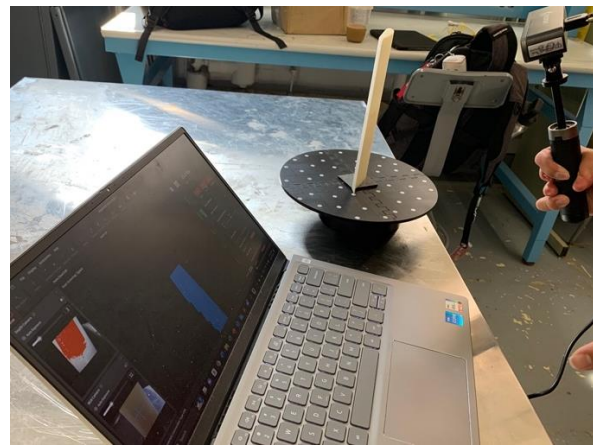


Figure 13: 3D-printed airfoil being scanned on turntable with scan results shown.

First, the team tested the Revopoint 3D scanner using a plastic bust that came with the scanner. The bust sat on a small rotating turntable which had a black surface with white dots on it that aided in the detection of both the turntable surface and the surface of the bust by the scanner. The bust was scanned without error and created an accurate 3D scan of the bust. This point cloud resulting from this scan was also imported as a CAD model into SolidWorks.

After the success encountered with testing the bust, the team decided to test various objects

without any additional methods adopted to reduce the extraneous and erroneous data points caused by highly reflective surfaces. However, since these tests were unsuccessful, the team purchased AESUB Scanning Spray, which is designed to make reflective surfaces easier to scan. Once this spray was received, the team sprayed the same objects that they had attempted to scan previously and retested them. The first object was a metal bracket, and once this bracket was sprayed the 3D scan was successful, as the entire object was detected by the scanner. See Fig. 10.

The next object that was sprayed with the AESUB spray and then scanned again with the Revopoint scanner was a battery. See Fig. 11. This battery had a dark surface that, without the spray, was undetectable by the scanner. The brighter surfaces of the battery were also difficult to detect by the scanner without the spray. Once the spray had been applied to the battery and the battery was rescanned, all the battery's surfaces other than the dark end were detected. However, based on both the angle at which the scanner and battery were oriented and potentially an insufficient amount of spray on the dark surface, this surface was not able to be picked up by the scanner. Sometimes, if the scanner was at an angle normal to the object's surface the orientation would hide any geometry changes or cavities. This problem was also sometimes encountered if the scanner was at a grazing angle to the surface, simply due to each object's unique geometry. Since the rotoprops have some dark surfaces, careful attention to the orientation of the scanner would be needed to capture all the rotoprop features with the scanner.

Another item that the team scanned with the spray was a small airfoil provided by a member of the WPI aerospace engineering Dept. faculty. When sprayed, this airfoil was easily detected by the scanner. The team made the following observations: First, one can see from Fig. 12 that the spray must be sufficiently concentrated. One area in the middle of the airfoil had a lighter layer of spray, and parts of this area were undetectable by the scanner. So, the team had to ensure that when the rotoprop is sprayed to be scanned, the AESUB is sprayed uniformly and with enough of a layer so that the surface is sufficiently and uniformly coated with the spray; this technique would likely result in the most success when scanning.

The second observation was that AESUB residue remained on the model after the 24-to-48-hour drying time specified in the product documentation. It is important to note that this was

the only object that the team tested that showed any signs of leftover spray on its surface. The AESUB scanning spray type tested is designed to sublimate completely after about four hours so that the surface of whatever was sprayed is returned to its original state. This is vital to the scanning process since the team does not want to alter the rotoprops in any way since NEAM aims to preserve them as part of the restoration process.

The team has several theories as to why there was some residual spray leftover, the primary one being that the airfoil was the first object sprayed. The team member who sprayed it did not shake the can before spraying the airfoil, but rather after spraying the airfoil. Therefore, the residue could have only been left on this object because the spray was not properly mixed according to the directions. This theory is supported by the fact that no other objects had leftover spray on their surfaces, since the can was shaken before spraying those objects. Another theory for the leftover residue was that the team member applied the spray too close to the surface. It is important to follow the spraying distance guideline listed on the AESUB can so that the spray will fade properly. A final theory is that the spray was leftover due to the material of the airfoil, or the paint used on its surface. This theory is the weakest as this spray is designed to be used on most common materials. Further investigation into the material and surface characteristics of the airfoil and the specifications of the AESUB spray is needed before this can be ruled out, however.

The last item that the team tested was a 3D-printed airfoil from one of the team member's previous classes. This item was detected better with the spray than when the team scanned it without the spray, but other items the team tested with the spray were detected more clearly than this airfoil. See Fig. 13.

One alternative to using this model 3D scanner was to buy a 3D scanner capable of scanning larger objects from a large distance. The Revopoint RANGE 2 scanner manufactured by Revopoint has a maximum range of about 1300 millimeters, capturing everything in an 860-by-1380-millimeter frame at that distance. This scanner implements dual-camera structured infrared light to scan large objects. While this scanner would have been a promising path forward in 3D scanning the blade, cost, time constraints, and the risk that it would still not properly scan made this option unattractive.

4.2 3D Scanner Results

The team looked at other alternatives for the 3D scanner technique. After conducting some research, it found that Revopoint produces 3D scanners that are designed to scan larger objects. However, due to the time constraint on the project, the team decided that trying a new scanner was not a viable option. The team instead decided to implement digital calipers to measure certain features onsite, and to photograph the actual rotoprop residing at NEAM for measurements. From the pictures and measurements, the CAD team would then be able to create the model that could be imported into other software programs. This process allowed the team to extract the necessary measurements and create the model in a timely manner.

4.3 Creating a CAD Model of the Rotoprop

Creating an exact digital replica of the rotoprop was essential to determining the performance capabilities of the K-16B. Today, engineers have more advanced analysis tools such as CFD and a better understanding of the engineering design capabilities of aircraft provided by these tools. Using the tools available today provides our team with a unique opportunity to analyze an experimental and innovative design from a time without our advanced analytical tools. Using the blueprints, historical reports, photographs, and measurements gathered from the team's research and access to the documents and aircraft itself, they were able to create a high-fidelity digital replica of the rotoprop. This allowed the team to analyze and determine the performance capabilities of the K-16B rotoprop and determine missing information accurately.

4.3.1 Implementing Data from Historical Documents

To model the flow interacting with the rotoprop, strip analysis method was used in the initial studies of the K-16B's performance. This method is a two-dimensional analysis that predicts flow effects, such as stall [10]. This method was used in the original work done in the 1950's, being described in the 1967 report G-113-36 and in more detail in the 1959 report G-113-4 [10] [2]. As described in a report from 1967, "No method has been found for relating the strength of

these vortex sheets to the tip angle-of-attack and load distribution; therefore, they are not accounted for in the two-dimensional strip analysis. Because the effect of the natural boundary layer control on the inboard sections is not considered in the present analytical method, the calculated results are conservative” [10]. Therefore, it must be noted that in the original analysis of the rotoprop that the underside of the blade, which included the linkage, was ignored in the estimated calculations but was incorporated in their testing. This highlights an important consideration that although important to the design process, their estimated performance values are estimations limited by the times modeling capabilities. Their test data is a better representation of real behaviors since the aircraft itself is tested under designed operating conditions.

The K-16B has blade pitch control, where each blade can be positioned at the same angle; with a range of motion of 15 to 45 degrees defined as the angle between the root chord and the hub (relative to its direction of rotation) [10]. The collective deflects the collective flap from its up position (the position where the flap is flush with the blade, where it is a standard rotor) of 0 to 13 degrees (deflected down towards the tilt wing) [10]. The cyclic deflects the flap from its neutral point to 25 and negative 25 degrees [10]. In Fig. 14, the dimensions of the aircraft are that of an earlier iteration from the 1959 report, which are different than the final design but are included since the final designs general arrangement is illegible [2]. For example, the vertical tail was extended higher for better stability and the rotoprops were modified, notably the diameter became larger in the final general arrangement [10].

THE KAMAN AIRCRAFT CORPORATION
BLOOMFIELD, CONNECTICUT

MODEL K-16B

DATE 20 February 1959

REPORT NO. G-113-4

Figure 1(a)

PAGE NO. 71

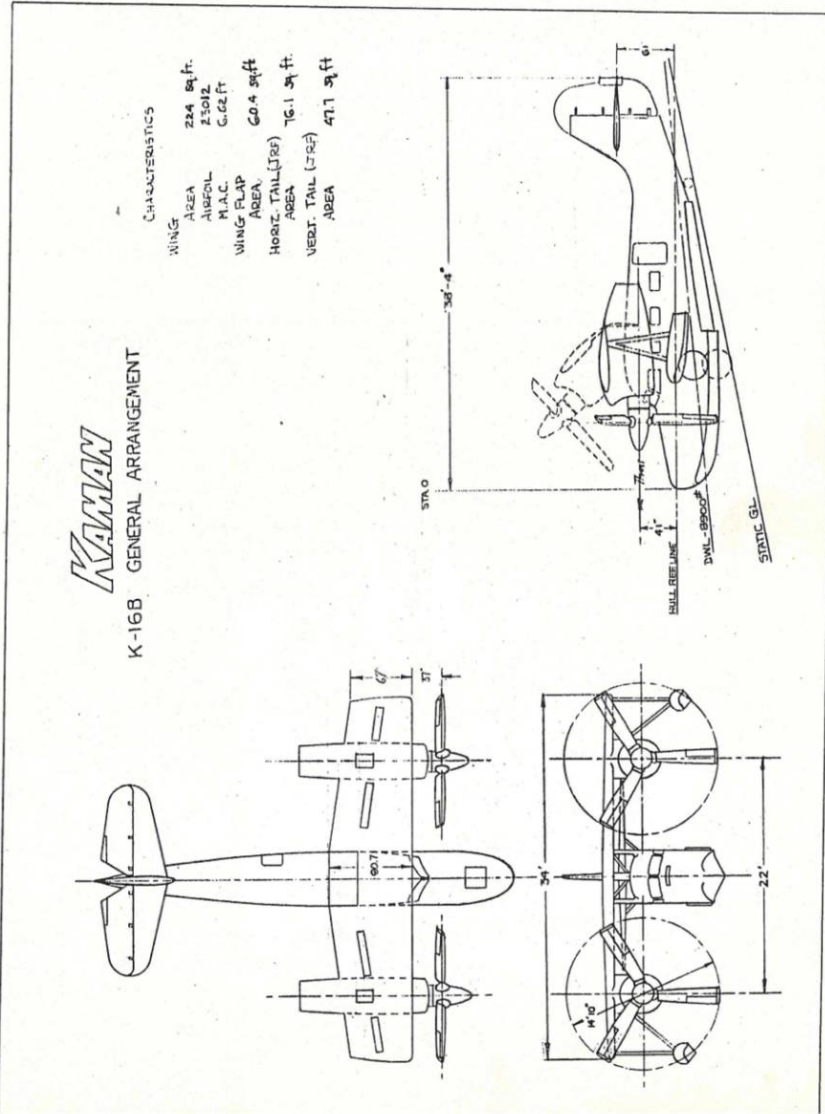


Figure 14: General arrangement of the K-16B from the 1959 estimated flying qualities report [2].

4.3.2 Photographing Blueprints

The team was provided access to some of the documents stored at NEAM in a digital

format, such as the G-113-4 report from 1959 titled, “Estimated Flying Qualities of The Kaman K-16B VTOL/STOL Aircraft” [2]. The team visited NEAM to take detailed photographs and collect vital information from the documents stored in the museum’s archives. The team had the opportunity to collect information that cannot be seen from observing the built K-16B. Some of the information found includes a detailed list of materials used in the construction of each rotoprop, a one-to-one scale blueprint of multiple cross-sectional cuts of the blade, aileron pushrod assembly, and rotoprop control assembly diagrams. The team used a Canon Rebel T3i EOS 600D camera with a Canon EFS 18-55mm zoom lens mounted on a tripod, lens pointing down to take photographs through a plexiglass sheet so the document was protected, both from students walking on it and from the tripod, which would not have to rest directly on the sheet. The team also used a circular polarizing lens filter to reduce unwanted reflections from the lighting on the glossy plexiglass surface. Having this information that cannot be seen from observing the rotoprop itself was important to the team’s analysis because it allowed them to model the internal structure to get more accurate analytical results from our Ansys Fluent and Structures simulations.

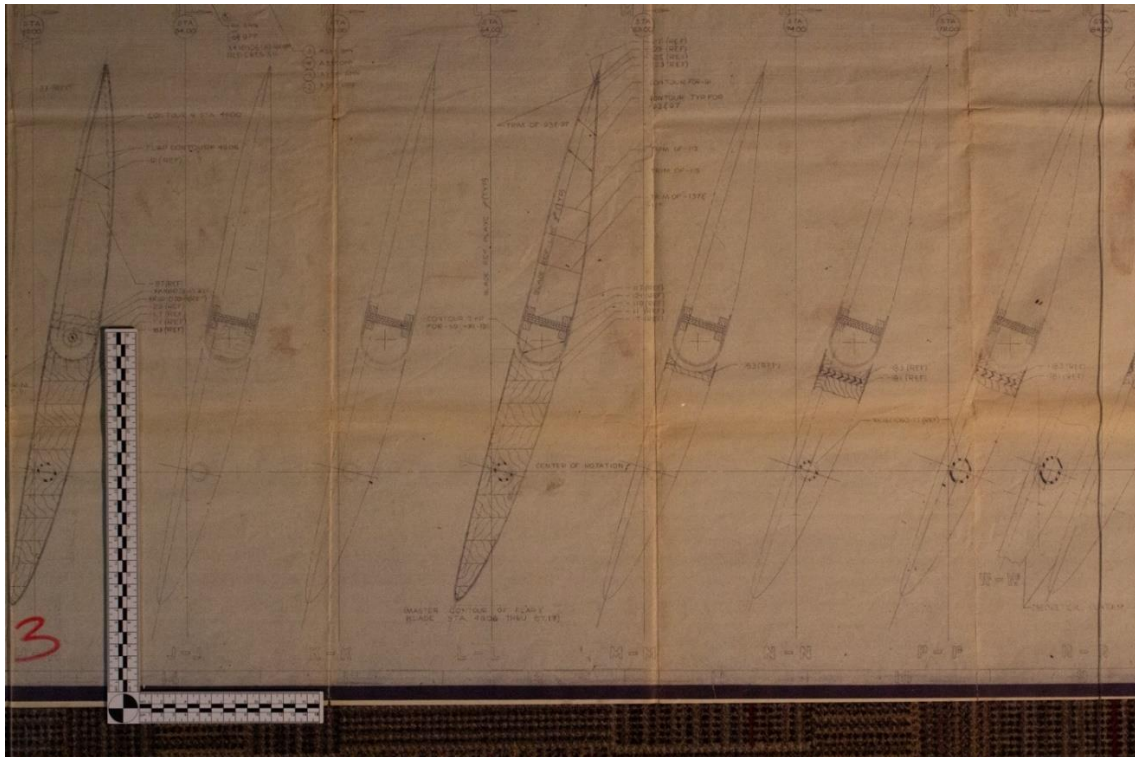


Figure 15: Photo of blueprint showing cross sections of the blade with center of rotation and material structure shown [NA2].

4.3.3 Photographing the Kaman K16-B Rotoprop

The team visited the New England Air Museum to take detailed photographs and measurements of one rotoprop blade to get the most accurate information on the final construction of the blade. We used a Canon Rebel T3i EOS 600D camera with a Canon EFS 18-55mm zoom lens for our photographs, mounted on a tripod. To limit optical distortion produced by the wide-angle zoom lens, the lens was set to about the middle of its range, approximately 36 mm. The tripod was set at a height where the lens center is at the middle of the blade to further limit optical distortion effects, which could affect the final shape and level of accuracy of the final rotoprop model. The camera was mounted on its side (portrait orientation) and put at a distance where most of the blade was visible in the frame to achieve the highest pixel resolution possible. An evidence ruler was included in each image to provide a reference scale for sizing and a green backdrop was used to create a contrast with the background to make the boundaries of the shape more visible. To ensure each position had an optimal resolution, three photographs were taken at each position, refocusing the camera each time. There were eight sets of vertical images taken, where the blade is rotated 90 degrees to 360 about its long (span) axis. Four of the sets began with the position of the blade shown in Figure 16, and rotated 90 degrees each time, resulting in positions where the camera lens is perpendicular to the bottom and top of the blade and straight at the leading and trailing edges, which can be seen in Figure 17.



Figure 16: Perpendicular view of the underside of the rotprop blade used to generate the CAD model.



Figure 17: Perpendicular view of the leading edge of the rotprop blade used to generate the CAD model.



Figure 18: 45-degree view of the rotprop blade used as a reference to generate the CAD model.

The other four were positioned at a 45-degree angle relative to the original position which can be seen in Figure 18, resulting in overall reference images to guide the shape and twist of the blade. Some of the positions photographed also showed the collective flap fully deflected in the up or down position. Three images were taken from the top of a ladder looking directly down on the rotoprop blade at three focus points to attain detail at different depths and to see the twist more easily.

Numerical data was collected using calipers and rulers to provide dimensions of the pushrod and mechanism, nose cone, blade mounting points, and various gaps present on the blade. A picture of the sample measurements is shown in Fig. 19. This was done to ensure there were multiple accurate reference data types collected to ensure the accuracy of both shape and size within the generated CAD model. The small pieces, such as the pushrod and the rod mounting bracket, were measured extensively due to their small size relative to the overall image. This also allowed for a better record of the three-dimensional shape that the part is rather than a one-dimensional viewpoint since the camera cannot see through the blade.

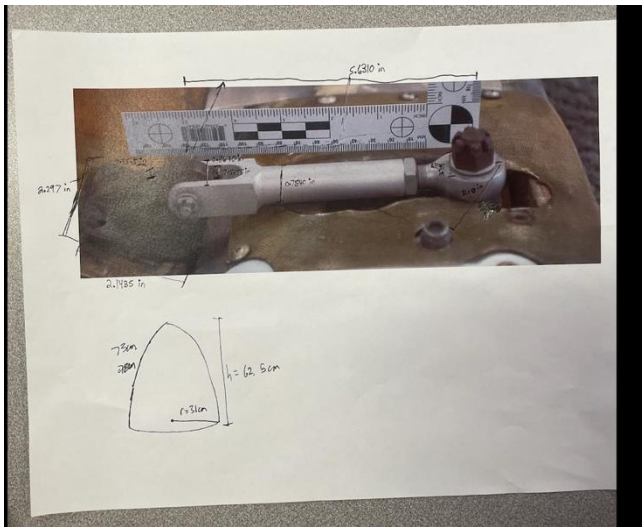


Figure 19: Sample photo of measurement of hinge on flap.



Figure 20: Picture of the nose cone.

4.3.4 Using ImageJ

ImageJ is a free software tool designed by Wayne Rasband [16] that allows the user to take precise measurements from an image with a known measurement. The user can upload an image with a known reference distance (e.g. a ruler or other object of known length) in the frame then use the software to draw a line of that known distance. The known reference length provides a calibration between pixels and physical length. This procedure creates a scale in the software that the user can use to measure other features. This allows the user to properly scale and create an accurate CAD sketch from the measurements taken from the image.

4.3.5 SolidWorks

A digital replica of the rotoprop was created using SolidWorks. SolidWorks is a CAD software tool that enables engineers to produce detailed drawings and design models in 2D or 3D that can be further analyzed in simulation software like Ansys. The team decided to use SolidWorks because SolidWorks is the preferred CAD software among engineering students at WPI due to license availability and its compatibility with Ansys. The team was able to export models in Parasolid format (.x_t) for CFD or structural analysis in Ansys.

Within the process of creating the digital model of the rotoprop in SolidWorks, there were two different workflows that the team employed. The first method was to create the model using the photographs taken of the physical rotoprop blade and parts at NEAM, and the second method was to create a model using the blueprints and other Kaman K-16B documentation available at NEAM.

The team initially experimented with creating the entire rotoprop model solely from the photographs but realized that creating the model using this method would not achieve the desired fidelity. The biggest issue to consider was the twist in the rotoprop blade, and the other curved surfaces. After a few tests, the team realized that capturing the twist and the airfoil shape accurately from the photographs would be extremely difficult, so another method was used to create those parts. However, the team was able to create the control surface linkage on the rotoprop blade using the photographs, as the linkage had a simple geometry. Using photographs of the linkage assembly

from various angles with an evidence ruler in the frame, the team used ImageJ to scale the photo accurately and draw the geometry for each part which was then assembled using a SolidWorks Assembly.

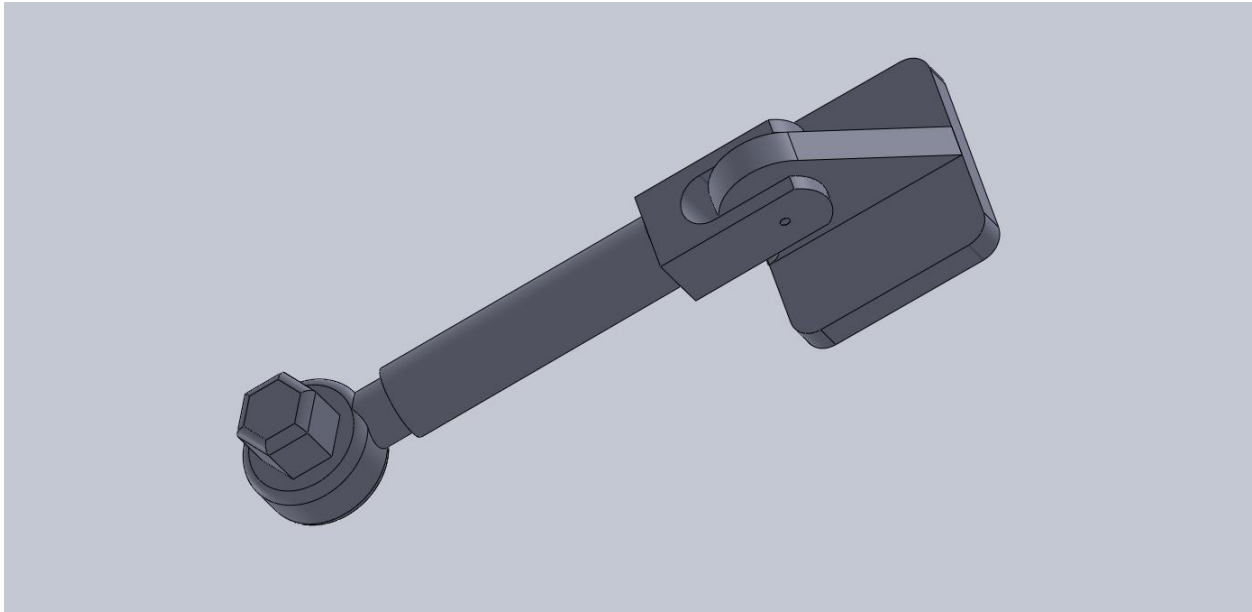


Figure 21: Image of the control surface linkage SolidWorks assembly created using photographs.

The rotoprop blade model was created using the blueprints that were available to the team at NEAM [NA1]. One blueprint of the rotoprop blade displayed a total of 16 airfoil cross-sections, each drawn to 1:1 scale. Each airfoil was sketched on a plane, with spacing between planes labeled in the blueprint. As stated previously, when taking the blueprint images, an evidence ruler was placed in the frame of every picture. The evidence ruler was used in SolidWorks to scale the picture by setting the known distance on the ruler and therefore the geometry to the corresponding distance in SolidWorks. Scaling the picture ensures that each sketch created from the blueprint is consistent and the dimensions are uniform. Fortunately, we did not need to adjust the scale by another factor because the blueprint was 1:1 with the evidence ruler. The spline sketch tool in SolidWorks was used to trace each of the airfoil cross sections to ensure the digital model is the same as the blueprint. After sketching all the airfoils on parallel planes consistent with the dimensions in the blueprint, each 2D airfoil was then lofted together to create a 3D model of the rotoprop. The CAD

subteam then drew a circle at the quarter-chord of the first airfoil and used the extrude cut feature in SolidWorks to cut the hole for the rod which is needed for the rotoprop assembly as displayed in the blueprint.

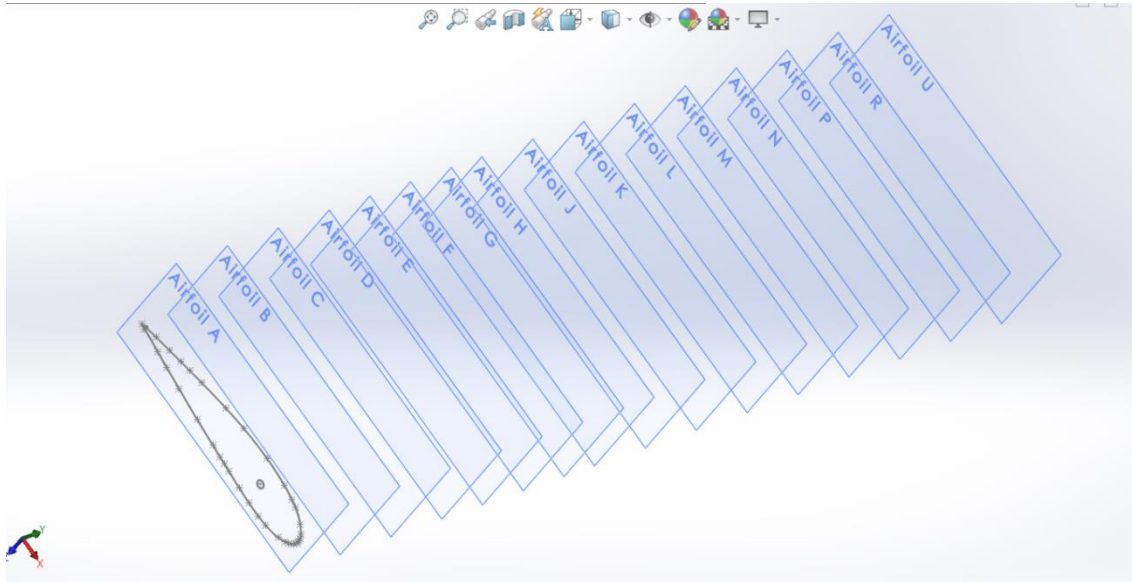


Figure 22: Image of the planes where airfoil cross-sections were sketched.

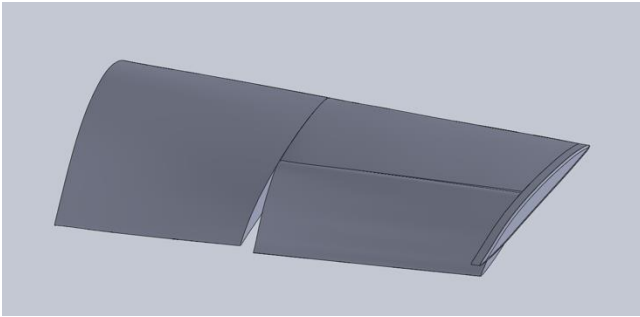


Figure 23: Image of the rotprop blade with collective flap deflection based on blueprint cross sections.

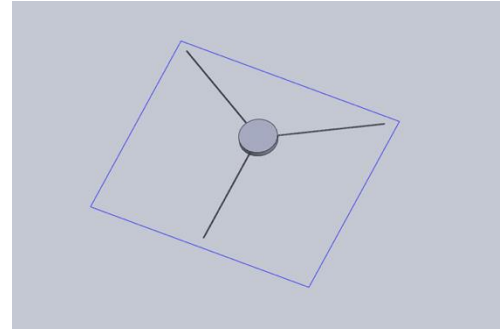


Figure 24: Image of the rotprop hub.

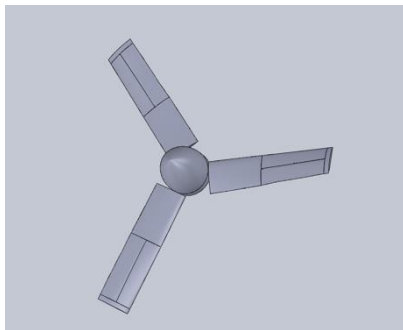


Figure 25: Image of the assembled rotprop.

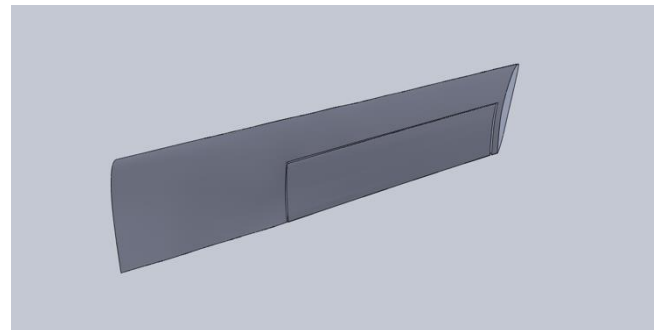


Figure 26: Image of the simplified rotprop blade.

The rotprop blade assembly also includes a control surface, the collective flap, which was also shown in the blueprint's cross sections. Once the collective flap was made, the team was able to rotate it about its rod to create variations in flap deflection that could be used for analysis.

The full rotprop of the Kaman K-16B consists of three rotprop blades, a hub, and a nose cone. After creating the rotprop blade, the team designed a hub for the rotprop, which is the central part of the assembly where all the blades are attached. The hub is an extruded circle that has three rods attached to it that represent the tie rods that extend through each of the blades. The diameter of the central circle is the same as the diameter of the rotprop hub cover measured at NEAM.

Once the hub was designed, the team created a final rotprop assembly in SolidWorks using all the individual parts. They used coincident and concentric mates to align all the parts where they were meant to be.

The CAD subteam created many iterations to the rotoprop model before they produced a model that successfully meshed in Ansys. Some changes made in the iterative process included ensuring the edges were rounded and reducing the complexities in the model as much as possible. The CAD model of the entire rotoprop assembly couldn't be meshed for analysis due to the complexity. There were many small features and errors that resulted when meshing was attempted. The subteam spent a considerable amount of time working on the problems but were unsuccessful in achieving a mesh of the full rotoprop. Given the time constraints on the project, the team had to test and simplify the model at many points along the way, a process that was slow and painstaking. For example, a feature on the blade model was the endcap with smooth curved surfaces that the CAD subteam was able to model, but there were issues with meshing it due to the connection points. So, one of the simplifications that the CAD team made was to keep the tip a flat surface. The final blade mode that was successfully meshed and used for the Fluent analysis was the simplified blade shown in Fig. 26.

5 Methodology of Computational Fluid Dynamics

The team chose to conduct CFD simulations to analyze the rotoprop thrust performance. The goal of these simulations was to determine the thrust capabilities of the K16-B rotoprop, and to understand the variables that play a role in maximizing the thrust.

5.1 Single-Rotoprop Boundary Condition Approach

The team originally investigated what we referred to as the “single-rotoprop boundary condition approach”. This is a method of simulating the propeller wherein a single, stationary propeller blade (and stationary mesh) is subjected to a flow, defined by the boundary conditions specified. The streamlines of the flow have a circular curvature and have a faster velocity near the blade tip. After the forces acting on one propeller blade are determined, this data would be extrapolated to estimate the forces on an entire three-blade assembly. The team pinpointed two major drawbacks with this method. First, it lacks the ability to model interactions resulting from the propeller blade passing through the previous blade’s wake and second, the boundary conditions are difficult to adjust to account for different conditions. The first drawback would be especially amplified by the presence of K-16B’s unique rotoprops’ collective flaps and external linkages. Due to these reasons, the CFD team opted to not use this method to attempt to create a higher fidelity simulation.

3.5 5.2 Full Rotoprop Rotating Mesh Approach

The CFD team ultimately decided to use the “Rotating Mesh Approach”, which involves modeling the entire three-rotoprop construction as it rotates in a free stream. This seems to be the most common approach when analyzing propellers in Ansys FLUENT [17]. This approach, while more computationally intensive, better captures the turbulent interactions between the rotoprop blades and is simpler to set up. The simplicity of this setup also allowed for the CFD subteam to spend less time setting up the boundary conditions for each individual scenario, and to focus on other issues such as meshing.

5.2.1 Geometry

Since we used the rotating mesh approach, the entire rotorprop construction with three blades and a nose cone was modeled. We began by importing the rotorprop parasolid file geometry into Ansys Design Modeler as seen in Figure 27.

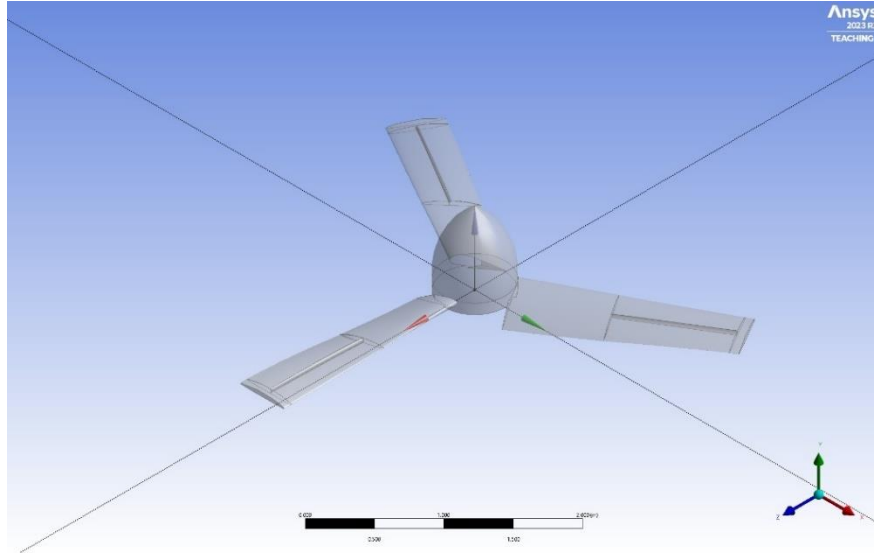


Figure 27: Isometric View of the rotorprop in Ansys Design Modeler.

Immediately, there were two problems we faced in this step. The first problem was the origin of the CAD model not being at the center of the nosecone. When specifying a rotation in Ansys, the model rotates about its origin as defined in the CAD model, regardless of what adjustments are made in the Design Modeler. This was a problem that required the CAD subteam to adjust the models accordingly. The other problem we faced with meshing and geometry modifications originates from this step. It is important to note that the imported geometry must be one single part and cannot be imported as an assembly. The CAD subteam was responsible for making sure that the CFD subteam received models that were a single body “water-tight” geometry. Otherwise, this simulation will not run. AS a part of the workflow, we would check if the geometry was made correctly by looking at the tree outline on the left-hand side of the screen, as seen in Figure 28. We check if the geometry was made correctly by looking at the tree outline on the left-hand side of the screen, as seen in Figure 28.

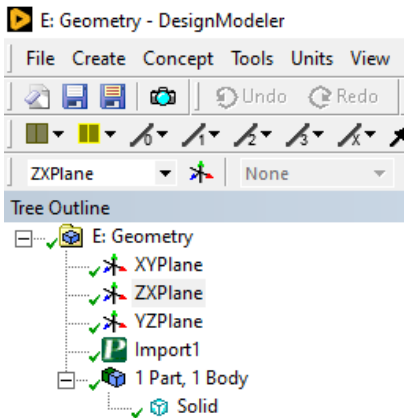


Figure 28: Tree Outline of the geometry in the Ansys user interface.

As seen in Figure 28, the geometry only contains “1 part, 1 body”. This indicates that the model was imported successfully.

After ensuring that the geometry was of good build quality, we began by creating the “rotating domain” around the rotoprop. The purpose of a rotating domain is to accurately simulate the dynamic interaction between propeller blades and the surrounding fluid environment. By incorporating this domain into Fluent simulations, we can precisely model the rotational motion of the propeller blades, providing insights into their speed, direction, and the resulting fluid forces they generate. This approach enables us to study complex fluid-structure interaction phenomena, including the development of boundary layers, wake formation, and vortex shedding, all of which are crucial for understanding propeller performance. Additionally, the rotating domain allows for the calculation of performance parameters such as thrust, torque, and power required, facilitating the optimization of propeller design for enhanced performance and efficiency in real-world applications.

We can create this domain by inserting a primitive cylinder geometry and defining its construction plane according to the orientation of the rotoprop. The rotating domain must include a 15mm “cushion” between the ends of the blades and the domain itself [17], so it is important to note the dimensions of the geometry. The consensus for the gap between nose cone and the underside of the rotoprop and the top and bottom of the cylinder was that it was not as important,

and we approximated the vertical cushion to be about 70mm from the rotoprop. This is seen in Figure 29.

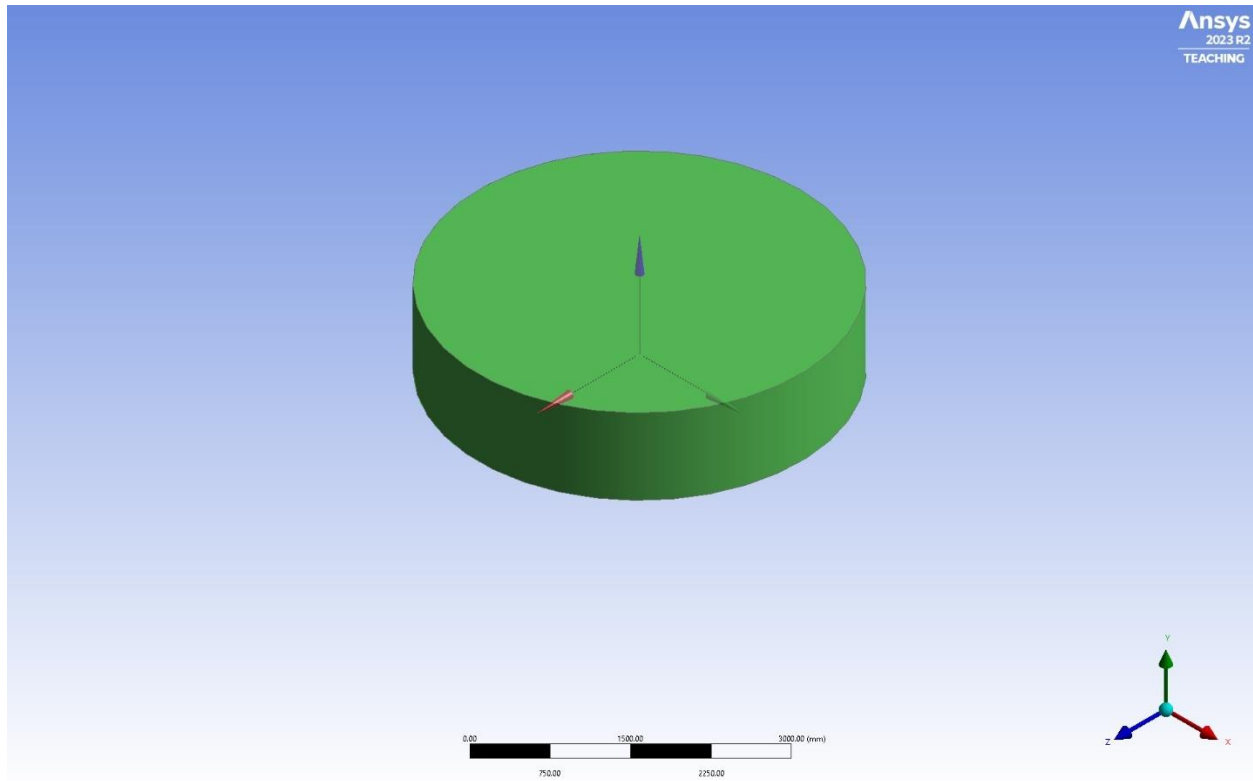


Figure 29: Cylinder Generation over the Rotoprop.

An important piece to note in this step is to make sure that the cylinder was generated under the operation of adding “frozen material”. "Frozen material" in Ansys Fluent refers to a modeling approach where one assumes that the properties of the fluid remain constant and do not change throughout the simulation, regardless of variations in temperature or other factors and in essence, “frozen material” allows us to focus on analyzing fluid flow patterns, turbulence effects, and other aspects of the simulation without the computational burden of tracking changes in material properties. If one is creating this domain using the enclosure feature in Ansys Design Modeler, the program automatically generates the geometry with Frozen material. We can specify the dimensions and the operations type in the detail view of the cylinder generation, seen in Figure 30.

Details View	
[-] Details of Cylinder1	
Cylinder	Cylinder1
Base Plane	ZXPlane
Operation	Add Frozen
Origin Definition	Coordinates
<input type="checkbox"/> FD3, Origin X Coordinate	0 mm
<input type="checkbox"/> FD4, Origin Y Coordinate	0 mm
<input type="checkbox"/> FD5, Origin Z Coordinate	-175 mm
Axis Definition	Components
<input type="checkbox"/> FD6, Axis X Component	0 mm
<input type="checkbox"/> FD7, Axis Y Component	0 mm
<input type="checkbox"/> FD8, Axis Z Component	1000 mm
<input type="checkbox"/> FD10, Radius (>0)	2115 mm
As Thin/Surface?	No

Figure 30: Cylinder Generation Details View in the Ansys user interface.

Next, we generated the box enclosure that will surround both the rotoprop and the cylinder. The purpose of this enclosure is to define the domain used to simulate the rotoprop, something comparable to defining the dimensions of the test section in a wind tunnel. In CFD simulations, the user must define the physical boundaries so in this case, our boundary dimensions were ambiguous and were just made large enough to where we would not have to consider any interactions between the rotoprop and the future walls, as shown in Figure 31.

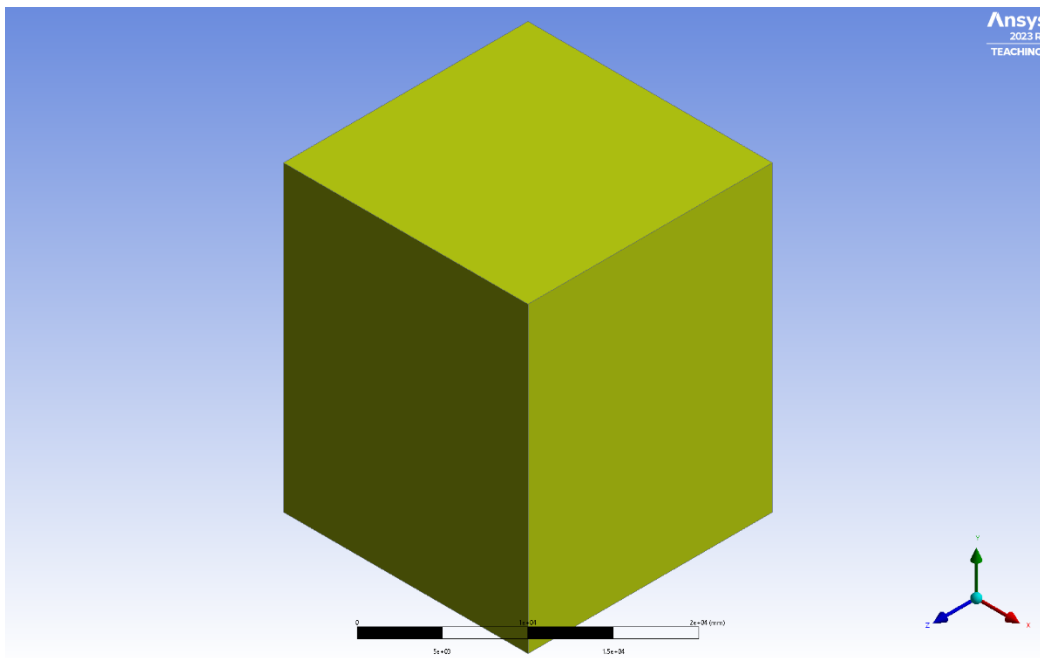


Figure 31: Box Enclosure containing the rotoprop and cylinder.

Details View	
[-] Details of Enclosure1	
Enclosure	Enclosure1
Shape	Box
Number of Planes	0
Cushion	Non-Uniform
<input type="checkbox"/> FD1, Cushion +X value (>0)	8000 mm
<input type="checkbox"/> FD2, Cushion +Y value (>0)	8000 mm
<input type="checkbox"/> FD3, Cushion +Z value (>0)	8000 mm
<input type="checkbox"/> FD4, Cushion -X value (>0)	8000 mm
<input type="checkbox"/> FD5, Cushion -Y value (>0)	16000 mm
<input type="checkbox"/> FD6, Cushion -Z value (>0)	8000 mm
Target Bodies	All Bodies
Export Enclosure	Yes

Figure 32: Box Enclosure Details View.

In our case, it can be seen in the detailed view (Fig. 32) that the box enclosure dimensions were 8000mm x 8000mm x 16000mm, sufficiently larger than the dimensions of the rotoprop.

One of the last steps to prepare the rotoprop for the Ansys Fluent simulations is to add Boolean operations to define relationships between the enclosures the user has defined. A Boolean operation is a mathematical operation used to combine or modify solid geometry shapes, in our case, we used the subtraction operation to combine our generated geometries into a usable model. The first Boolean was used to create the rotating domain. Our rule of thumb for Booleans was that target bodies are on the outside and tool bodies on the inside for a subtraction Boolean operation. So, in this case, the target body was the cylindrical enclosure, and the tool body was the rotoprop. A key thing to note when generating this Boolean is that for the rotating domain, tool bodies are unpreserved, meaning that the original rotoprop geometry will be removed after the Boolean is generated, shown in Figure 33.

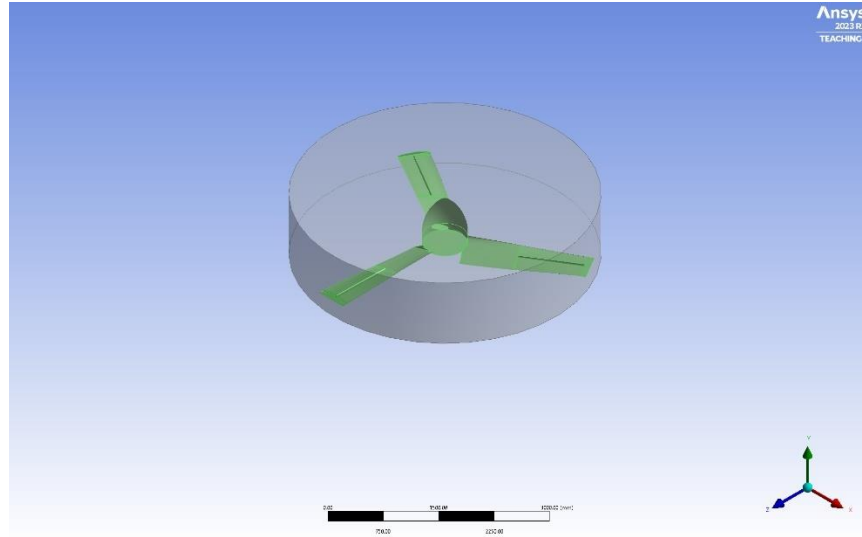


Figure 33: Rotating Domain Boolean.

Details View	
<input type="checkbox"/>	Details of Boolean1
Boolean	Boolean1
Operation	Subtract
Target Bodies	1 Body
Tool Bodies	1 Body
Preserve Tool Bodies?	No

Figure 34: Rotating Domain Detail View in the Ansys user interface.

The second and final Boolean will be used to create the static domain. The purpose of a static domain is to provide a stationary reference frame within a fluid simulation, enabling the analysis of fluid flow and interactions with fixed structures or boundaries. This was also a subtraction operation where the target body was the box enclosure, and the tool body was the newly formed rotating domain solid. A key difference between this Boolean and the last one is that this Boolean will be preserving Tool Bodies. Meaning that the rotating domain part will remain after the Boolean is generated.

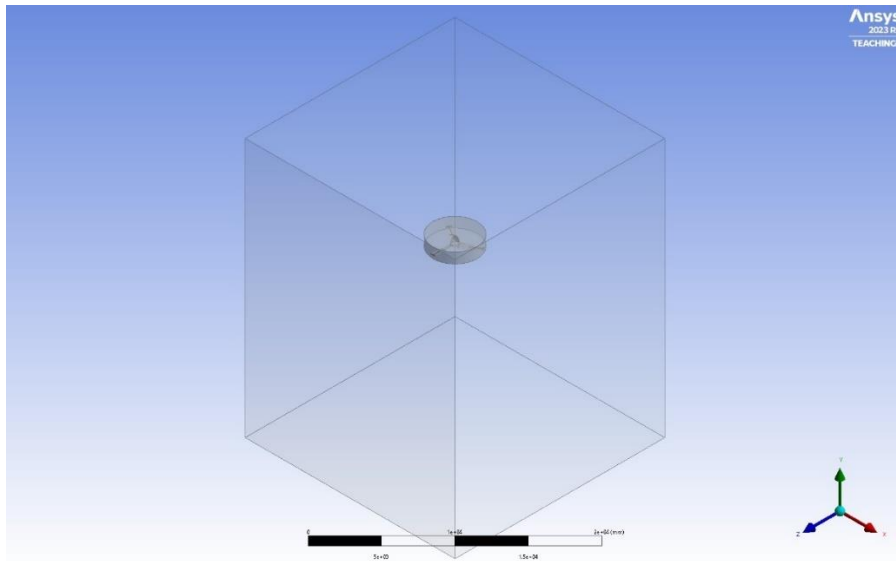


Figure 35: Static Domain Boolean.

Details View	
[-] Details of Boolean2	
Boolean	Boolean2
Operation	Subtract
Target Bodies	1 Body
Tool Bodies	1 Body
Preserve Tool Bodies?	Yes

Figure 36: Static Domain Boolean Detail View in the Ansys user interface.

After the geometries and Booleans are generated, the final Design Modeler tree outline contains five geometries including the imported rotoprop geometry and in total two parts, two bodies.

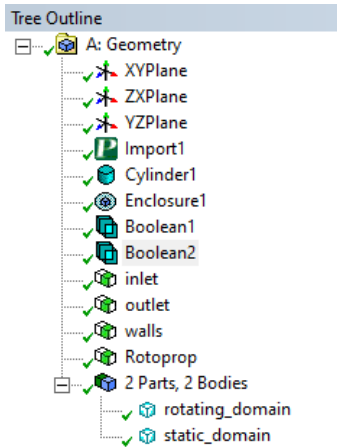


Figure 37: Final Design Modeler Tree Outline in the Ansys user interface.

A final thing to note is that during this step of the Ansys Fluent setup, if using Fluent Meshing rather than Ansys Meshing the named selections will have to be defined this step.

5.2.2 Meshing

After proceeding with the Ansys Fluent simulation setup, the subsequent task involves creating a mesh for the model. As the initial simulation method yielded unsatisfactory results, we opted to explore alternative approaches in pursuit of a more acceptable outcome. Specifically, we employed two distinct mesh generation applications provided within the Ansys Software Suite: Ansys Meshing and Fluent Meshing.

Ansys Meshing is a comprehensive mesh generation tool provided within the Ansys software suite. It allows users to create meshes for various types of simulations and includes advanced features such as boundary layer meshing, mesh morphing, and mesh refinement to enhance mesh quality and accuracy. Although the tutorials we followed gave us a rough estimate for the methodology and approximate mesh sizing, this step still required the majority of our time and effort to thoroughly complete. We began this process by inserting a face sizing section on the rotating domain.

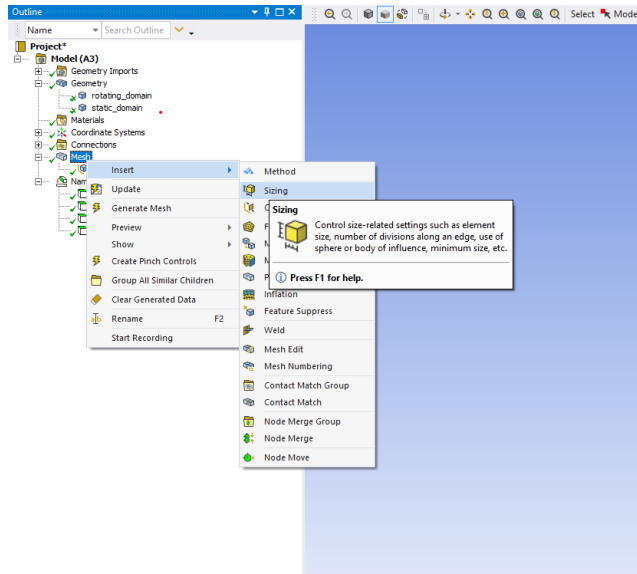


Figure 38: Inserting Face Sizing in the Ansys user interface.

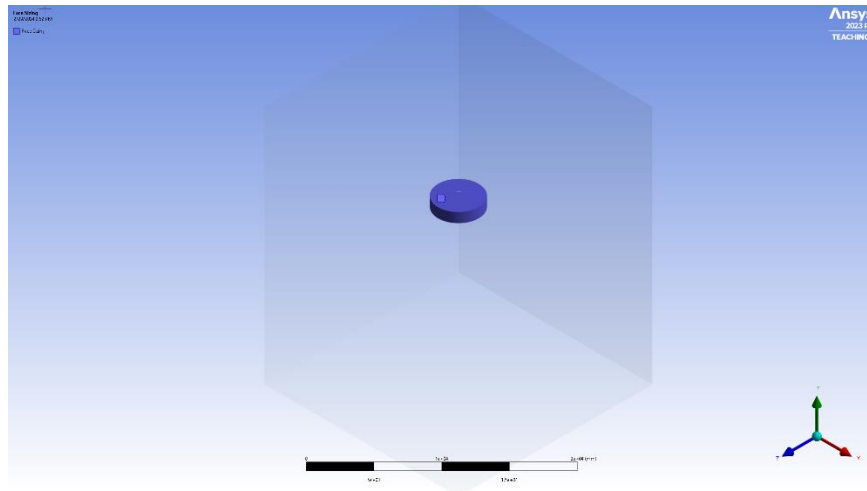


Figure 39: Face Sizing Geometry

It is important to note that when selecting the part of the geometry for (mesh) face sizing the face selecting mode option is selected on the top task bar. This allowed us to select multiple individual faces rather than the volume or body of a geometry. The purpose of face sizing is to gain the ability to control the mesh density specifically on selected faces or regions of the geometry. This allows for finer mesh resolution in areas of interest, such as near boundaries, geometric features, or regions of anticipated sharp gradients or flow disturbances. For our simulation, we defined the element size in face sizing on the rotating domain to be 160mm which

can be seen in Figure 40.

Details of "Face Sizing" - Sizing	
Scope	
Scoping Method	Geometry Selection
Geometry	130 Faces
Definition	
Suppressed	No
Type	Element Size
<input type="checkbox"/> Element Size	160.0 mm
Advanced	
<input type="checkbox"/> Defeature Size	Default (1.6 mm)
Influence Volume	No
<input type="checkbox"/> Growth Rate	Default (1.15)
Capture Curvature	Yes
<input type="checkbox"/> Curvature Normal Angle	Default (18.0°)
<input type="checkbox"/> Local Min Size	Default (3.2 mm)
Capture Proximity	No

Figure 40: Face Sizing Detail View in the Ansys user interface.

Then after defining the face sizing element size, we had to also define the model's overall element sized which we set to be 320mm as seen in Figure 41. The overall element sizing with be used to adjust the sizing of the mesh on faces other than the rotoprop such as the static domain.

Details of "Mesh"	
Display	
Display Style	Use Geometry Setting
Defaults	
Physics Preference	CFD
Solver Preference	Fluent
Element Order	Linear
<input type="checkbox"/> Element Size	320.0 mm
Export Format	Standard
Export Preview Surface Mesh	No
Sizing	
Use Adaptive Sizing	No
<input type="checkbox"/> Growth Rate	1.15
<input type="checkbox"/> Max Size	480.0 mm
Mesh Defeaturing	Yes
<input type="checkbox"/> Defeature Size	Default (1.6 mm)
Capture Curvature	Yes
<input type="checkbox"/> Curvature Min Size	Default (3.2 mm)
<input type="checkbox"/> Curvature Normal Angle	Default (18.0°)
Capture Proximity	No
Bounding Box Diagonal	37993 mm
Average Surface Area	2.1549e+007 mm ²
Minimum Edge Length	3.7708e-002 mm

Figure 41: Mesh Detailed View in the Ansys user interface.

Additionally, the mesh detail views gave us additional options when it came to mesh generation. There was a significant amount of experimentation that was done with these settings, but we found the most success at generating a complete mesh when these values we kept as close to default as possible. We had multiple issues with geometry shaping and mesh sizing throughout this entire process but through trial and error were eventually able to determine a series of settings that allowed the mesh to generate. On multiple occasions we would try generating a mesh that resulted in either a failed mesh and/or an obsolete mesh which would be unusable for running the simulation. To clarify, an obsolete mesh refers to a mesh that is no longer suitable or effective for its intended use due to changes in the simulation setup, geometry, boundary conditions, or mesh quality considerations. Adjusting the mesh growth rate allowed us to create finer mesh sizes on the rotoprop but at the same time allowed us to keep the static domain mesh sizing coarse without sacrificing the concentration of mesh cells. We set our growth rate at 1.15 as seen in Figure 41 which is 0.05 less than that of the default value (1.2). This also had the added benefit of keeping our mesh more consistent throughout the static domain volume outside of the rotoprop as seen in Figures 42 and 43.

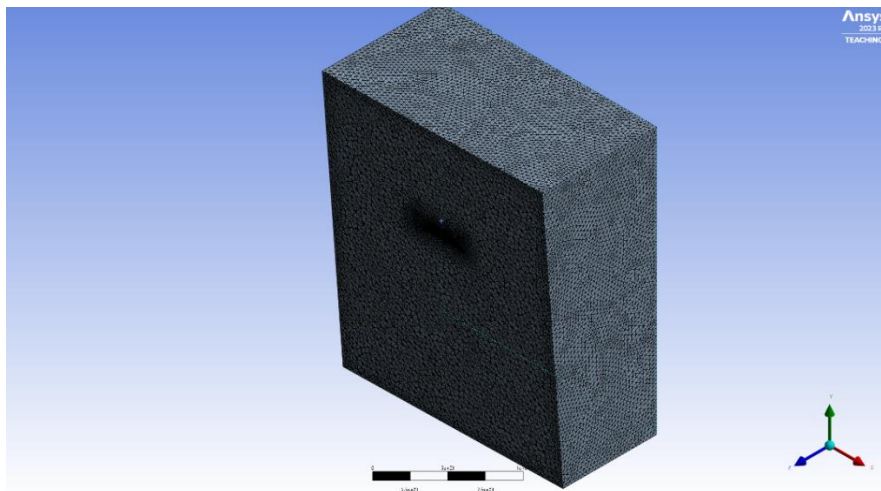


Figure 42: Mesh Isometric Section View

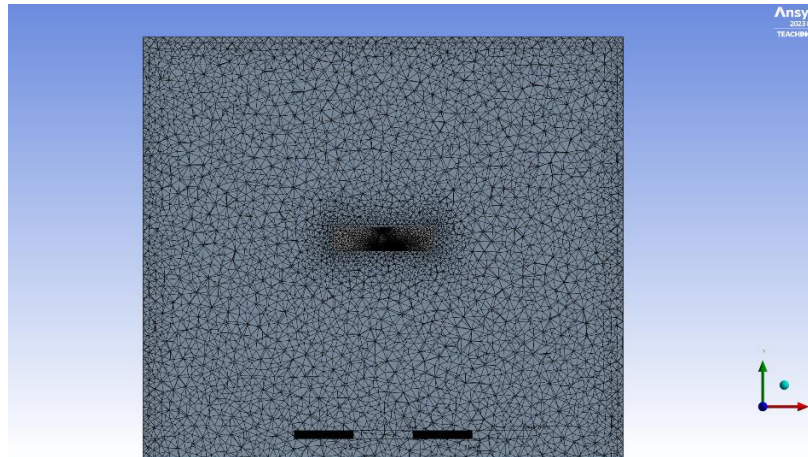


Figure 43: Mesh Section View

After generating the mesh, it was critical to ensure that the quality of the mesh met the requirements for CFD simulations. In CFD simulations, higher quality meshes are imperative for accuracy, convergence, and stability. These meshes provide finer resolution of flow features, including boundary layers and vortices, leading to more precise results that better reflect real-world behavior. In this context, boundary layers refer to the region of flow near solid boundaries where mesh refinement is applied to accurately capture flow behavior. This is achieved through the creation of prism layers or boundary layer elements aligned with the solid boundary. Additionally, high-quality meshes ensure better convergence, reducing the likelihood of numerical instabilities and improving simulation stability. We checked the quality of the mesh by displaying the mesh quality worksheet which can be seen in Figures 44 and 45.

Error Check	Quality Criterion	Warning Limit	Error (Failed) Limit	% Warning	# Warning	% Failed	# Failed	Average	Worst
<input type="checkbox"/>	Max Aspect Ratio	Default (0)	Default (1000)	7.866 %	433021	0 %	0	2.53	477.35
<input type="checkbox"/>	Min Element Quality	Default (0.005)	Default (0e-04)	0.149 %	7844	3.0e-05 %	2	0.764	0
<input type="checkbox"/>	Min Orthogonal Quality	Default (0.005)	Default (0e-03)	0.013 %	702	0 %	0	0.756	% 1e-03
<input type="checkbox"/>	Max Skewness	Default (0.6)	Default (0.999)	0.037 %	1933	0 %	0	0.242	0.99

Figure 44: Ansys Meshing Quality Worksheet 1 in the Ansys user interface.

Error Check	Quality Criterion	Warning Limit	Error (Failed) Limit	% Warning	# Warning	% Failed	# Failed	Average	Worst
<input type="checkbox"/>	Max Aspect Ratio	Default (0)	Default (1000)	0.072 %	175	0 %	0	1.204	10.166
<input type="checkbox"/>	Max Skewness	Default (0.6)	Default (0.999)	0.031 %	75	0 %	0	0.098	0.994

Figure 45: Ansys Meshing Quality Worksheet 2 in the Ansys user interface.

Unfortunately, regardless of the mesh generation settings we changed we could not get the

minimum orthogonal quality and for this setup we accepted that failure in this was one category would be unavoidable.

Due to the lack of success from our Ansys Meshing setup, we also attempted to run the same simulation but generating a geometry mesh utilizing Ansys Fluent Meshing. Ansys Fluent Meshing is a computational tool within the Ansys Fluent software suite designed for generating high-quality meshes for fluid flow simulations. It provides automated meshing capabilities, allowing users to efficiently create meshes for complex geometries without manual intervention. Ansys Fluent Meshing employs advanced algorithms to generate meshes that accurately capture geometry features and boundary conditions, ensuring accurate and reliable simulation results. This tool streamlines the meshing process, reducing simulation setup time, and enabling engineers and researchers to focus more on analyzing and interpreting simulation results rather than on mesh generation.

The user interface for Ansys Fluent Meshing is very similar to that of the Ansys Fluent simulation setup where each step is broken down in chronological order to make defining the mesh settings far easier to see. The first step in this process was to define the computational resources allowed to be used by the Ansys Fluent and Fluent Meshing software which can be seen in Figure 46. In our case, we dedicated four processors to our simulation. We also enabled double precision, which enables the use of double point floating numbers, reducing round off errors. Enabling this mode is particularly useful for ensuring reliable results in simulations requiring high levels of precision, such as those involving complex geometries or high Reynolds number flows.

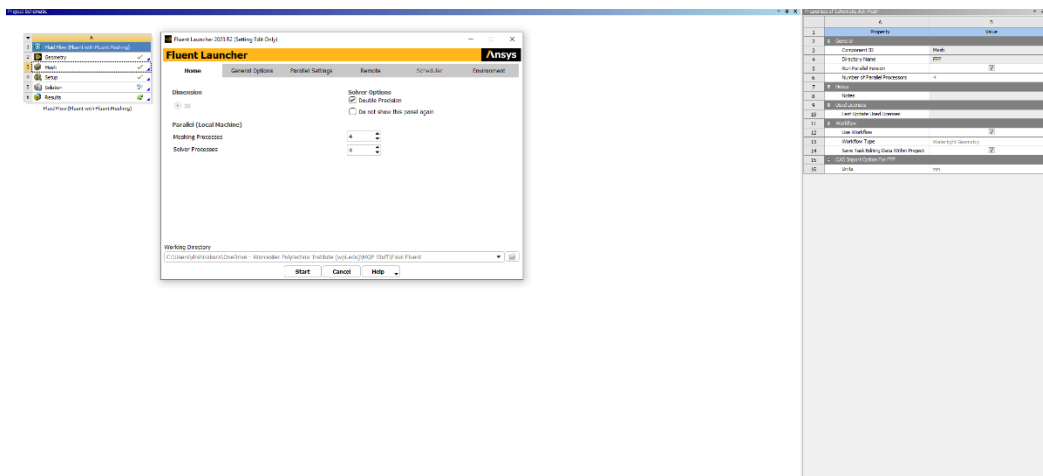


Figure 46: Ansys Fluent Meshing Start Up in the Ansys user interface.

After starting the Ansys Fluent Meshing software, the first step was to import the geometry as seen in Figure 47.

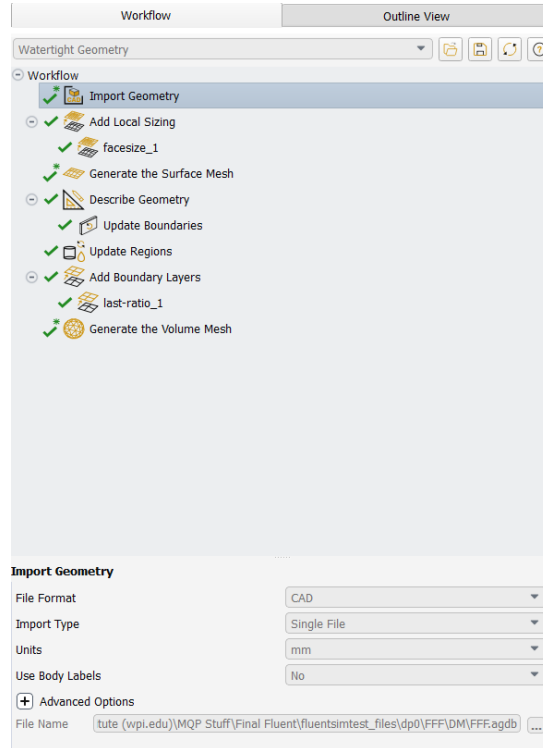


Figure 47: Ansys Fluent Meshing Import Geometry in the Ansys user interface.

After that we had to add and define any local sizing on our geometry, similar to the procedure that was followed for Ansys Meshing. We defined the target mesh size for the rotoprop face sizing to be 4 mm as seen in Figure 48.

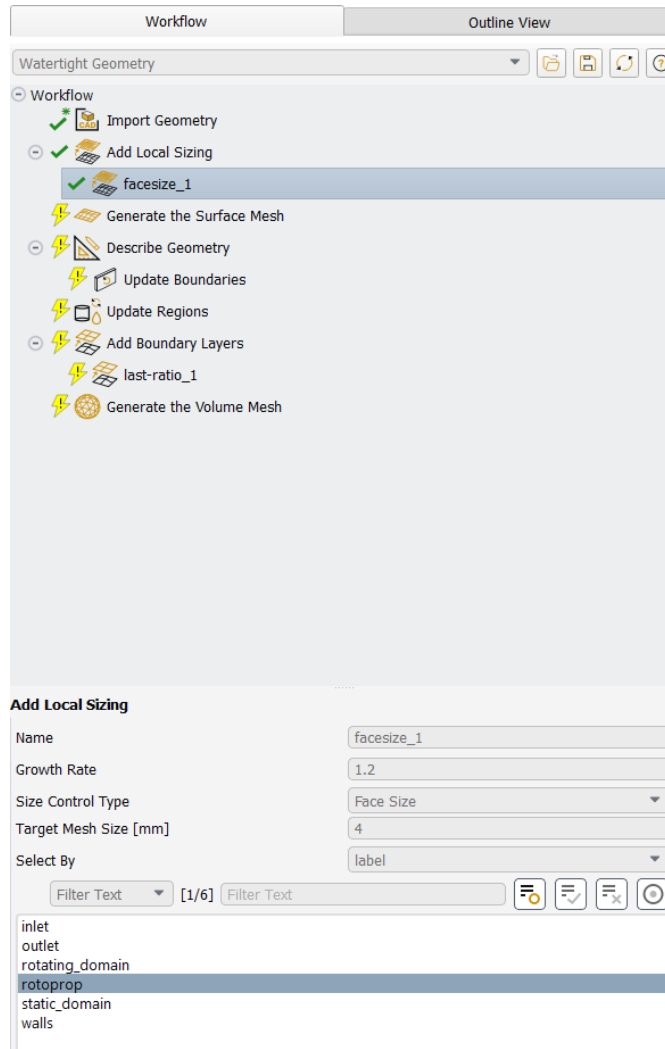


Figure 48: Face Sizing Detail View in the Ansys user interface.

After defining the face sizing dimension, we then were able to generate the surface mesh with the settings that can be seen in the detailed view in Figure 49.

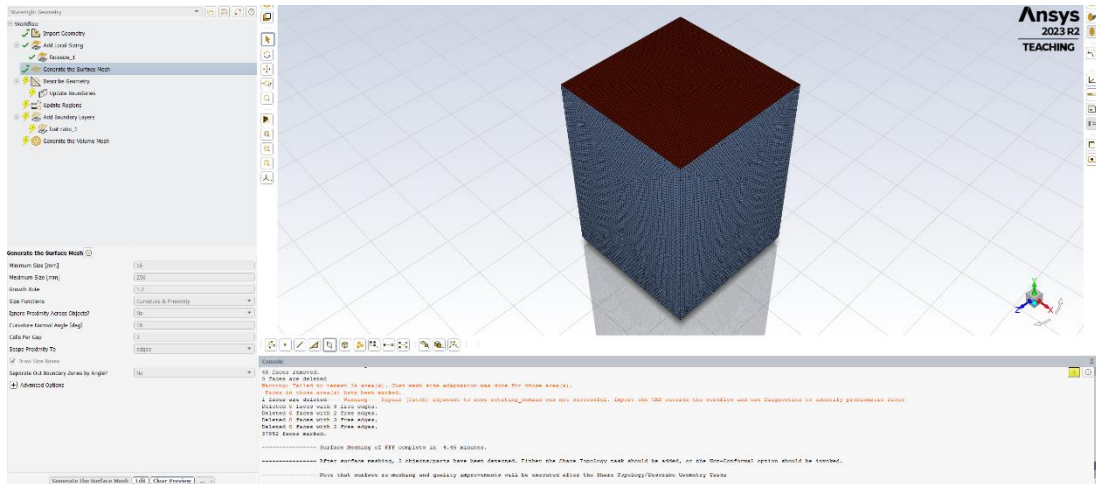


Figure 49: Generated Surface Mesh

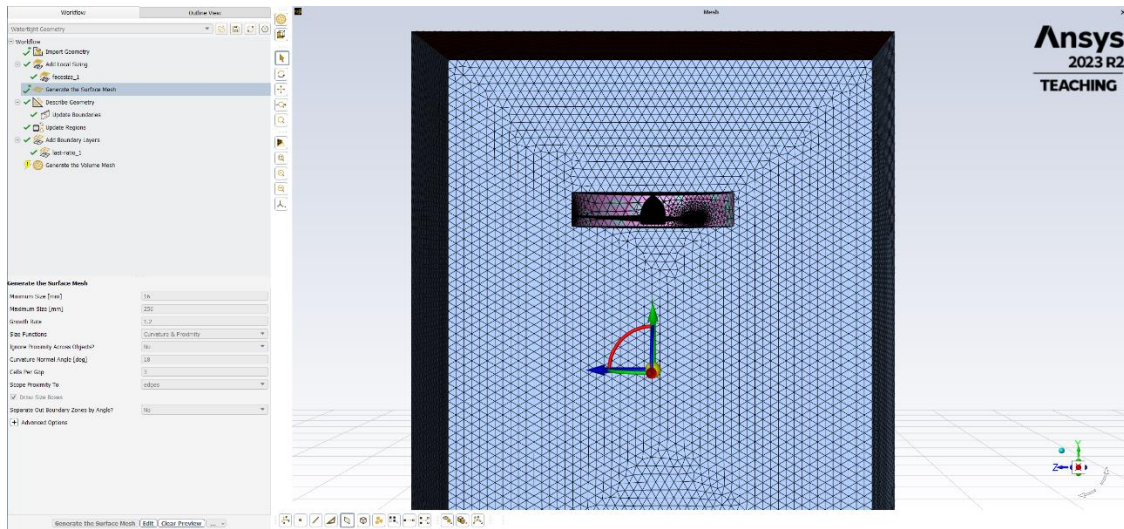


Figure 50: Generated Surface Mesh Section Plane

After the surface mesh is generated, we then had to describe the geometry where we would select the option that best fit the description of the model which was that geometry consisted of only fluid regions with no voids.

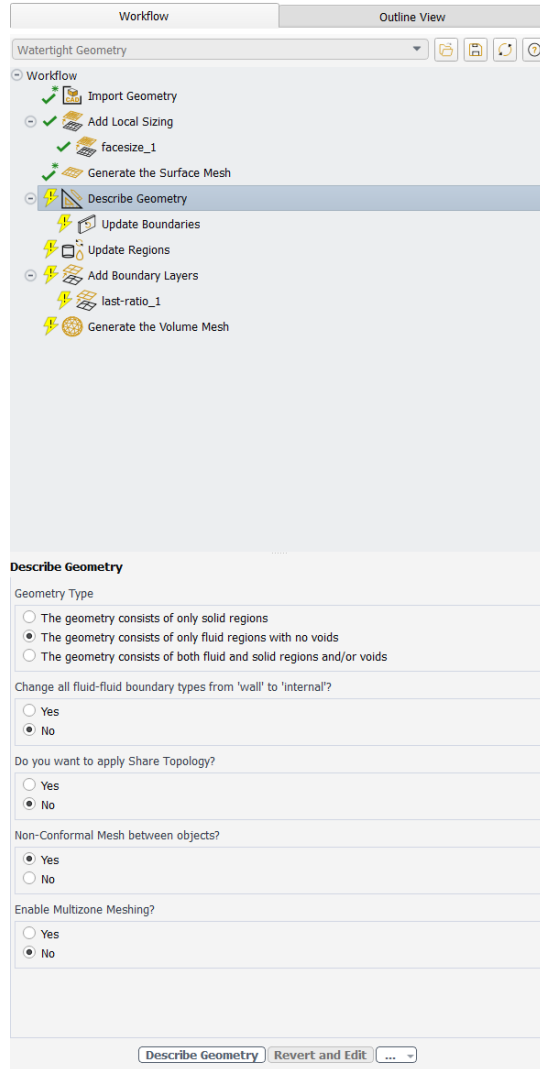


Figure 51: Fluent Meshing Describe Geometry in the Ansys user interface.

Then we could update the boundary and define the regions of the simulation utilizing the named selections we created in design modeler so that they could be directly imported into the Ansys Fluent Solver which can be seen in Figures 52 and 53.

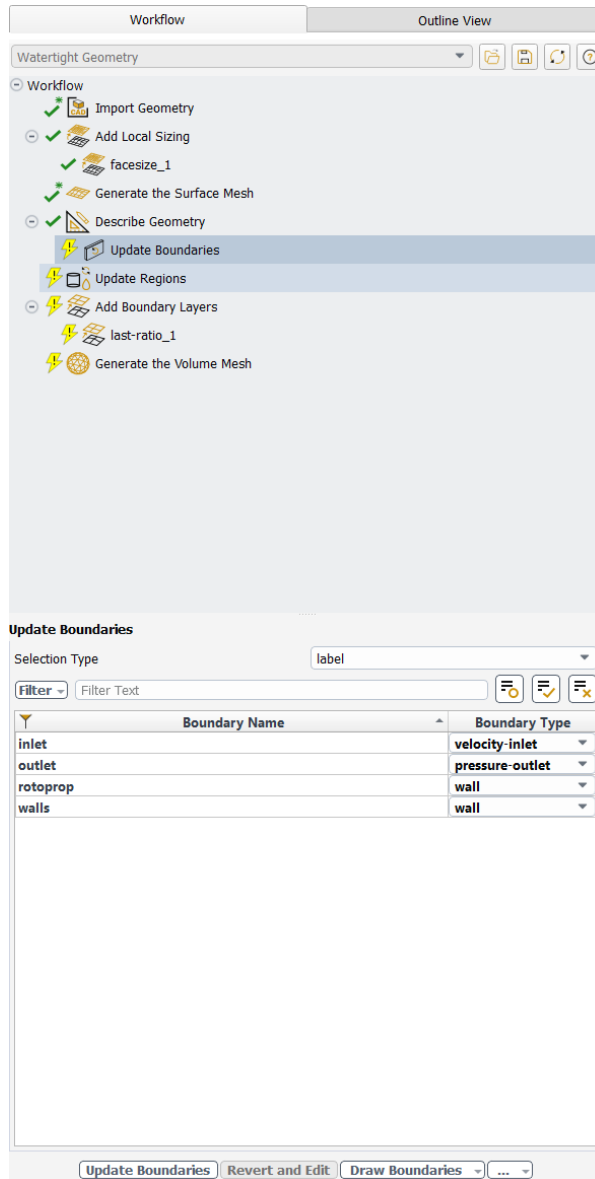


Figure 52: Fluent Meshing Update Boundaries in the Ansys user interface.

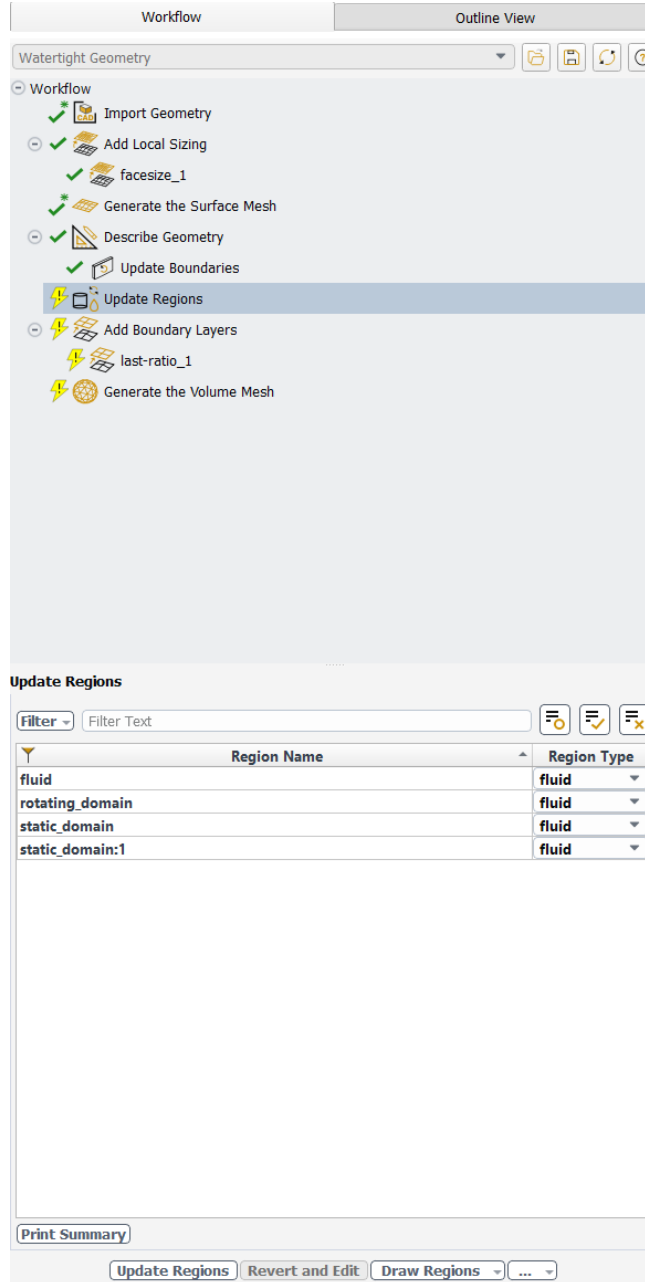


Figure 53: Fluent Meshing Update Regions in the Ansys user interface.

One of the main benefits of Ansys Fluent Meshing is that it allows it to define boundary layers more easily and quickly on the surfaces of the model. For our case we attempted to generate seven boundary layers utilized the last ratio method on the surfaces of the rotoprop. The "Last Ratio" method for adding boundary conditions in Ansys Fluent refers to a technique used to specify boundary conditions based on the ratios of the physical quantities at the boundary. This method

proved to be particularly useful because the exact values of the boundary conditions were not known but their ratios relative to other quantities could be estimated. The values that we used to generate the boundary layers can be seen in Figure 54.

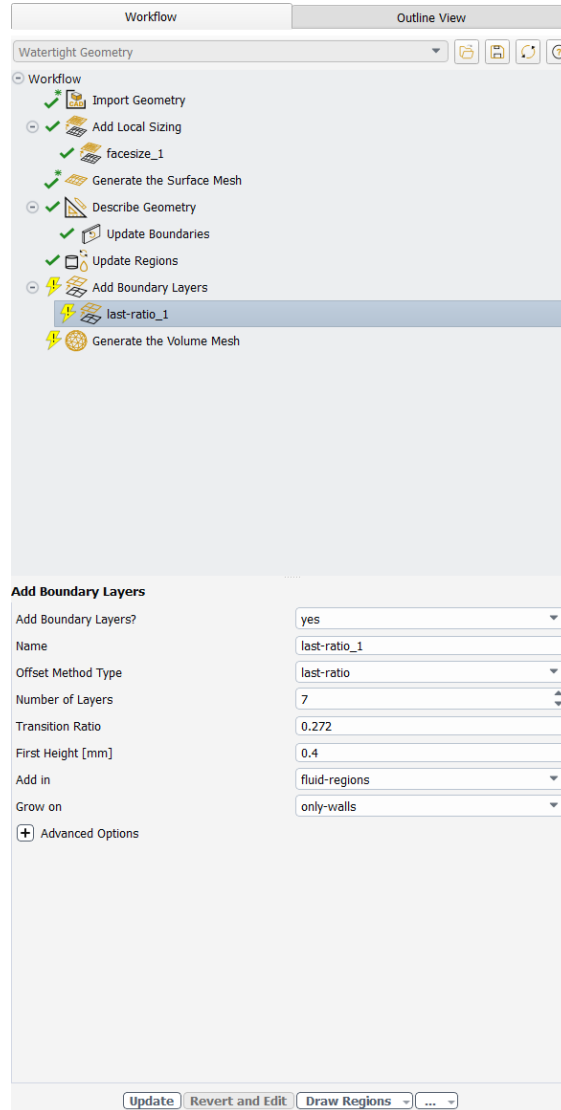


Figure 54: Fluent Meshing Adding Boundary Layers in the Ansys user interface.

The final step for the Fluent Mesh generation was to generate the volume mesh for the model. This step is the most difficult part of the process to result in success and took multiple tries like the Ansys Mesh to generate properly. The generated volume mesh and its quality can be seen in Figure 55.

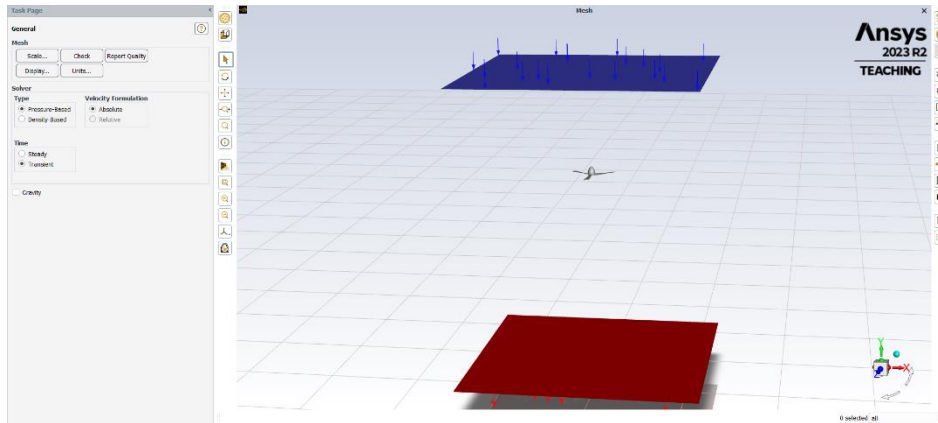


Figure 56: General Solver Setup

As discussed earlier, the simulation used the $k-\epsilon$ turbulence model; this is specified under the viscous model section in the Fluent setup which can be seen in Figure 56. We opted to use the $k-\epsilon$ turbulence model. This is a very standard turbulence model, appropriate for turbulent streams far from boundary walls.

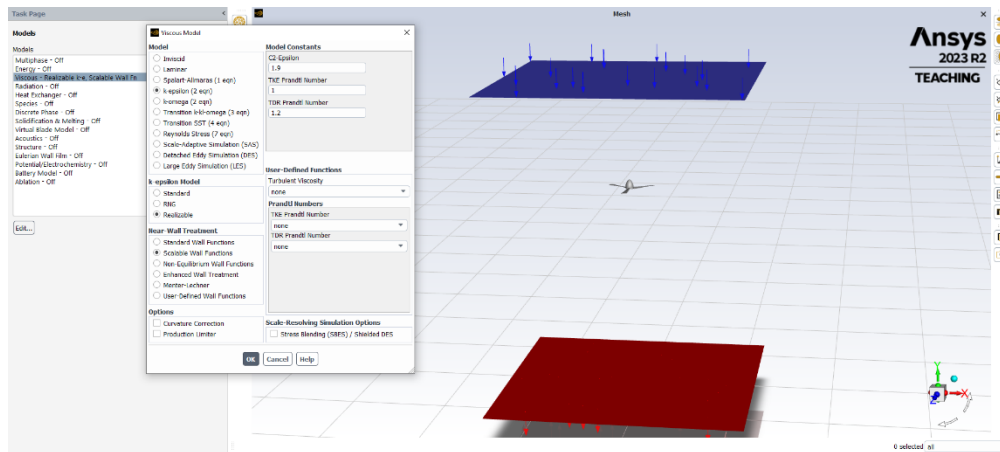


Figure 57: Viscous Model Definition.

Then we defined the materials that will be used for the simulation, in this case, the main fluid was air and the solid material for the walls was aluminum. We determined that the effect of the wall material on the result of the simulation was negligible and therefore left the material of the solids as the default which can be seen in Figure 58.



Figure 58: Fluent Setup Materials in the Ansys user interface.

We then defined the cell zone condition for this simulation. In this step, we input the free stream velocity and rotational speed of the propellers. We utilized mesh motion which refers to the capability of dynamically altering the mesh during a simulation to account for changes in the geometry, boundary conditions, or flow field. This feature allows for the simulation of moving or deforming domains, such as rotating machinery, oscillating structures, or fluid-structure interaction problems, ensuring accurate representation of the transient behavior of the simulation. The details of the cell boundary conditions can be seen in Figure 59.

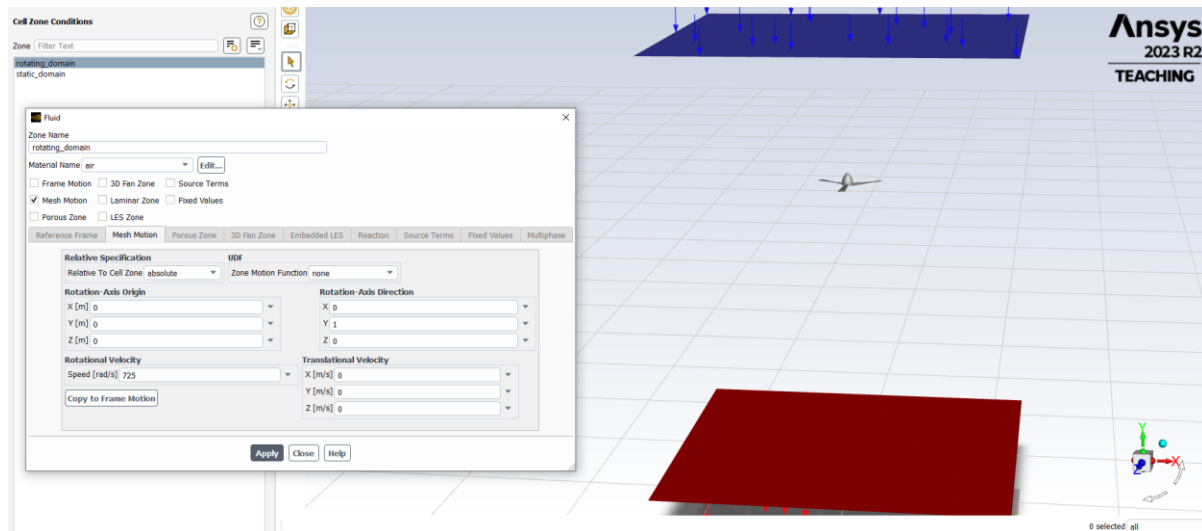


Figure 59: Fluent Setup Cell Zone Conditions in the Ansys user interface.

After the cell zone conditions were defined, we could then define the boundary conditions of the fluent simulation setup mainly the inlet velocity which can be seen in Figure 60. An important component of determining the inlet velocity value is specifying the tip speed ratio which is a critical parameter in Fluent analysis of propellers because it directly influences the

performance and efficiency of the propeller. It is defined as the ratio of the speed of the propeller blade tips to the speed of the fluid flow. Understanding and optimizing the tip speed ratio is essential for achieving desired propeller performance characteristics such as thrust, efficiency, and cavitation avoidance (in the case of flows through liquids). In our case, this calculation allowed us to make a rough estimate for our inlet velocity which we needed to define in our boundary conditions set up which can also be seen in Figure 60. The tip speed ratio is defined as:

$$\text{TSR} = \frac{wR}{v} \quad (17)$$

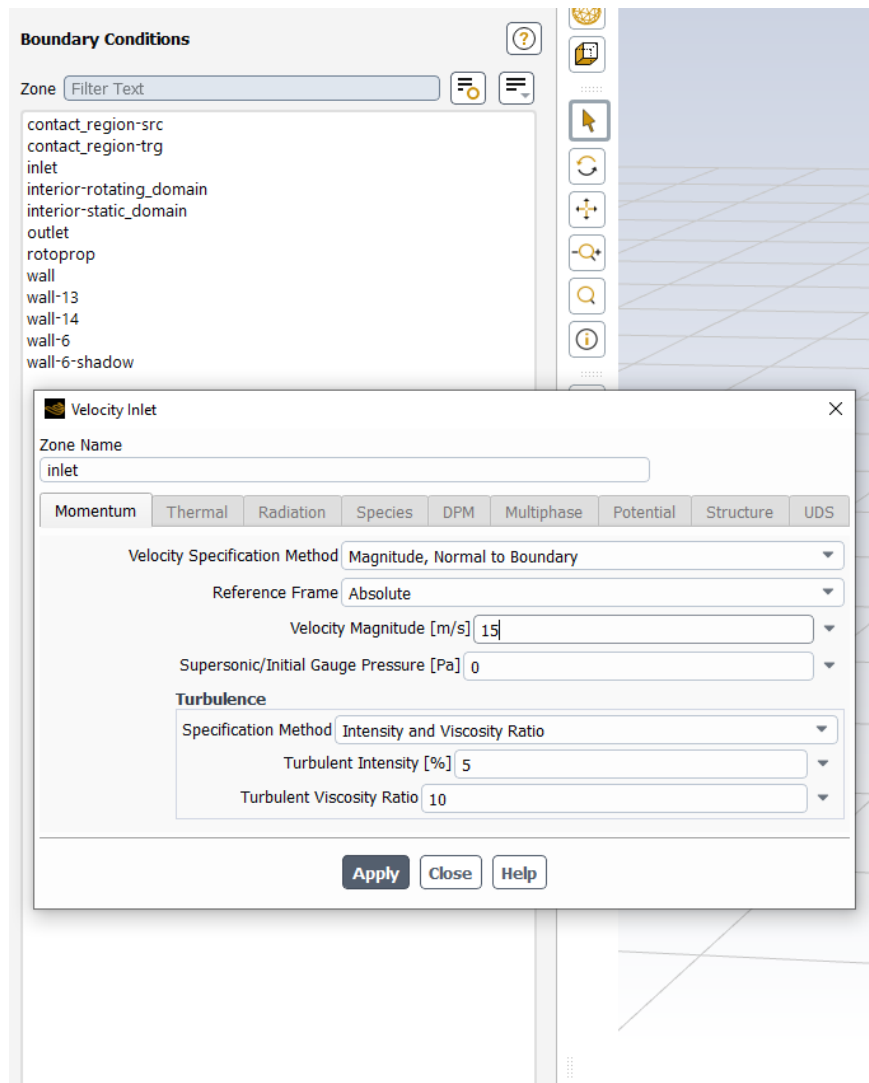


Figure 60: Boundary Conditions Setup in the Ansys user interface.

Once the necessary solution values are known, we could define the report definitions for

this simulation. Report definitions are predefined sets of data that specify the quantities and locations where data should be collected during a simulation. These reports are used to monitor and analyze various parameters such as flow variables, forces, and heat transfer coefficients at specific points or regions within the computational domain and streamline the post-processing phase by automatically generating reports containing the desired data. In our case, we want to generate a report that will produce the thrust force that rotprop produces which can be seen in Figure 61.

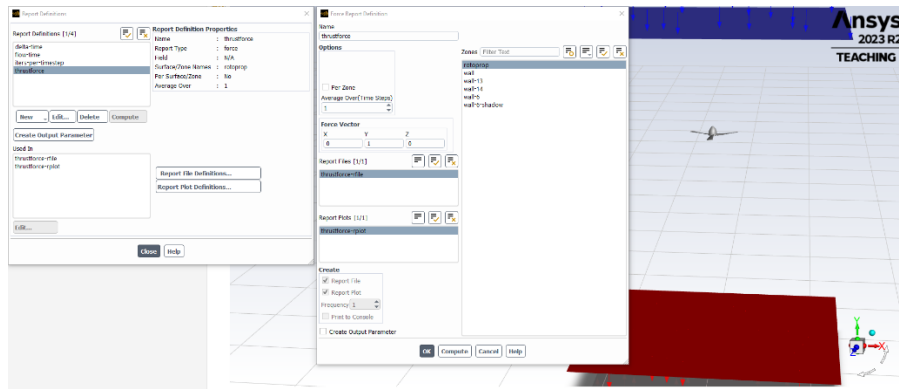


Figure 61: Report Definitions Setup in the Ansys user interface.

The next step after defining the needed reports was to define the solution methods that the model will utilize to produce an accurate simulation. Solution methods in Ansys Fluent refer to the algorithms and numerical techniques used to solve the governing equations of fluid flow and heat transfer. These methods include finite volume, finite element, and finite difference methods, which discretize the governing equations into algebraic equations that can be solved iteratively. For this case, we left these models set to the default selection as changing any of the options had little to no effect on the result of the simulation. The default solution methods can be seen in Figure 62.

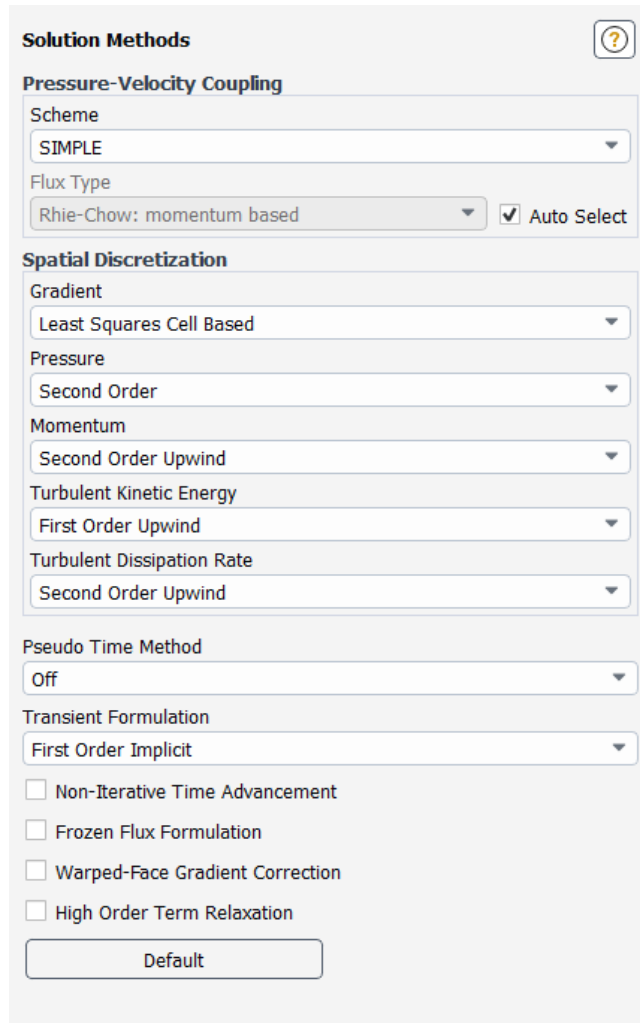


Figure 62: Solution Models Setup in the Ansys user interface.

We then finally were able to initialize the simulation which sets the initial conditions for the simulation before starting the main iterative solver and running the simulation which can be seen in Figures 63 and 64.

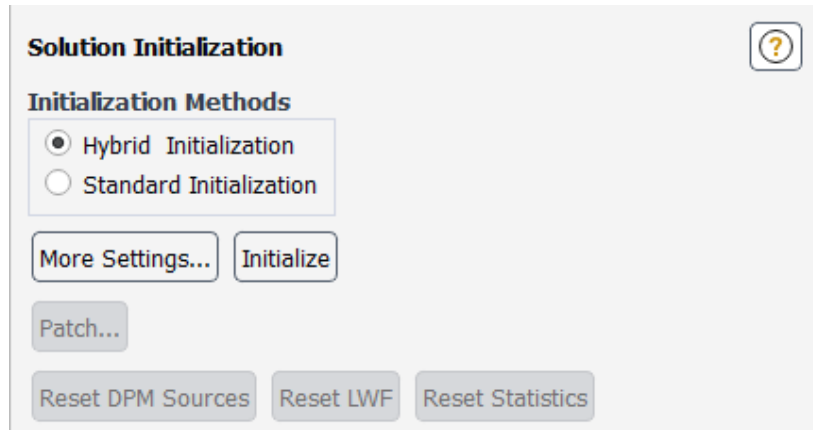


Figure 63: Fluent Simulation Initialization in the Ansys user interface.

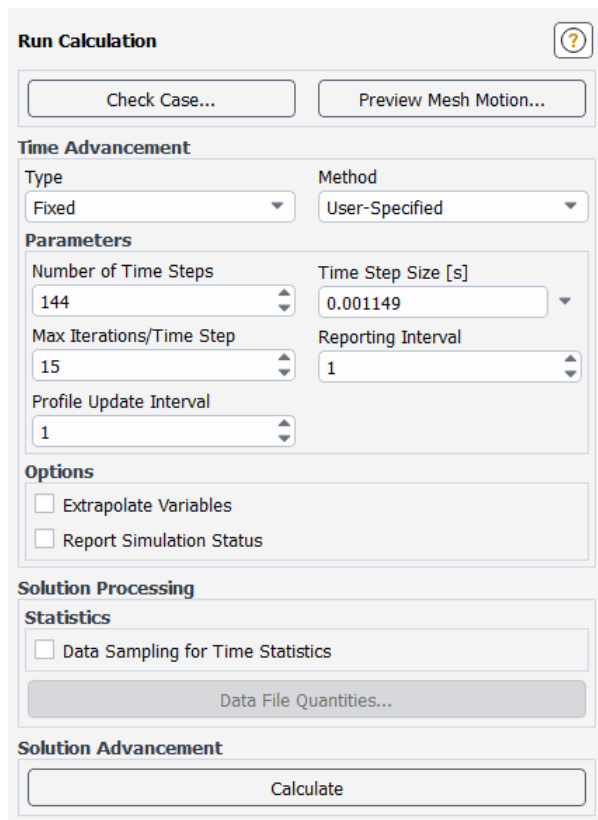


Figure 64: Run Simulation Setup in the Ansys user interface.

The time steps need to be small enough for the simulation to produce valid results. Since the simulation runs in a discretized manner, the propeller cannot “jump” from one location to another that is too far in one frame. Then, enough time-steps need to be run to ensure that the propeller settles into an equilibrium state. A visualization of this concept can be seen in Figure 64.

Then from the size of the time step we can then determine the number of time steps we required to revolve a certain number of times, in this case, twice.

5.2.4 Full Rotoprop Approach Conclusion

Overall, even though simulating the full propeller motion seems to be one of the more popular approaches analyzing the aerodynamic capabilities of a propeller [17], the results of our simulation using this approach were inconclusive. The Ansys Fluent simulation found the rotoprop to be generating over 400,000 N of thrust almost 40 times greater than our expected value of around 10,000 N. Our generated results can be seen in Figure 65.

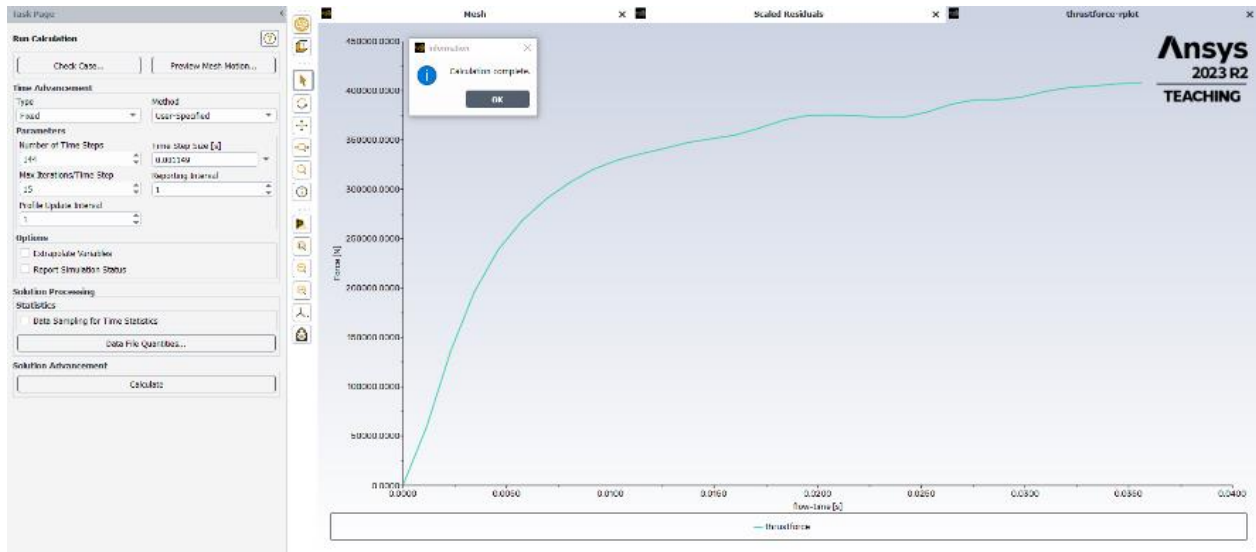


Figure 65: Ansys Meshing Thrust Solution

Unfortunately, an even more unsuccessful result for the Fluent Meshing simulation ended up producing an error that can be seen in Figure 66. The simulation would continue to do this regardless of the simulation set-up and it was concluded that this error was a result of some meshing inconsistencies that may have been missed by the Fluent Meshing quality check.

The team concluded that this approach using a rotating mesh and including the entire rototprop was not solving correctly so an alternative approach was needed.

5.3 Single-Blade Approach

Because we were unable to obtain realistic results from the full rototprop approach, the next step was to schedule a meeting between the CFD subteam and WPI Professor Hera. She advised that we simplify the simulation further by modeling a single blade of the rototprop. To guide the team through simplifying our simulation, Professor Hera directed us to a free course provided on the Ansys Innovation Courses website where a blade of a wind turbine was analyzed [5]. The tutorial analyzed the power output of a wind turbine by simulating one blade in Ansys Fluent. The guide was most helpful with designing the geometry, and determining how the boundary conditions and rotation were modeled in this single blade simulation. The team combined their original single blade approach with the advice of Professor Hera. This simplified approach proved to be easier to run and gave us realistic results.

The number of simulations we were able to run was severely limited by the project deadline, therefore the team had to reduce the parameter space of our simulations. If time was not an issue with this project, we would have tested a large number of blade pitch angles, collective flap angles, and engine rpms. However, the team decided to test blade pitch angles of 15, 30, and 45 degrees, collective flap angles of 0 and 13 degrees, and only one engine speed at 725 rpm. Later, once the results had been collected there was still more time left to run cases. With the extra time we were able to run one more case with a collective flap angle of 7 degrees only at a blade pitch angle of 30 degrees.

5.3.1 Geometry

In Section 5.2, the importance of designing solid models specifically for Fluent purposes was emphasized. The solid model features that resulted in the most errors were sharp features, spline features, and gaps in the geometry. When meshing a solid object for a Fluent simulation,

Fluent simulates the fluid flow over the outer surface of an object, therefore prior to importing a solid model to Fluent, it must be made “watertight” with no gaps in its surfaces. With the rotoprop CAD models being created from images of blueprints, there were small inconsistencies that posed challenges during the Fluent meshing process. To solve this issue, the CAD and CFD subteams collaborated to identify problematic features and modify these features to obtain a usable Fluent model. Through many iterations and simplifications, the CAD subteam created three single-blade models with varying collective flap deflections that would successfully mesh and produce realistic results.

To create the geometry, first a single blade of the rotoprop was imported into Ansys SpaceClaim and centered on the origin with the span of the blade in the positive y-direction. Then the blade’s pitch angle was set by drawing the chord line on the root of the blade and rotating the blade about the y-axis to the desired angle. In Figure 68, the rotated blade can be seen with its root highlighted to better visualize how the angle was measured.

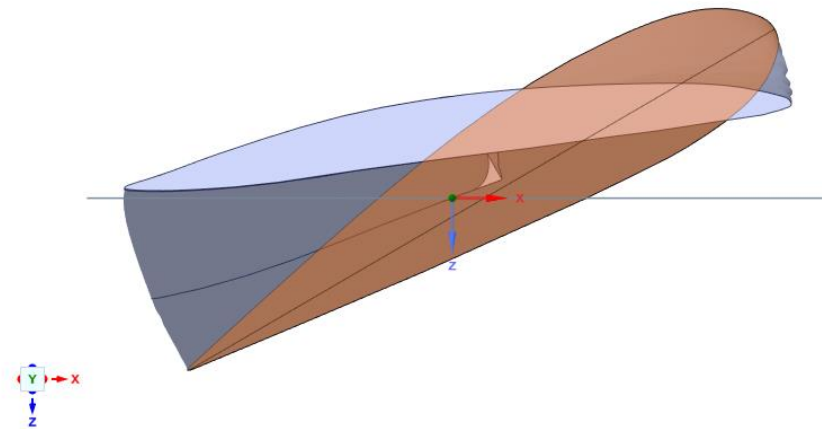


Figure 68: Top-Down View of Setting the 30° Blade Pitch relative to the root

To ensure the blade was rotating correctly in the simulation, the center hub of the rotoprop must be accounted for by moving the blade in positive y-direction by 313mm. This distance of 313mm was the measured distance from the root of the blade to the center of the hub in the rotoprop solid model that the blade was taken from. After the blade was correctly set up, the enclosure was

sketched in the x-y plane. Since the simulation is designed to model one third of a rotoprop, a 120° arc enclosure is necessary. The radius of enclosure needed to be 2.5 times the length of the blade to guarantee that all the flow conditions were analyzed [5]. Our blade was 2073mm long, therefore, the radius of the arc was set to 5183mm. Two radii were created, each at an angle of 30° to the x-axis. These two radii were connected by the three-point arc tool in SpaceClaim, completing the 120° arc enclosure sketch. This sketch with its dimensions can be seen in Figure 69.

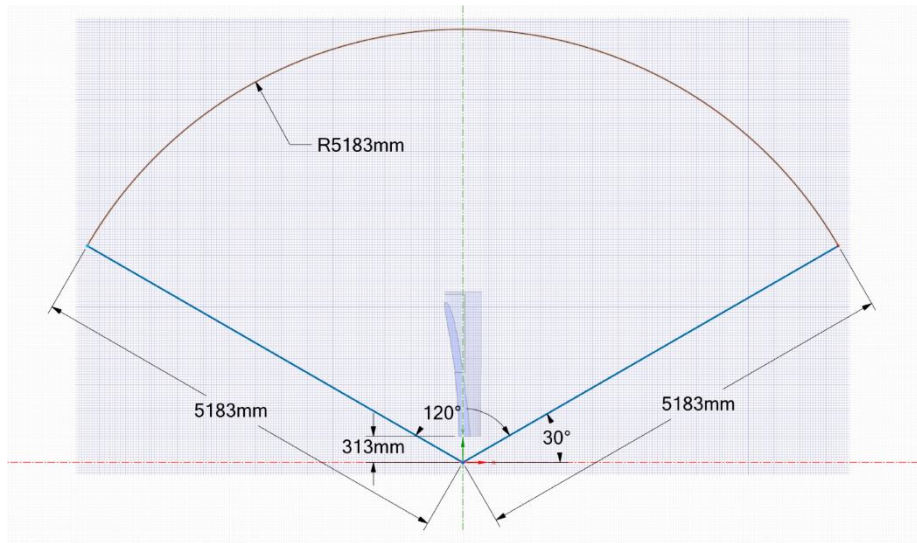


Figure 69: Dimensions of the Enclosure Sketch

After creating the sketch, the enclosure was extruded in both directions on the z-axis with the “No Merge” option selected to ensure the blade’s geometry is not deleted by the extrusion. The inlet face of the enclosure is also two and a half blade lengths in front of the blade, and the outlet face is five blade lengths behind the sketch plane. The distance to the outlet from the blade is longer than the distance to the inlet because the flow characteristics after interacting with the blade are of interest whereas the flow ahead of the blade is less important. The fully extruded enclosure is shown in Figure 70.

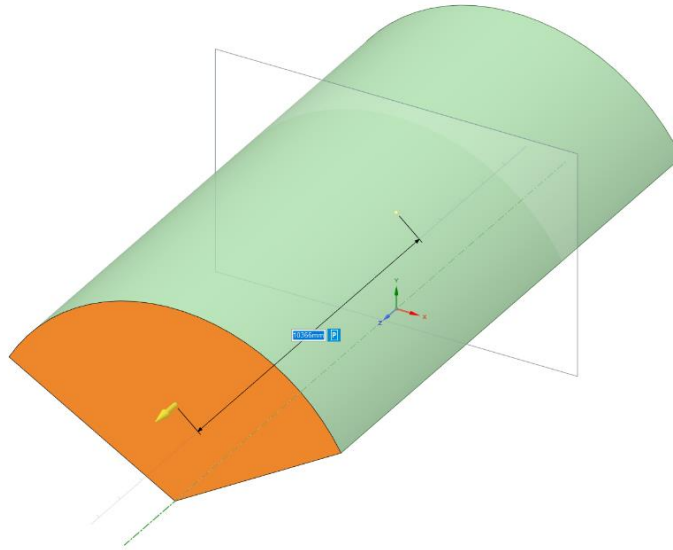


Figure 70: Extruded Enclosure

To simplify the simulation, the blade geometry must be subtracted from the enclosure. This subtraction keeps the geometry of the blade in the simulation, while decreasing the number of bodies that fluent must simulate. This was completed using a Boolean operation which is called the “Combine” feature in SpaceClaim where the enclosure was selected as the “Target Body”, and the blade was selected as the “Cutter Object”. An important step in this subtraction is disabling the “Keep Cutter Object” option in the “Combine” feature, because this allows the solid model of the blade to be deleted from the simulation while keeping the impression of its geometry on the enclosure body, seen in Figure 71.

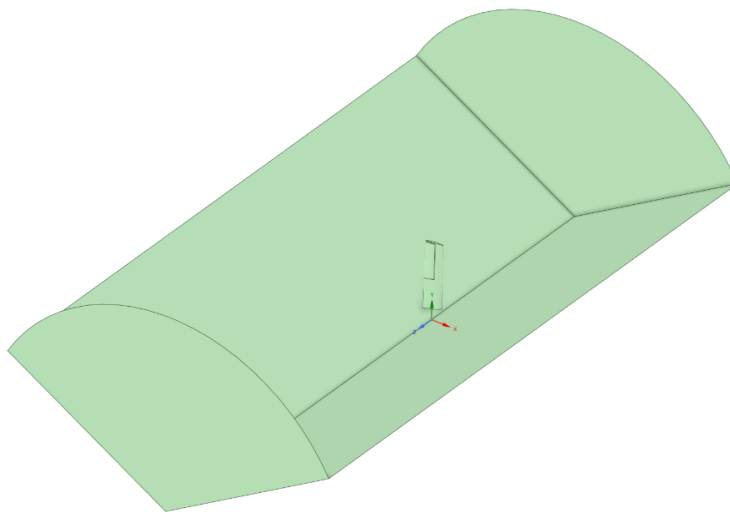


Figure 71: Final Geometry of the Simulation with the Top Face Hidden

The final step in setting up the geometry is to create “Named Selections” for each of the faces of the enclosure. By using “Named Selections”, Ansys can better predict the purpose of certain faces of the enclosure when creating boundary conditions. The face in the negative z-direction from the blade is the inlet, and in the positive z-direction is the outlet. The top face hidden in the final geometry (Fig. 71) is also named as an inlet, and this face is used later in the setup to maintain the freestream velocity at the boundary of the enclosure. The two angled walls are named periodic boundaries and help the simulation accurately model the rotation of the rotoprop without the other two blades. To set up these periodic boundaries correctly, the wall that is in the direction of the blade’s rotation is named “periodic_1”, and the other boundary is named “periodic_2”. Finally, with all the previously described walls hidden, all faces of the blade geometry are selected and named “blade”. These named selections will carry through each part of the simulation and make it easier to set up.

5.3.2 Creating A Mesh

The tutorial used for the single-blade approach recommended using the “Fluent with Fluent Meshing” analysis system to mesh its model. However, due to prior difficulties with this meshing approach, we decided to use the “Fluent” analysis system that meshes its models through Ansys’ meshing approach. The main difference between these two approaches is that Fluent meshing will first create a surface mesh on the watertight geometry, then create the volume mesh after. Whereas meshing through Ansys does not differentiate these steps.

In total there were seven simulations run under the single-blade approach, and each simulation had to be individually meshed because the blade pitch angle was set in the geometry part of the simulation. The only mesh size specification was “Face Sizing” on the blade. This mesh sizing was utilized to ensure the small details of the blade would be accurately meshed, while allowing the mesh sizing of the enclosure to be larger and not create a dense mesh on unimportant features. Every simulation had the same meshing setup, however the sizes used in each simulation

varied. These variations were due to slight differences in the geometry originating from the subtraction of the blade into the enclosure. While there were only three blade models imported into Ansys, the Combine feature in SpaceClaim has a finite precision and may not be able to imprint every detail from the blade onto the enclosure. The mesh sizes used in each simulation are detailed in Table 7.

Mesh Sizes used in each Simulation			
Simulations	Pitch_Flap	General Sizing (mm)	Face Sizing (mm)
	15_0	160	4
	15_13	160	40
	30_0	160	80
	30_7	160	20
	30_13	160	40
	45_0	160	40
	45_13	160	80

Table 7: Mesh Sizing Used in Each Simulation

The general meshing size was applied to the enclosure walls and did not pose any problems, therefore for all simulations the general element size remained at 160 mm. Due to the inconsistencies created from the Boolean operation in SpaceClaim, the face sizing needed to be modified to ensure the blade could be accurately meshed with minimal defeaturing. If Ansys encounters difficulties when meshing a specific feature, it will selectively delete small portions of the model and create a mesh as close to the original model as possible. The most common causes of defeaturing were complex curves, sharp edges, and the minimum element size being too large.

When meshing each simulation, the first face mesh sizing was set from 40 to 80 mm, if this first sizing failed the face sizing was decreased until all the blade features were accurately meshed. A successful blade mesh can be seen in Figure 72.

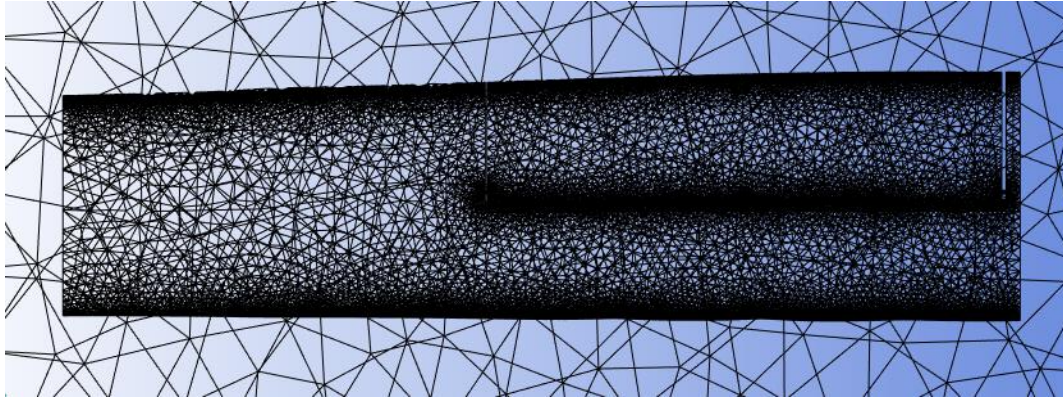


Figure 72: Bottom Face of Accurately Meshed Blade set at 30° Pitch and 0° Flap Angles

The successful blade mesh shown in Figure 72 is representative of the other meshes used in the rest of the simulations. The simulations with smaller face sizing had more elements and higher mesh densities throughout the blade. The simulations with a greater number of elements resulted in significantly longer run times to complete the same number of iterations. As shown in Figure 72, the blade mesh was most dense on the leading and trailing edges, the collective flap's leading edge, and the blade face closest to the flap's leading edge. The mesh primarily became denser in these regions to accurately mesh the curvature of the blade, and other minute details. Outside of these edges, the rest of the blade's mesh is much less dense.

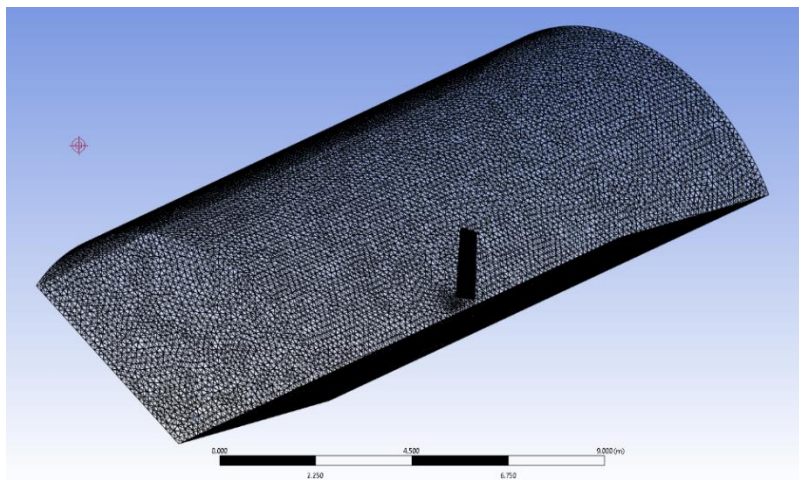


Figure 73: Example of Successfully Meshed Full Enclosure

For all seven simulations, each enclosure mesh was identical to the mesh shown in Figure 73. Since the general sizing remained constant, the enclosure mesh also remained constant. Most

of the problems with mesh generation occurred on the faces of the blade, therefore all the differences between meshes in each simulation are in the blade mesh.

5.3.3 Setup

Once the model for a simulation has been successfully meshed, the last step before running the simulation is to define the operating conditions of the system. The options in the “Setup” task are used to define every quality the user wants to control in their simulations. Only a select few of the options were modified for our single-blade approach, and any other options not mentioned in the following section were left as default. Some of the options, such as the solver type, viscous model, and cell zone conditions were taken from the tutorial discussed in Section 5.3.1.

The first option in the Setup window is to determine the solver type, the solver can either use pressure- or density-based equations and be set to a steady state solution or a transient solution. For the single-blade approach we used pressure-based equations with steady state assumptions. We chose to use a steady solver type, because we were not interested in the transient nature of the blade and any startup sequences of the simulation. The steady solver is best used when analyzing the long-term behavior of a simulation, which matched our goal. The next option was to choose the viscous model, which helps predict more complex flow characteristics especially when pertaining to turbulence. The tutorial used the Generalized $k-\omega$ turbulence model, which yielded favorable results and instilled confidence in our selection of the model. While the turbulence model choice is unlikely to significantly impact the outcome of the simulation, should our simulation’s flow characteristics pose a challenge for the selected model, we were prepared to change the model. Fortunately, the generalized $k-\omega$ model produced results that were both realistic and within the anticipated range.

Accurate material definitions play a pivotal role in the simulation setup process, ensuring that Fluent appropriately categorizes different bodies as either fluid or solid during the simulation. There is a section for defining the materials in the setup phase, however due to the simple nature of this simulation we were able to ensure the enclosure was modeled as a fluid under the “Cell-Zone Conditions” section. The rotation of the simulation is defined in the Cell-Zone Conditions as

“Frame Motion” instead of “Mesh Motion”. To define the Frame motion, the rotation speed, origin, and axis of rotation are necessary inputs. For all the simulations we ran, the rotational speed was set to 725 rpm about the negative z-axis of Fluent’s coordinate system. The Cell-Zone Conditions window with the options for frame motion of the enclosure is shown in Figure 74.

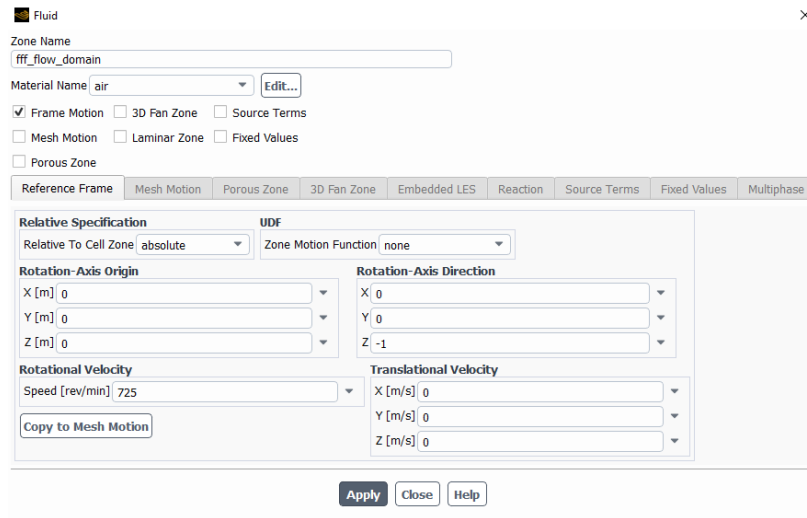


Figure 74: Frame Motion Options under Cell Zone Conditions in the Ansys user interface.

After the rotation of the simulation is defined, the next step is to define all of the boundary conditions. The named selections from creating the geometry become much more important in this phase of the simulation. By naming the outlet of the enclosure as “outlet” and the inlet as “inlet”, it helps Fluent predict the type of boundary condition that is applied at the face. The only faces that need to be defined are both inlets. The top face of the enclosure and the other inlet face both define the freestream velocity, and for our simulations we used 15 m/s solely in the direction of the positive z-axis. The outlet was defined as a pressure outlet, with no inputs required outside of the ambient pressure, and 1 atm was used for our simulations. Finally, each of the “periodic” faces were able to be modeled as walls in the simulation. The inlet boundary conditions window is shown in Figure 75.

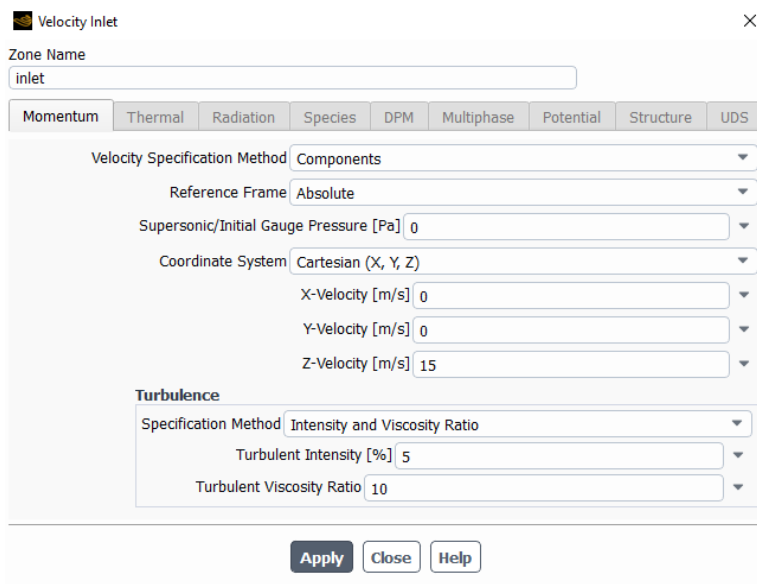


Figure 75: Boundary Condition Options for the Inlet

The next step in the process is to create report definitions, which fill a crucial role in the simulation. These reports are used to plot the solution at each iteration as the simulation simulates the model, serving to assess the convergence quality over time. In our simulations, the only report definition selected was to plot the force produced by the blade in the z-direction. Pressure can also be set as a report definition; however, each report definition will create a plot seen later in Figure 78. These plots report only one value for the desired quantity, and since the pressure needs to be evaluated over the blade surface it only adds time to the simulation setup to add a pressure report definition. All flow characteristics are solved by Ansys Fluent, and do not need a report definition to output a quantity, therefore all pressure characteristics can be gathered in post-processing.

Before running the calculation portion of the simulation, the simulation must be initialized. The initialization step assigns each computational cell with a value serving as an initial guess for the solver. For this approach, standard initialization was computed from the inlet, and the window used for this step can be seen in Figure 76. This step does not take much time to complete, but it is crucial to the simulation running correctly.

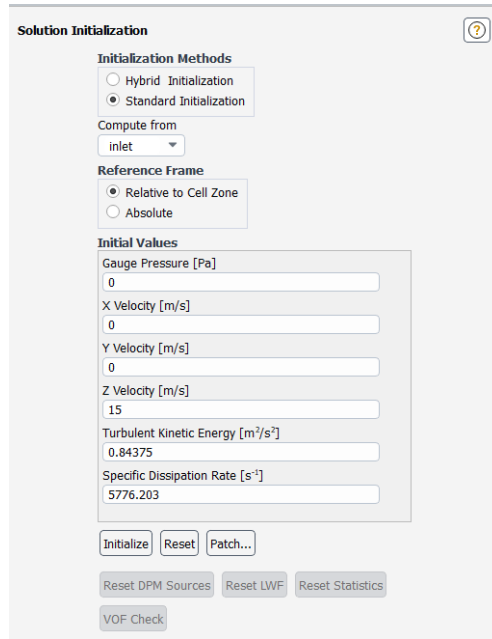


Figure 76: Standard Initialization Window Computed from the Inlet

The last step of the setup is to set the number of iterations and run the calculation. Under the steady solver type, all the fluid time scale settings are automatically determined by Fluent. This ensures that the simulation is running at its steady state when the first iteration is solved. Nearly all our simulations were run for 1500 iterations, with a select few runs extended to assess whether additional iterations would lead to better convergence. The “Data File Quantities” button above the “Calculate” button in Figure 77 is used to export certain solutions from the Fluent simulation to other Ansys simulations. This was used to export the correct pressure data that was used in the static structural analysis simulations.

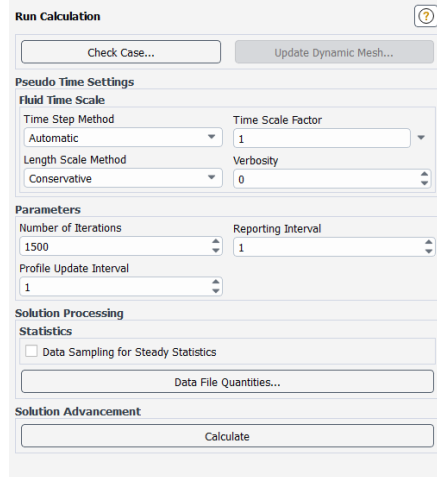


Figure 77: Sample “Run Calculation” Window

5.4 Results

The goal of utilizing Ansys Fluent for this MQP was to analyze the thrust characteristics of the rotoprop. Of the two approaches detailed in Sections 5.2 and 5.3, the single-blade approach proved to be more successful at producing consistent solutions and good convergence on these solutions. In this section these results will be presented and analyzed.

Before analyzing the results, the importance of convergence must be further discussed. Convergence in an Ansys simulation is used to evaluate the stability and reliability of the solution. In a case of perfect convergence, the numerical solution must not significantly change with subsequent iterations. Analyzing the convergence of a solution is the first step in analyzing results from Ansys, because if the simulation is unable to converge to a solution in an allotted number of iterations, then the solution has little credibility. An example of the best convergence our simulations reached can be seen in Figure 78.

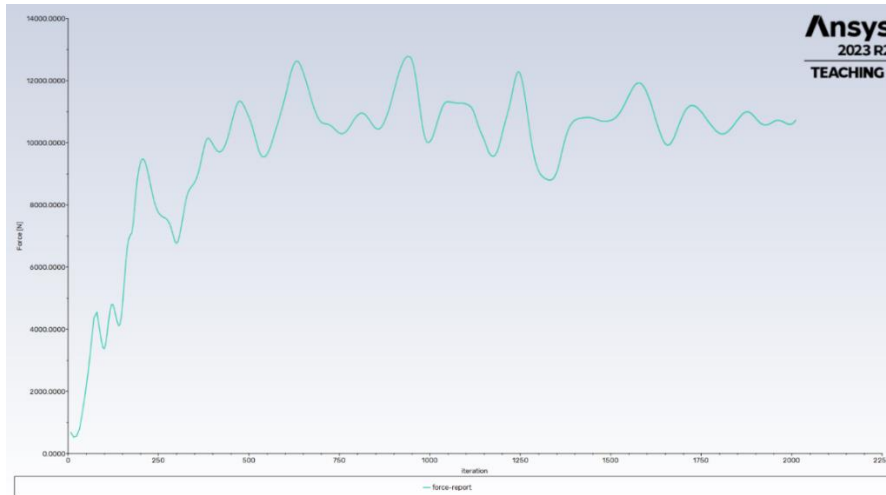


Figure 78: Force vs. Iterations Plot for the Blade at the 30° Pitch and 7° Flap Angles

The convergence in our simulations remained relatively constant after 1500 iterations, with one outlier being the 30° pitch angle and 7° collective flap angle, seen in Figure 78. This plot shows the best convergence any of our simulations reached, and at around 2000 iterations the amplitude of each oscillation decreased until the plot reached the solution. With the quality of the convergence shown above, we can be much more confident that our solution is accurate and credible. Figure 79 is an example of the convergence seen in the other six simulations.

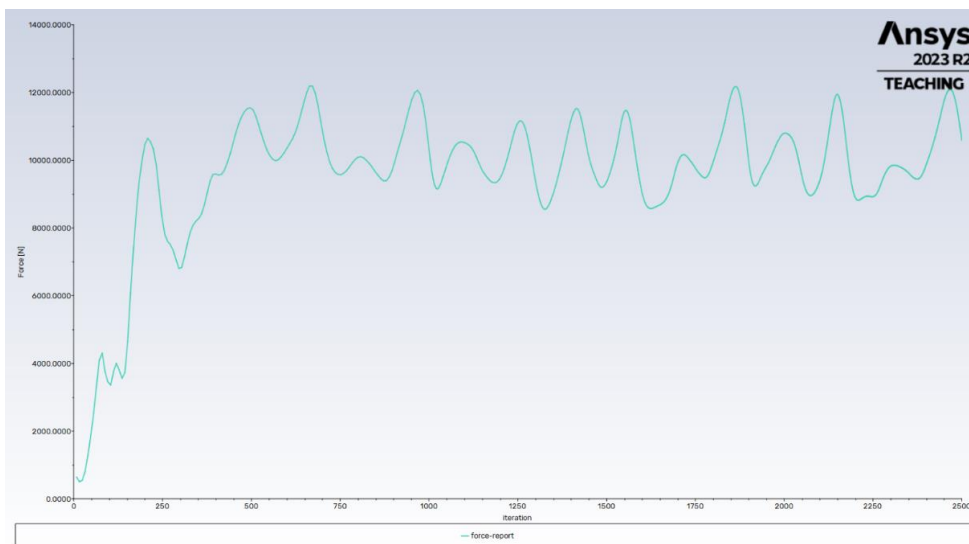


Figure 79: Force vs. Iterations Plot for the Blade at the 30° Pitch and 13° Flap Angles

While the convergence seen in Figure 79 is not perfect, the solution oscillates between a range of 10000 to 12000 N for over 2000 iterations. To determine the necessary number of iterations for improved convergence, a few simulations were run for 2500 iterations. The convergence of these cases can be seen in Figs. 78 and 79. The case with better convergence (Fig. 78), converged after approximately 2000 iterations, while the other simulation ran for the full 2500 iterations (Fig. 79) and still failed to improve its convergence. Most of our simulations were run for 1500 iterations, and depending on the number of mesh elements, each simulation could take from two to three hours to execute. In the cases where the iteration count was increased to 2500, these simulations took approximately five hours or longer to complete. Due to time constraints, we were unable to extend the duration of each simulation up to 2500 iterations to achieve an optimal convergence. Therefore, the team decided to average the peaks of the oscillations and use this as the solution. Through comparing the average of the peaks of the 2500 iteration simulation and the convergence seen in this case, Fig. 78, the team confirmed that averaging the peaks was a valid method of determining the thrust results of each simulation.

The Kaman K16-B was designed to test V/STOL technology in planes, therefore assuming the plane were to takeoff vertically, the two rotoprops would need to produce more thrust than the plane's weight. From the documents of the original work with this plane, to overcome the estimated maximum gross weight of 12,000 lbf, a thrust value from the rotoprops required was 12960 lbf, or 57648 N due to the turning efficiency of 0.92 from a max flap deflection of 50 degrees [10]. According to this, each rotoprop must be able to supply 28824 N of thrust to remain at a stationary hover, any more thrust and the plane would be able to accelerate vertically. This is an overestimation of the thrust required, as the engines would only tilt up to 60° and the thrust would not be entirely vertical. Guided by these assumptions, we formulated expectations regarding the anticipated results. The team also presumed that increasing the collective flap deflection would increase the thrust of the rotoprop due to an increase in camber; however, this assumption did not prove accurate in our simulations. The results of the single-blade Fluent simulations are listed in Table 8. The values in this table also approximate the total thrust capabilities of one rotoprop by multiplying the single blade results by a factor of three.

Single-Blade Thrust Results (N)					Full Rotoprop Thrust Results (N)				
		Collective Flap Angle (deg)					Collective Flap Angle (deg)		
		0	7	13			0	7	13
Blade Pitch Angle (deg)	15	7173	-----	6100	Blade Pitch Angle (deg)	15	21519	-----	18300
	30	11550	11000	10900		30	34650	33000	32700
	45	14254	-----	13543		45	42762	-----	40629

Table 8: Results of the Single-Blade Thrust with Approximation of Full Rotoprop Thrust

The results in Table 8 show that the K16-B could have produced enough thrust to takeoff vertically with the blade pitch set at 30 and 45 degrees, regardless of the collective flap angle. Interestingly, the results show that the thrust decreases with collective flap angles of 7 and 13 degrees. This decrease in thrust is most likely due to flow separation from the high camber towards the blade tip created with collective flap deflections. In the original documentation of work on the K16-B, the engineers found that the collective flap was not as useful as they thought [10]. Initially the engineers set the maximum collective flap angle to 15 degrees but found this was even worse for the thrust and decreased the maximum angle to 13 degrees. Despite this adjustment and according to our results, the collective flap may only be useful in increasing the thrust from 0 to 7 degrees. With more time to conduct simulations, the CFD subteam would have been able to determine the optimal collective flap angle to maximize the thrust.

The impact of the blade pitch on thrust aligned precisely with our initial expectations. As the blade pitch angle increased, so did the thrust generated by the rotoprop. The blade pitch angle of 15 degrees represented the minimum setting found in the original engineering reports [10], making it improbable to generate sufficient thrust for lifting the plane. This setting was more likely intended for use in cruise conditions.

We were unable to make any speculations about the plane’s ability to takeoff vertically or over a short distance from these results alone. However, the thrust the rotoprops can produce would give the plane a great chance of taking off. While the results only represent the highest rpm the engine was tested at in the wind tunnel, they show that the plane could have been used as intended.

While the collective flaps were ineffective at increasing the thrust of the rotoprops, the flaps could have been used to help the engine run more efficiently. To analyze the effects on the

engine when deflecting the collective flap, the moment of the blade was calculated about the center of rotation. The results of these calculations are presented below in Table 9. The moment of the full rotoprop (i.e. the torque needed to overcome aerodynamic loads to rotate at the specified rpm) was also approximated using the same method as when evaluating the thrust results.

Single Blade Moment Results (N-m)					Full Rotoprop Moment Results (N-m)				
		Collective Flap Angle (deg)					Collective Flap Angle (deg)		
Blade		0	7	13	Blade		0	7	13
Pitch	15	-2178.5	-----	-3171.1	Pitch	15	-6535.5	-----	-9513.3
Angle	30	-6099.2	-6370.5	-9418.4	Angle	30	-18297.6	-19111.5	-28255.2
(deg)	45	-12569.8	-----	-14097.8	(deg)	45	-37709.4	-----	-42293.4

Table 9: Moment on the Blade about the Center of Rotation

The moments in Table 9 were calculated from the center of rotation about the axis of rotation. The results are all negative because the blade had a negative rotation relative to Fluent’s coordinate system. As the collective flap angle increases, the moment also increases, therefore the engine would have had to produce more torque to rotate the rotoprop with collective flap deflection. The power required to rotate each rotoprop was calculated by multiplying the moments for a full rotoprop shown in Table 9 and the rotational speed of the rotoprop. Based on the moment data in Table 9, the engine would have to produce from 665 hp to 4308 hp to rotate one rotoprop. The K-16B was created to use two YT58-GE-2A engines each producing 1325 hp. The required power to maintain the rotational speed of the rotoprops is higher than the maximum power output from the each YT58 engine, therefore the rotoprops require a higher power output at the higher moment rotoprop settings.

The addition of a collective flap on the propeller blade was a unique design choice and had not been done before. The flap may have been more effective at lower angles that we did not have the time to test, however it was shown to be ineffective at increasing the thrust and increasing the engine efficiency. Increases in collective flap deflection increased the torque required to turn the blade for the parameter space the team tested. In the original engineering report, they said that they needed to use the collective flaps much less than they anticipated [10]. The collective flap may have been a useful tool for increasing the thrust of the rotoprop at angles between zero- and 7-

degree deflection, however the team was unable to test this.

Fluent calculates all the parameters for the fluid dynamics of a simulation. The calculated pressures on the blade surface were exported from the CFD analysis to the structural analysis to evaluate the stresses through the rotoprop blades. The dynamic pressure contours at different blade pitch angles and collective flap deflections are presented in Figs. 80 - 82. The distributions seen below are representative of the distributions observed in the other cases, therefore the three cases displayed have similar pressure distributions over the rotoprop blades. For all three figures showing the pressure contours, the left image shows the top of the blade, and the right image is the bottom of the blade.

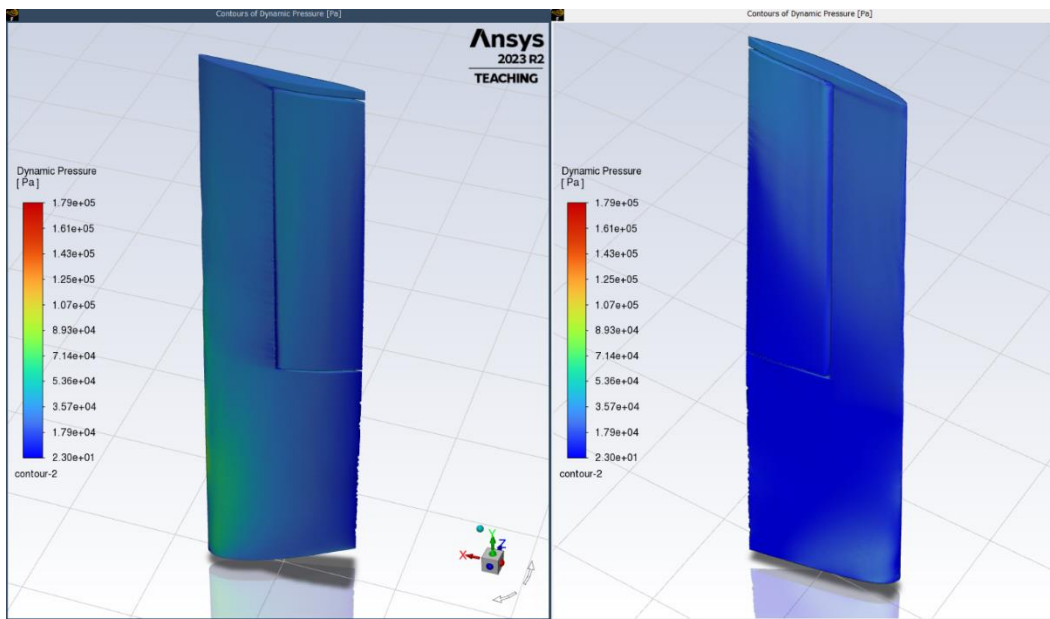


Figure 80: Pressure Contours of the Blade at the 15° Pitch and 0° Flap Angles

Figures 80 – 82 present the dynamic pressure distribution over a single rotoprop blade with different combinations of pitch and collective flap angles. As can be seen in Fig. 80, corresponding to a 15° pitch and 0° collective flap angle, the pressure is higher on the top surface and lower on the bottom surface, which shows that the blade was operating correctly and producing a positive thrust. With the flap set to no deflection, the pressure across the blade faces is relatively constant. This orientation of the blade was a relatively streamlined design, therefore the simple pressure distributions reflect this fact.

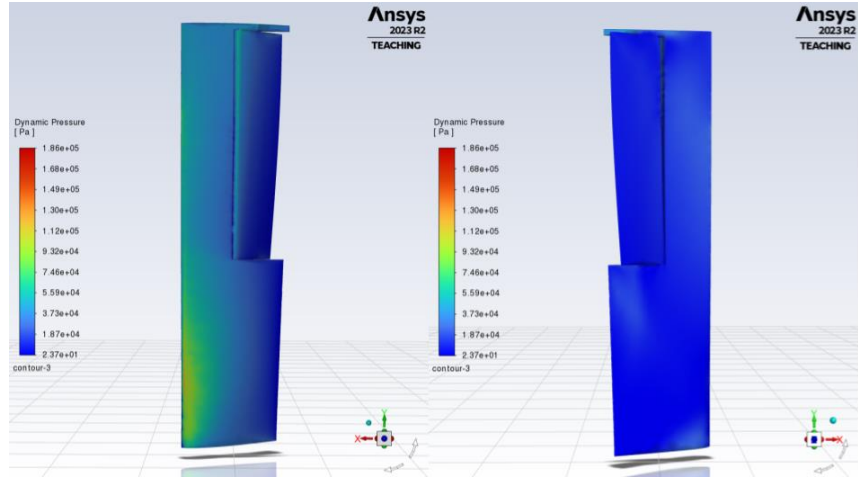


Figure 81: Pressure Contour of the Blade at 30° Pitch and 13° Flap Angles

Figure 81 presents the pressure distribution over the rotprop blade with a 30° pitch angle and full collective flap deflection. Between the higher angle of attack and the full deflection of the flap there are regions of higher pressure as compared to the 15° pitch contours. These regions could suggest more turbulent air flow which coincides with our earlier supposition that flow separation starts to decrease the thrust produced by the rotprop.

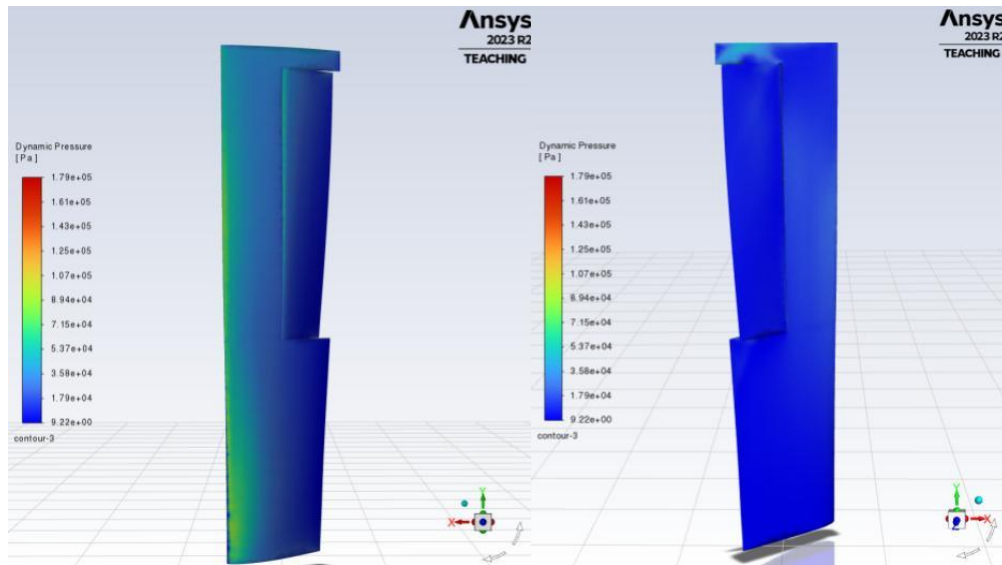


Figure 82: Pressure Contour of the Blade at 45° Pitch and 13° Flap Angles

Finally, Figure 82 presents the pressure contours on the 45° pitch angle with full flap deflection. When compared to the 30° pitch contours, this blade has regions of even higher pressure

than the last. Most of the high-pressure regions are on the blades' leading edge, which is normal for typical propellers. With the flap fully deflected, the gap between the blade and flap also has regions of high pressure, however this can be expected for flaps with a gap between the flap and the rest of the blade.

6 Methodology for the Structural Analysis

The team chose to implement Ansys Static to run a structural analysis of the K16-B rotoprop blade under typical operating conditions. Completing a structural analysis of the rotoprop blade allowed the team to understand the stress load that the blade would undergo during takeoff, along with the amount of force the actuator needs to apply to produce the desired collective flap deflection.

6.1 Practice with Ansys Static and Sample Model

While the CAD subteam was creating a model of the rotoprop, a sample model of a single rotoprop blade was used to practice and refine the process of structural analysis using Ansys Static. Unlike the original, full rotoprop model considered for the Ansys Fluent analysis, the team knew from the beginning that only one rotoprop blade was necessary to model in Ansys Static rather than all three blades. This was due to the assumption that the performance of the rotoprops was being analyzed rather than the operation of the cyclic or the collective control systems, allowing the structural subteam to focus on the blade individually instead of a three-blade system.

To better inform the team on how to accurately model this rotoprop blade so that the resulting stress distribution will be representative of the Kaman K-16B rotoprops during takeoff, the first step the team took was to research this type of analysis. The various steps and considerations taken to structurally analyze a helicopter propeller blade in Ansys Static were depicted by various online tutorials [19]. The team found several of these tutorials in both Ansys Static and Ansys Fluent to inform the team on how to best represent the propeller system in this simulation.

After learning from these tutorials, the next step was to mesh the sample rotoprop model. The already-set mesh settings were successful to mesh both the blade and the flap. The mesh used is shown in Fig. 83.

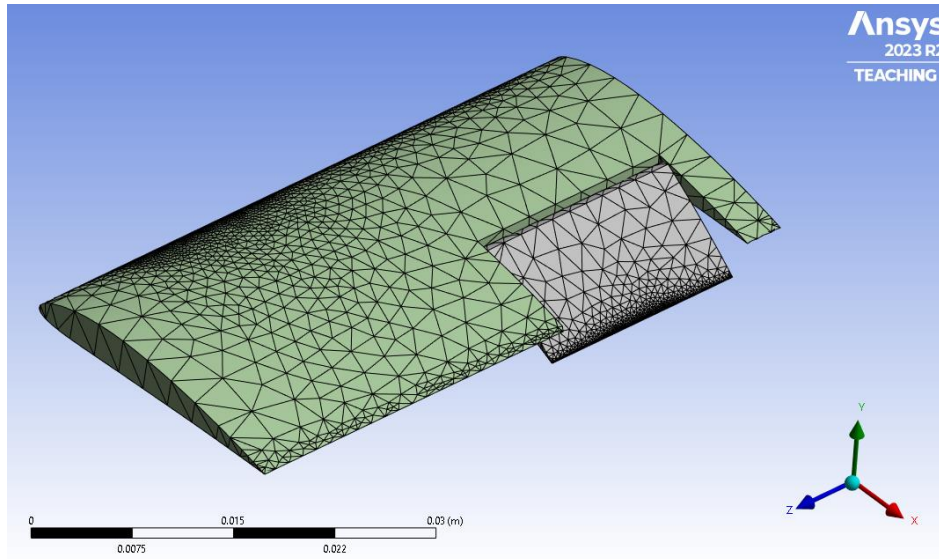


Figure 83: Mesh used for sample model in practice static analysis.

Once the best mesh for the sample model was chosen, the next step was to apply to proper loads and boundary conditions. The first load that must be considered is the pressure distribution due to the airflow over the blade. This pressure distribution is one of the outputs from the CFD analysis carried out in Ansys Fluent. This load will be applied directly to the actual rotoprop blade model by running both Ansys Fluent and Ansys Static in the same Ansys Workbench file; however, since the team was practicing with the sample model while working on completing the actual model, there was no pressure distribution yet obtained from the CFD analysis. So, a uniform pressure load of an estimated value of 10^7 Pascals was applied over the entire surface of the blade.



Figure 84: Uniform pressure load applied to sample model in practice static analysis.

Another load to consider is the induced rotational stresses on the rotoprop blade structure. This load is applied to the blade using the rotational velocity load. As described in Section 2.3.2, this rotational load results in centrifugal stresses that can become significant when rotating at high RPM. To test this and ensuring the deformation due to rotational movement was being evaluated correctly, the team used a simpler model with just one part to eliminate errors with contact regions and plotted the deformation with an extremely high rotational velocity applied to ensure that the model would deform. The center of rotation for this basic test was at the fixed face of the mode; for the actual simulation, the center of rotation will be applied at a certain distance from this face to represent the center of the hub about which the blade rotates. Note that this simpler model was used only to test the deformation that results from the rotational velocity load; for the rest of the practice analysis process, the sample blade model with the flap was used.

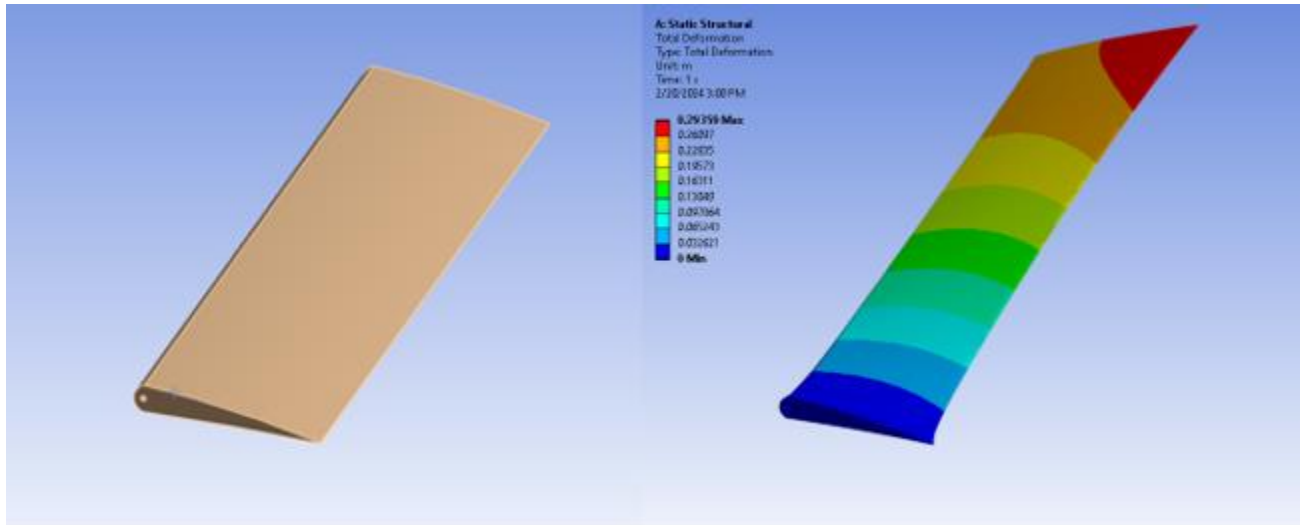


Figure 85: Single-part model of flap used to test deformation in Ansys Static.

Once this was confirmed, we moved back to the sample blade model with the flap and a rotational velocity was applied at an estimated distance away from the fixed end of this model since the blade rotates about the hub. A value of 75.9 radians per second, corresponding to about 725 rpm, was used, since this was about the same rotational velocity reported in one of the original K-16B report documents [10].

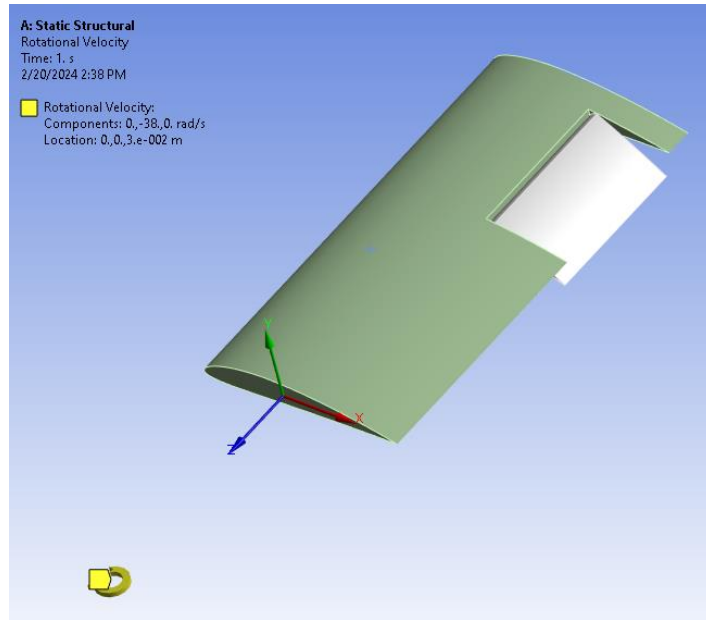


Figure 86: Rotational velocity load applied to sample blade model in practice static analysis.

The last step to simulate takeoff with the sample blade model is to apply a point on the model where it is constrained so that the model remains in place. For the sample blade model, we applied a fixed support to the entire face of the blade root where it would join with the rotoprops hub, which is where we planned to apply it on the actual model as well. This ensures that the applied loads best simulate how the blade is constrained on the K-16B.

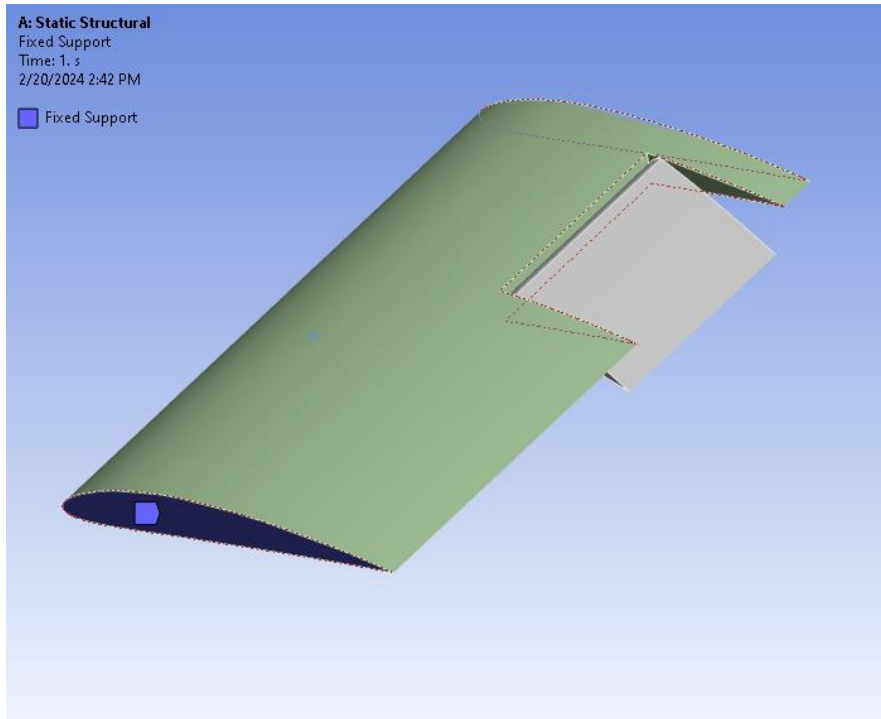


Figure 87: Fixed support applied to sample model during practice static analysis.

The sample model shown in Fig. 87 (with a flap) included only the load due to rotational motion at 725 rpm and was solved. The results are shown in Fig. 88 and display the equivalent, or von Mises, stress.

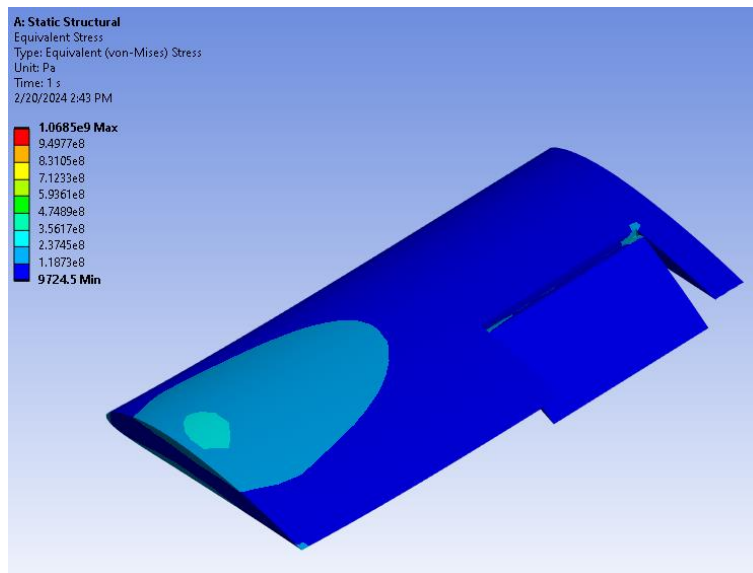


Figure 88: Von Mises stress plot for practice static analysis.

Using the sample simplified blade model, along with the test model to test the resultant deformation from the rotational velocity, the team was able to successfully go through the process of simulating the stress load that the blades would have to bear during takeoff conditions, which helped the team prepare for the final model of the blade.

6.2 Material Assignment

Because Ansys Static performs a structural analysis, the material of the part that a model represents is incredibly important; a material's properties such as tensile strength, compressive strength, fatigue life, toughness, and elasticity heavily influence and ultimately determine the stress load that a material can bear before failure. So, we had to apply the correct material properties to the model in Ansys Static before the model could be run.

To determine the exact materials used for the K-16B, the team turned to original blueprints provided by NEAM [15]. The "Blade Assy. (Rotor)" blueprint [NA1] provided the materials used for the blades. While this blueprint goes into much detail about the specific material used for each individual part, the team decided to reduce the number of materials used due to the project time constraints and to minimize the complexity of the CAD blade model. The blueprint revealed that a significant portion of the blade was made of various types of wood, with spruce being the most common; much of the wood is not visible from the outside due to an aluminum coating of the blade [NA1]. The blade also contains a spar that is made of laminated birch plywood.

Originally, based on the knowledge gained from this blueprint, the team planned to use spruce and birch plywood as the two materials applied to the model in the static analysis. However, the model was separated into three parts: the blade, the collective flap, and the rod that anchors the flap to the blade. Ansys Static is designed so that material assignment is specified for each part; however, the actual distribution of different materials in the blade is different than the separation of parts for this model. The spar is birch plywood surrounded by spruce [NA1], but since the blade itself is only one part, we could only assign one material each to the blade, flap, and rod. So, the team decided to run the blade and flap simulation assuming only spruce construction, since using

multiple material properties (as in, assigning either the blade or the flap birch plywood) would not have captured the combination of materials used in the actual blade and would only have made the model more complex. Further, the team chose spruce because it is the heavier of the two materials, and this would be the more conservative option considering the centrifugal force of the rotating blade.

To assign the material properties of spruce to the appropriate parts of the model, we used Table 14.4 in *Aircraft Dynamics* [27] to define the tensile and compressive ultimate and yield strengths, along with Young’s modulus. Poisson’s ratio for spruce was determined by research to be 0.4 [13]. Since spruce was not in the material library in Ansys Static, the team added wood to the model and changed the material properties to apply spruce to the model (see Figs 89 and 90).

The figure consists of two screenshots from the Ansys Static software interface. The top screenshot shows the 'Outline of Schematic A2: Engineering Data' window. It features a table with columns A, B, C, D, and E. Row 3 is 'Structural Steel' and row 4 is 'Wood'. Row 4 is highlighted with a dashed border. The bottom screenshot shows the 'Properties of Outline Row 4: Wood' window, which is a detailed table of material properties for the 'Wood' material.

	A	B	C	D	E
1	Contents of Engineering Data		Source		Description
2	Material				
3	Structural Steel				Fatigue Data at zero mean stress comes from 1998 ASME BPV Code, Section 8, Div 2, Table 5 -110.1
4	Wood				
*	Click here to add a new material				

	A	B	C	D	E
1	Property	Value	Unit		
2	Material Field Variables	Table			
3	Density	442.88	kg m ⁻³		
4	Isotropic Elasticity				
10	Tensile Yield Strength	4.2747E+07	Pa		
11	Compressive Yield Strength	2.7579E+07	Pa		
12	Tensile Ultimate Strength	6.4811E+07	Pa		
13	Compressive Ultimate Strength	3.4474E+07	Pa		

Figure 89: Material properties of spruce inputted into Ansys Static engineering data.

Table of Properties Row 4: Isotropic Elasticity					
	A	B	C	D	E
1	Temperature (C) 	Young's Modulus (Pa) 	Poisson's Ratio	Bulk Modulus (Pa) 	Shear Modulus (Pa) 
2	23	8.9632E+09	0.4	1.4939E+10	3.2011E+09

Figure 90: Elastic properties of spruce added to Ansys Static engineering data.

6.3 Meshing: Issues and Final Mesh

The team evaluated several different blade CAD models while attempting to generate the mesh in both Ansys Fluent and Ansys Static. Some models could not be meshed in either simulation, which prompted a return to SolidWorks by the CAD subteam to work out any contact surface issues or other problems that could be causing a meshing failure.

One of the final models the team attempted to mesh and run in Fluent and Static was a model of a single blade with the flap and rod along with the linkage part that attached the top of the flap surface to the top of the blade surface. While this would not mesh in Fluent, the meshing in Static was successful, as shown in Fig. 91.

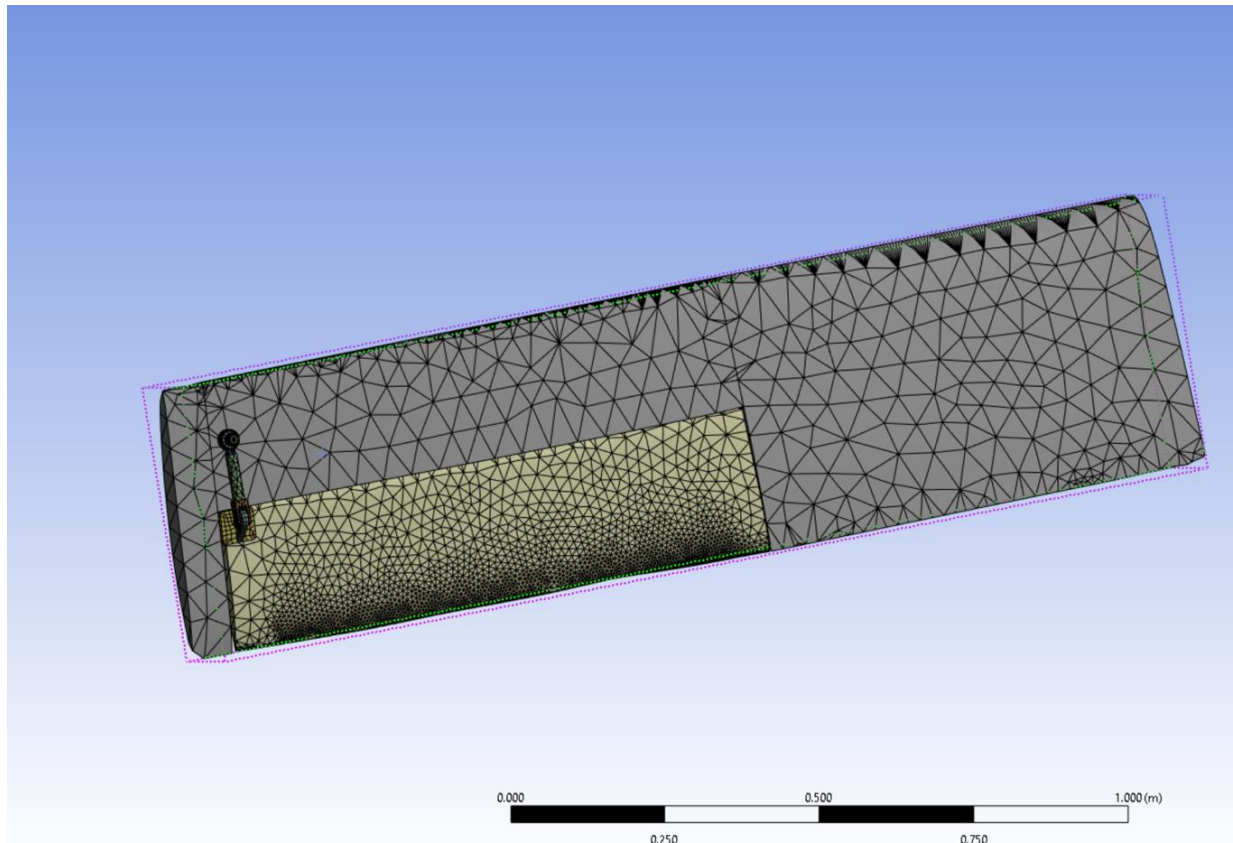


Figure 91: Meshed model of single blade including linkage in Ansys Static.

After some discussion, the team decided that the model including the linkage would not be used for the structural analysis due to unsuccessful attempts to mesh the model in Fluent. Instead, the simpler model of the blade with the flap and rod but with no linkage, was used for the structural analysis to preserve consistency between the CFD analysis and the structural analysis. So, the same model was used for all the parameter cases, but with the flap deflected to zero, seven, and thirteen degrees for the respective parameter cases.

6.4 Applied Loads

The team went through the same process to simulate the takeoff conditions for the blade as was done for the practice model. To model the blade's attachment to the hub, a fixed support was added to the face of the blade where the attachment would take place, as shown in Fig

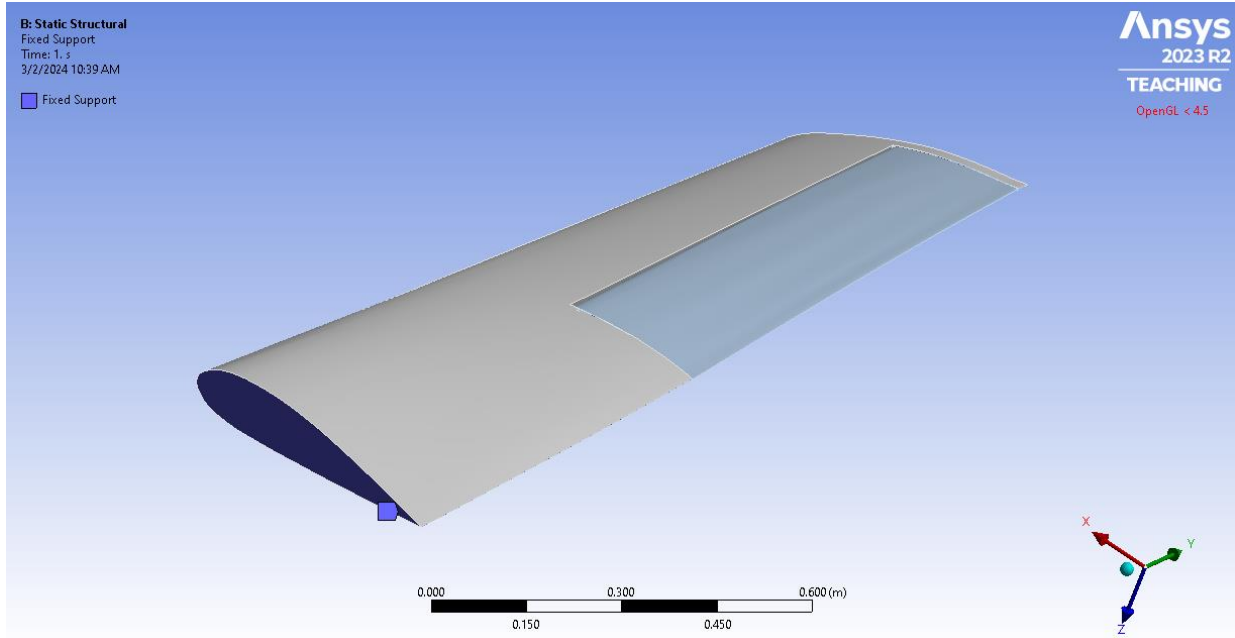


Figure 92: Fixed support load applied to proper blade face on the 0-degree flap deflection model in Ansys Static.

The team then imported the static pressure distribution load directly from Ansys Fluent by running Ansys Static in the same workspace. The team used the static pressure distribution because the structural analysis to be performed was a static structural analysis, meaning that there would be no variation of the loads with time. The team was carrying out this analysis with the goal of applying constant loads to the blade that would simulate the constant loads the blades would experience during takeoff, so a static pressure distribution was appropriate. The imported pressure distribution for the 15° pitch angle and the 0° flap deflection parameter case is shown in Fig. 93.

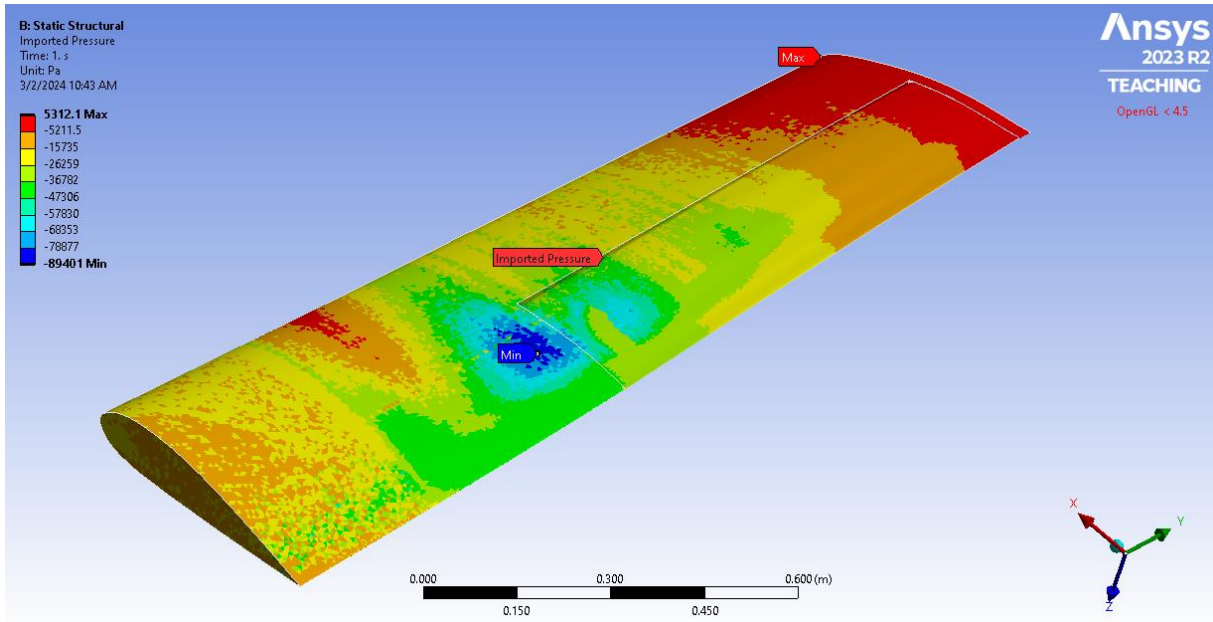


Figure 93: Imported static pressure distribution from Fluent in Static for 15° pitch angle and 0° flap angle parameter case.

The next load that was applied was the centrifugal load that results from the rotational velocity. Research into original documentation [7] showed that the intended rotational velocity of the blades was about 75.9 radians per second, corresponding to about 725 rpm. So, this rotational velocity was applied to the blade, with the center of rotation being the distance from the fixed face to the center of the hub (0.313 meters). This rotational velocity is indicated by the yellow arrow in Figure 94.

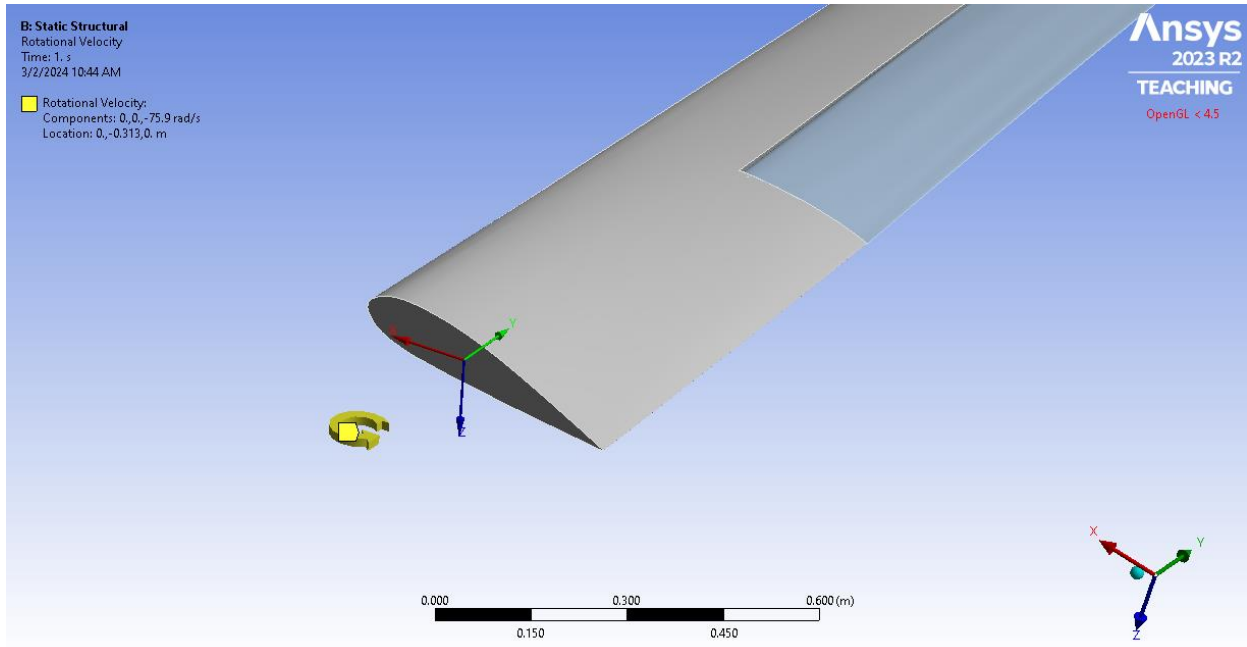


Figure 94: Rotational velocity of 75.9 radians per second applied 0.313 meters from fixed face of blade.

These rotational loads were applied to each model for all parameter cases along with the static pressure distributions and then run in Ansys Static to provide structural analysis results.

6.5 Stress Results and Discussion

We ran seven different parameter cases for the structural analysis. The parameter cases are defined in Table 10.

Parameter Case Number	Pitch Angle	Flap Angle
1	15°	0°
2	15°	13°
3	30°	0°

4	30°	7°
5	30°	13°
6	45°	0°
7	45°	13°

Table 10: Definitions of the parameter cases run for structural analysis.

This section displays three different figures of the structural analysis results for each case. Each case displays first the von Mises stress plot for the top of the blade without the flap; this first plot is followed by the side-by-side von Mises stress plots for the top and bottom of the blade with the flap. For the first figure of the stress distribution without the flap in each case, it is noted that the flap was included in the simulation, but it is suppressed in the figure to display the induced stresses that would otherwise be hidden, such as those on the rod.

Case 1: 15° pitch angle, 0° flap angle:

The first parameter case run was the 15° pitch angle and 0° flap angle case. The equivalent, or von Mises, stress results are shown with the rod circled in Fig. 95. See Section 2.3.1 for a definition of the von Mises stress.

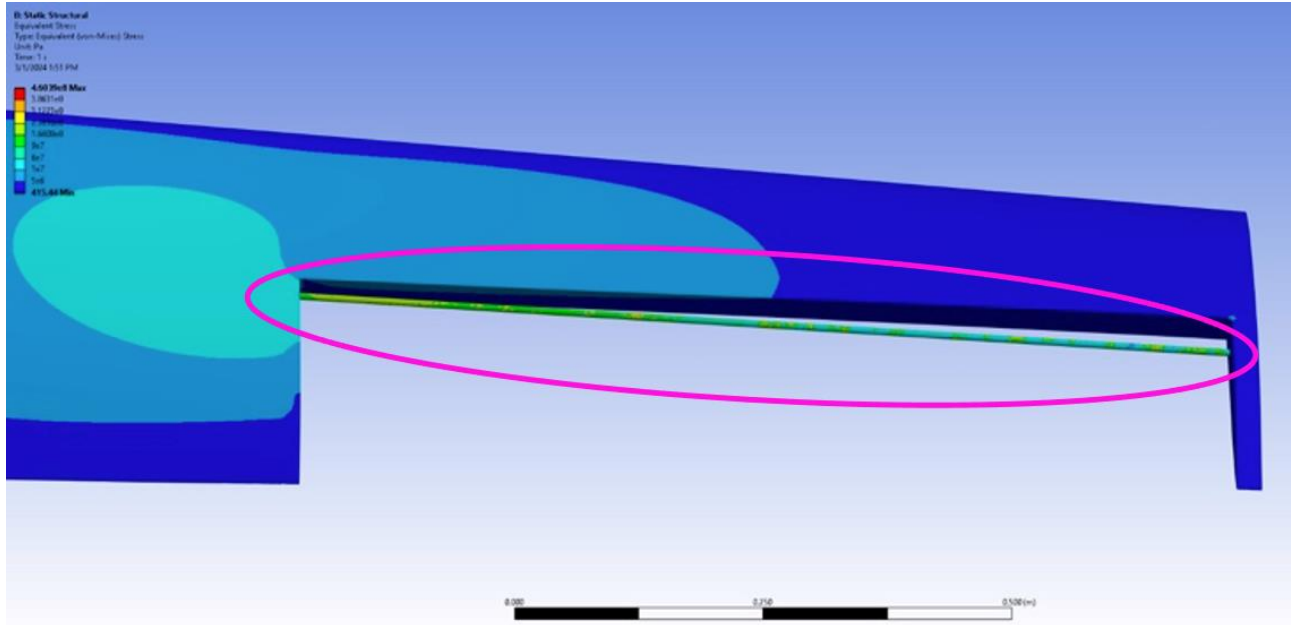


Figure 95: Von Mises stress contour plot without flap shown for 15° pitch angle and 0° flap angle case with a case-unique contour.

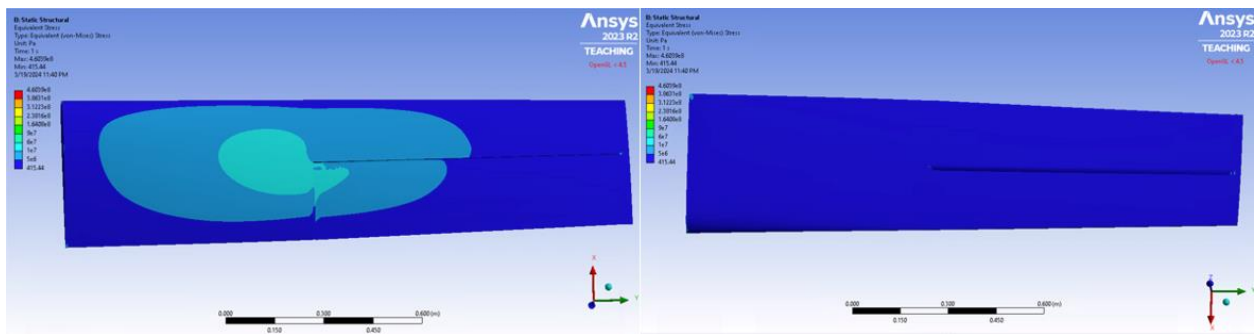


Figure 96: Von Mises stress contour plot of blade with flap (top and bottom surfaces) for 15° pitch angle and 0° flap angle case with a case-unique contour.

For this case, the rod showed the highest stress levels, shown in Figure 95 96, reaching the maximum of about 0.46 gigapascals (GPa). The top surface in Fig. 95 showed an increase in stress from the edges of the blade to where the blade meets the interior edge of the flap, with the maximum on the top of the blade reaching between 10 and 60 megapascals (MPa).

Case 2: 15° pitch angle, 13° flap angle:

The next parameter case run was the 15° pitch angle and 13° flap angle case. The von Mises stress results are shown in Figs 97 and 98.

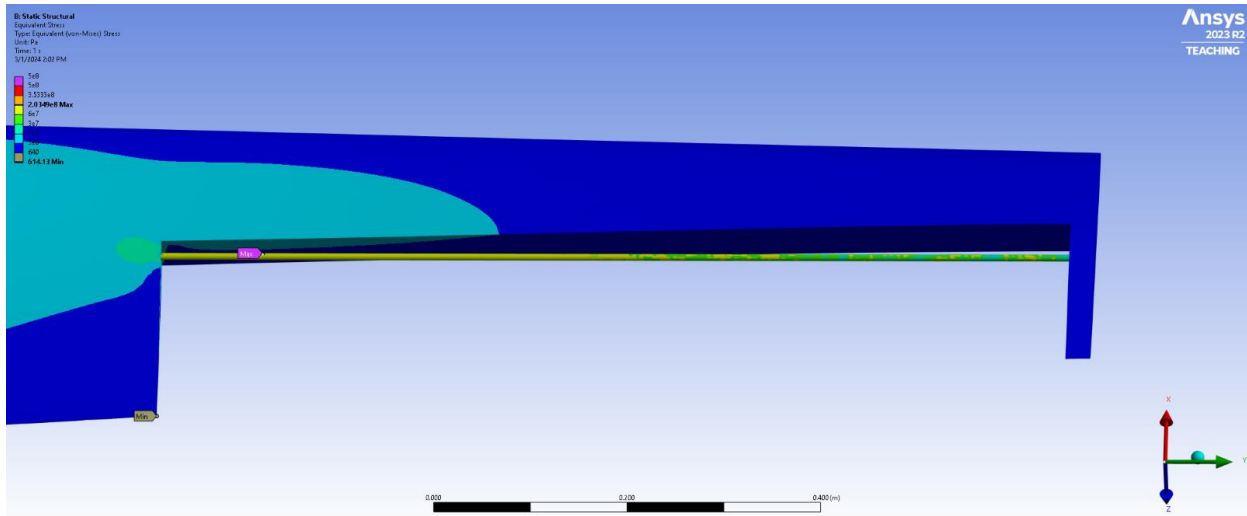


Figure 97: Von Mises stress contour plot focused on rod for 15° pitch angle and 13° flap angle case with a case-unique contour.

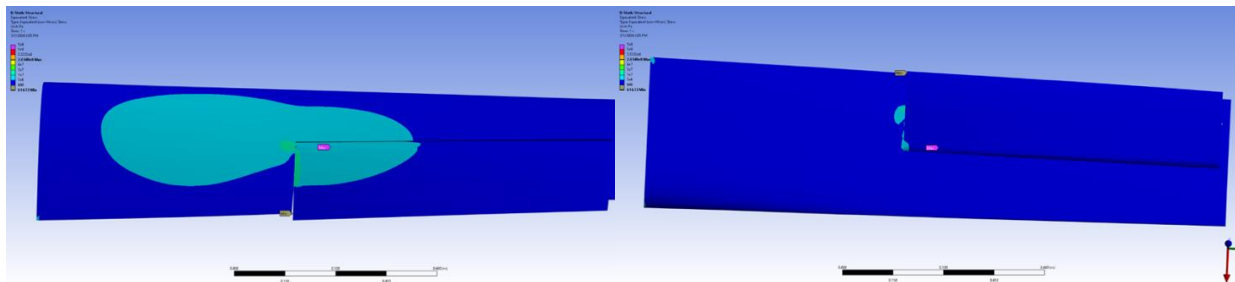


Figure 98: Von Mises stress contour plot of blade (top and bottom surface) for 15° pitch angle and 13° flap angle case with a case-unique contour.

Deflecting the flap thirteen degrees from Case 1, Case 2 showed the highest stress persisting on the rod in Figure 96 at about 350 MPa. The higher stresses on the blade and flap, between 10 and 30 MPa as shown in Fig. 98, continued to be seen increasing as the interior edge of the flap where it diverts from the blade.

Case 3: 30° pitch angle, 0° flap angle:

The third case ran was the 30° pitch angle and 0° flap angle case. The von Mises stress results are shown in Figs 99 and 100.

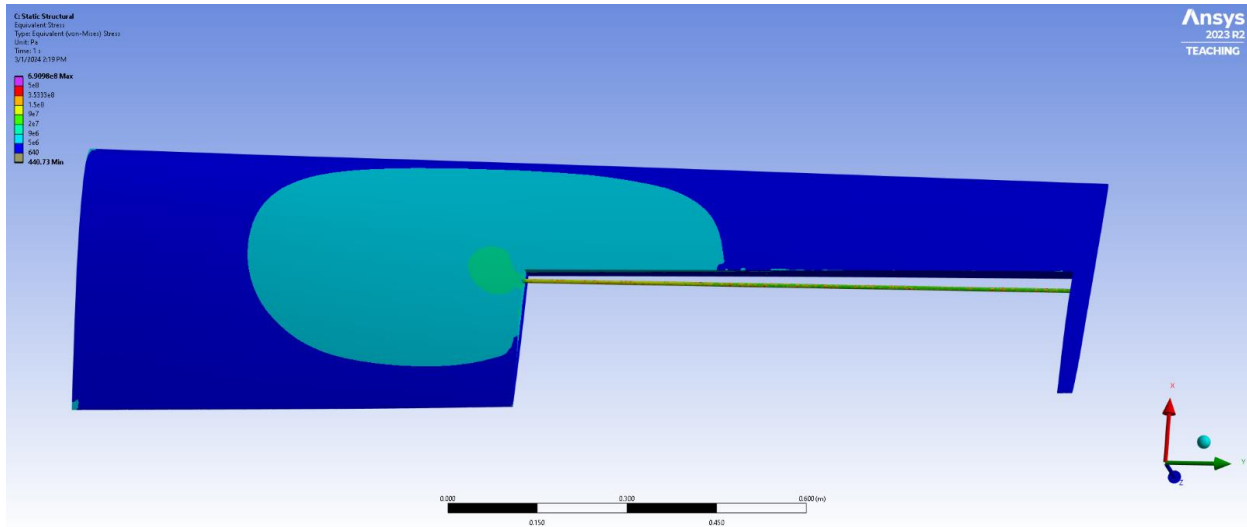


Figure 99: Von Mises stress contour plot focused on rod for 30° pitch angle and 0° flap angle case with a case-unique contour.

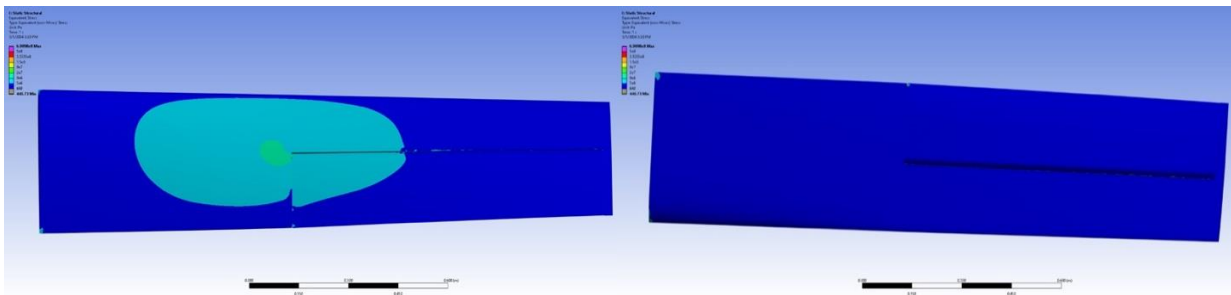


Figure 100: Von Mises stress contour plot of blade (top and bottom surface) with flap for 30° pitch angle and 0° flap angle case with a case-unique contour.

The highest stresses on the rod, shown in Fig. 99, reached between 350 and 500 MPa. The concentration of higher stresses on the top of the blade remained consistent in terms of location where the blade meets the interior edge of the flap; these stresses reached between 9 and 20 MPa, as shown in Fig. 100.

Case 4: 30° pitch angle, 7° flap angle:

The von Mises stress results for this case are shown in Figs 101 and 102.

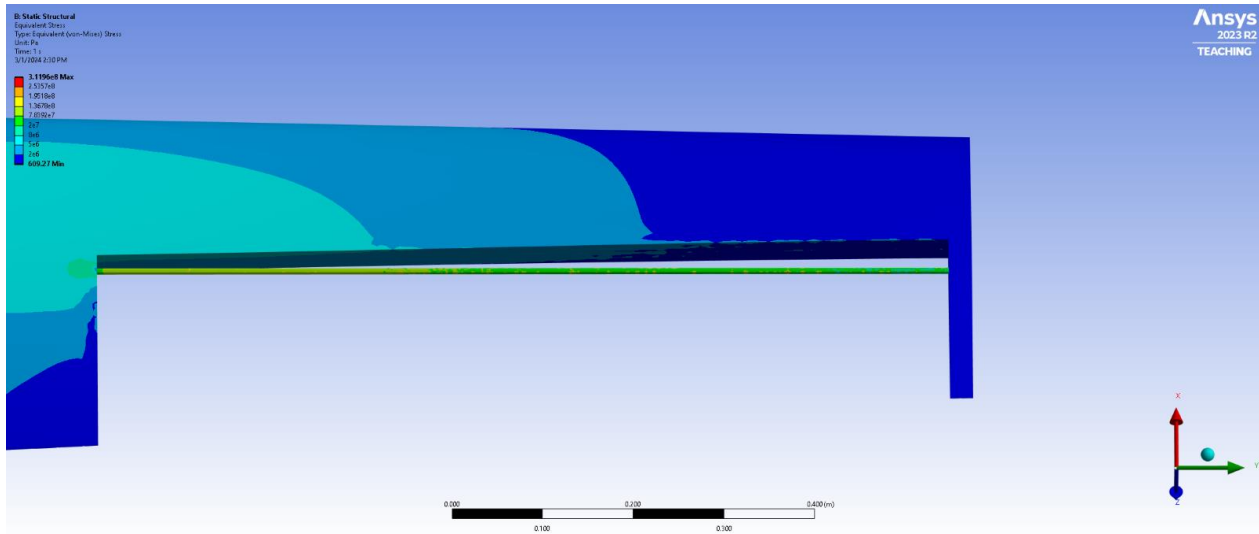


Figure 101: Von Mises stress contour focused on rod for 30° pitch angle and 7° flap angle case with a case-unique contour.

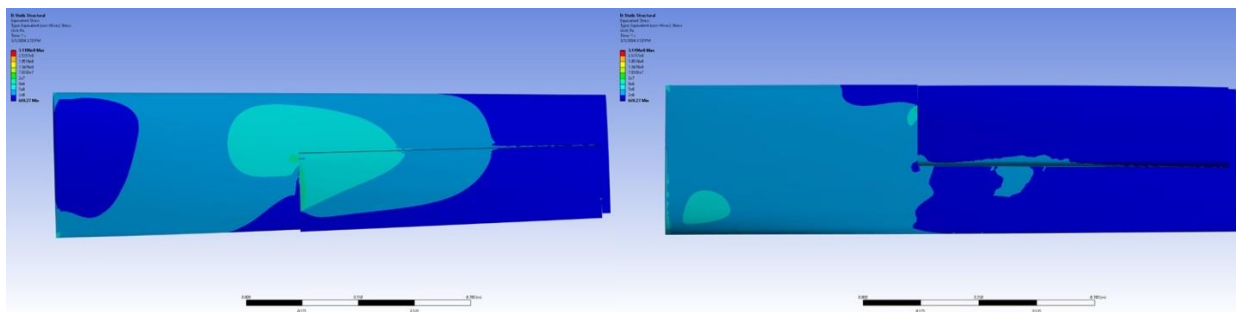


Figure 102: Von Mises stress contour of blade (top and bottom surface) with flap for 30° pitch angle and 7° flap angle case with a case-unique contour.

The highest stresses on the rod generally reached from about 100-200 MPa shown in Fig. 101, and the top surface of the blade showed the highest stresses near the interior edge of the flap reaching up to about 20 MPa shown in Fig. 102. The bottom surface of the blade saw higher stresses than in the previous cases, reaching up to about 5 MPa on the bottom surface in the region closer to the fixed face.

Case 5: 30° pitch angle, 13° flap angle:

The von Mises stress results for the next case with a thirty-degree pitch angle and a thirteen-degree flap angle are shown in Figs 103 and 104.

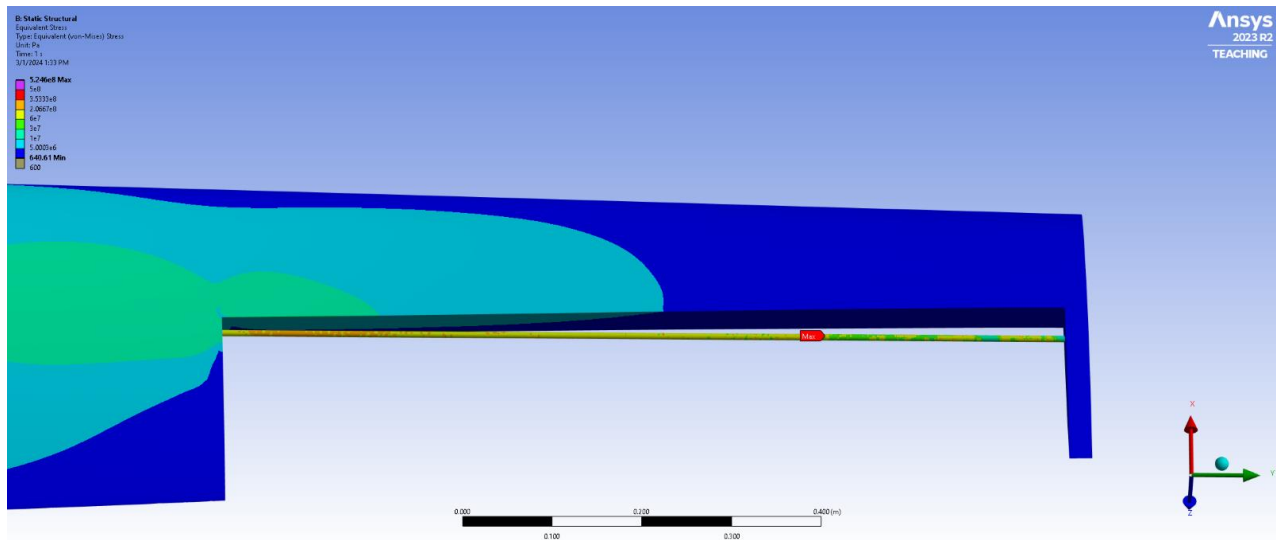


Figure 103: Von Mises stress contour without flap shown for 30° pitch angle and 13° flap angle case.

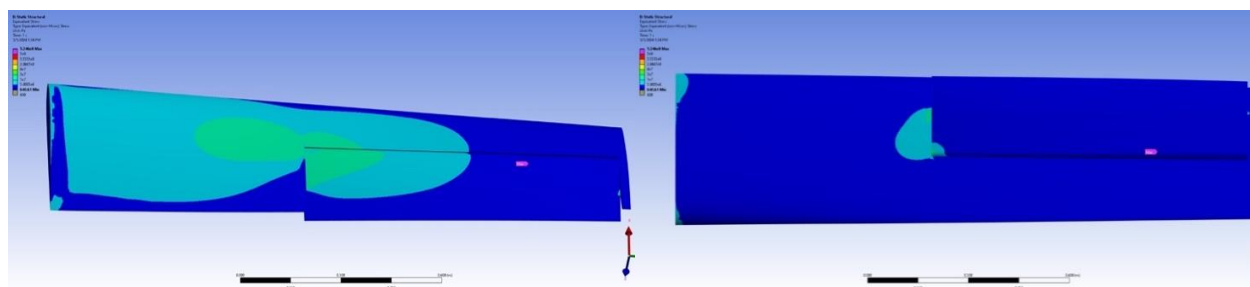


Figure 104: Von Mises contour plot for blade (top and bottom surface) for 30° pitch angle and 13° flap angle case.

The highest stresses occurred on the rod, reaching between 350 and 500 MPa as shown in Fig. 103. The high stresses on the blade remained concentrated near the interior edge of the flap as shown in Fig. 104, but stresses between 10 and 30 MPa were found closer to the root end of the blade surface than in previous cases.

Case 6: 45° pitch angle, 0° flap angle:

The next case increased the pitch angle to forty-five degrees and set a neutral flap angle of zero degrees. The von Mises results for this case are shown in Figs 105 and 106.

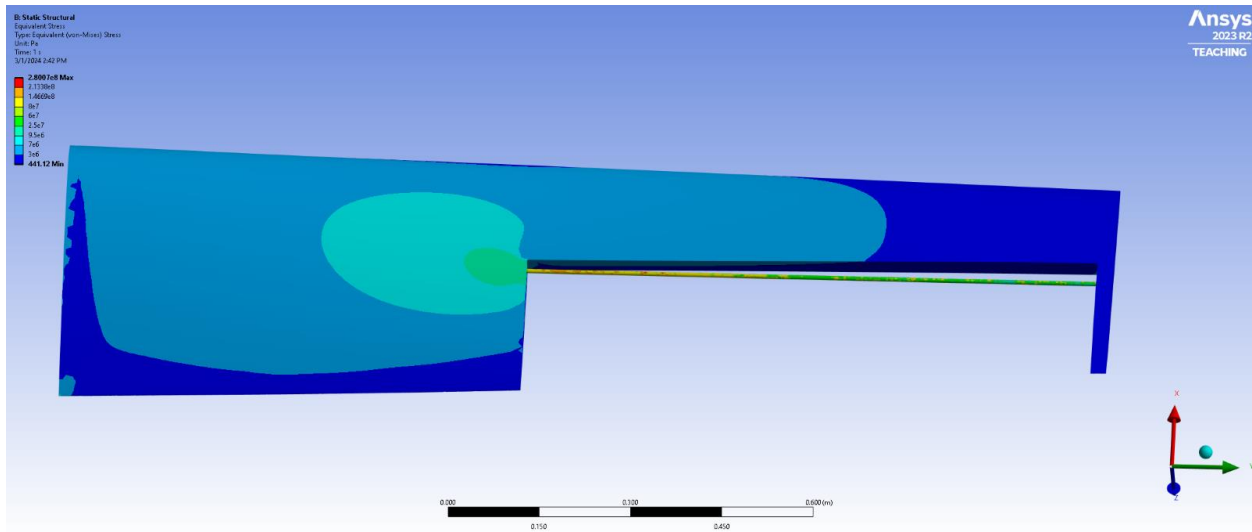


Figure 105: Von Mises stress contour plot without flap shown for 45° pitch angle and 0° flap angle case with case-unique contour.

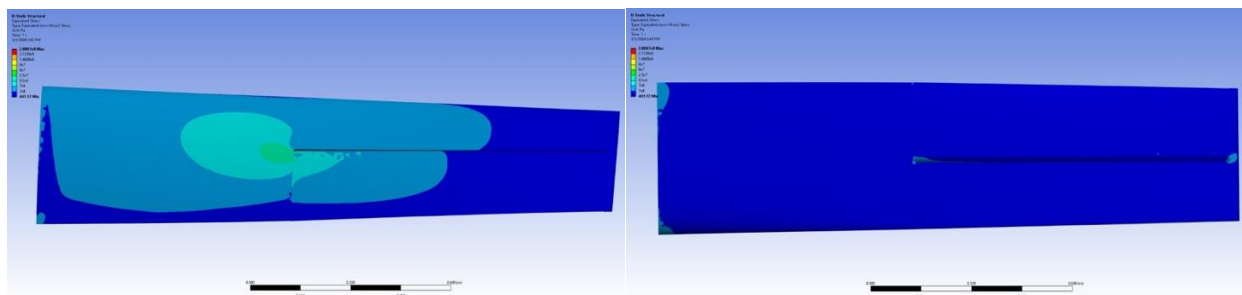


Figure 106: Von Mises stress contour plot of blade (top and bottom surface) for 45° pitch angle and 0° flap angle case with case-unique contour.

The highest stresses once again appeared on the rod in Fig. 105, reaching about 280 MPa. The stresses on the top surface of the blade were highest consistently at the interior edge of the flap at up to 25 MPa, as shown in Fig. 106. The bottom surface remained relatively low stress.

Case 7: 45° pitch angle, 13° flap angle:

The last case that was run was the blade at a forty-five-degree pitch angle and a thirteen-degree flap angle. The von Mises stress results for this case are shown in Figs 107 and 108.

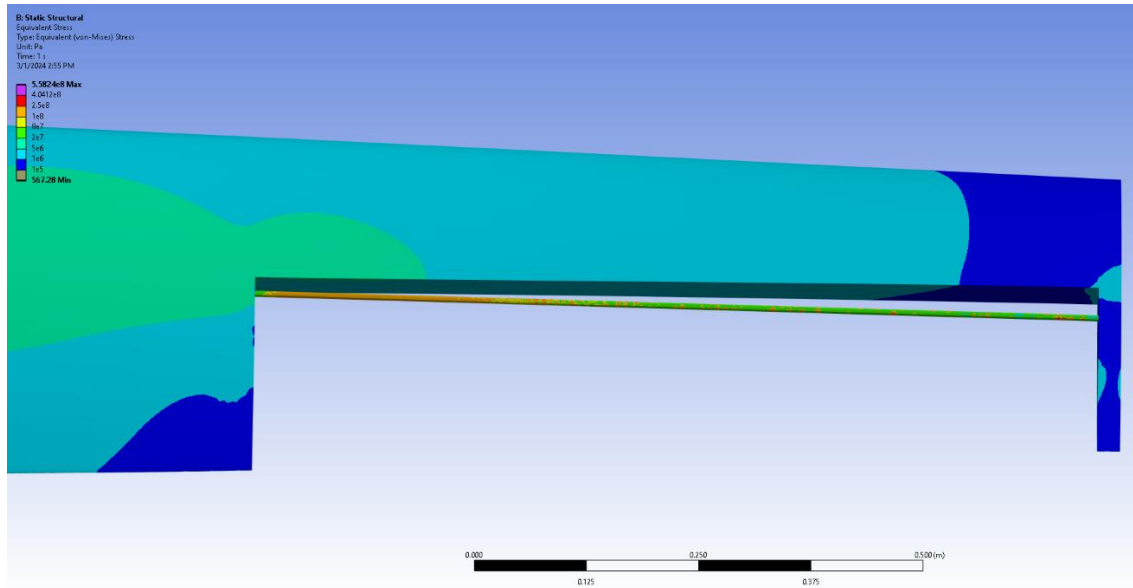


Figure 107: Von Mises stress contour plot without flap shown for 45° pitch angle and 13° flap angle case with case-unique contour.

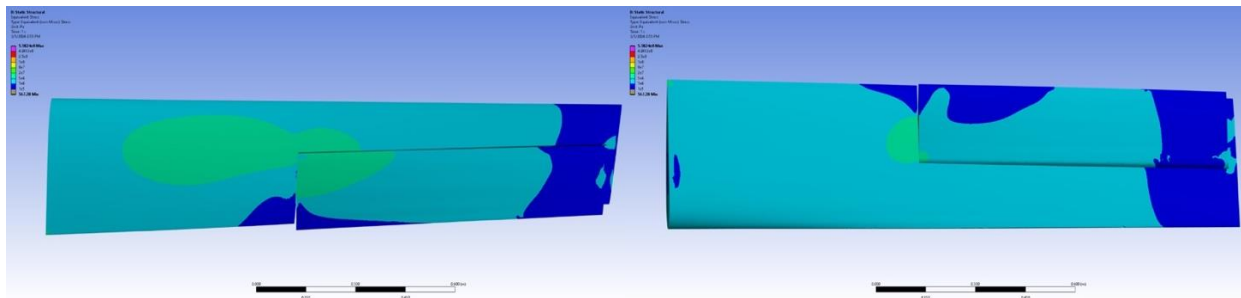


Figure 108: Von Mises stress contour plot of blade (top and bottom surface) for 45° pitch angle and 13° flap angle case with case-unique contour.

The stresses on the rod for this case, shown in Fig. 107, reach about 400 MPa. Fig. 108 shows that the stresses are more distributed on the blade surface than in past cases, with most of the blade surface being between 1 and 20 MPa.

Comparison of von Mises stress results:

In Figs 95 – 108, the colors used in the contours are automatically selected by Ansys to best display the range of values and are only slightly adjusted by the structural subteam. However, the von Mises results for each case can be better compared with a consistent range of contour color/values displayed. The von Mises stress plots for each case with a consistent set of contour

color values are shown in Figs. 109-115.

Case 1: 15° pitch angle, 0° flap angle:

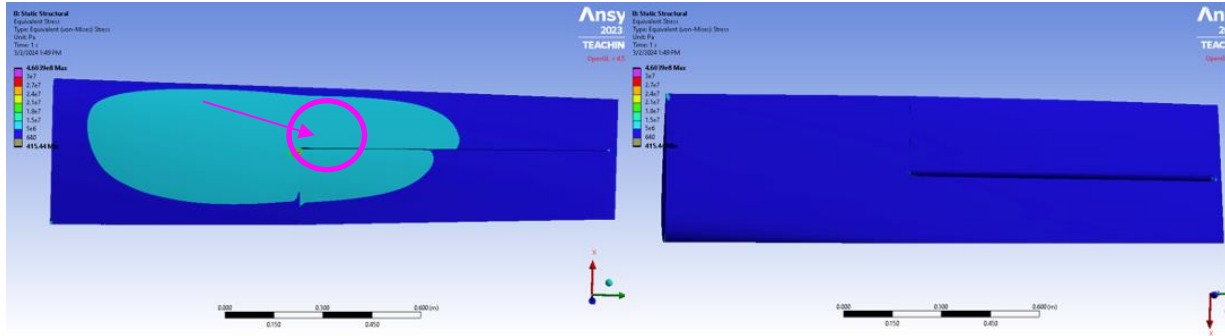


Figure 109: Von Mises stress contour plot of blade top and bottom surface for 15° pitch angle and 0° flap angle case with uniform contour.

Case 2: 15° pitch angle, 13° flap angle:

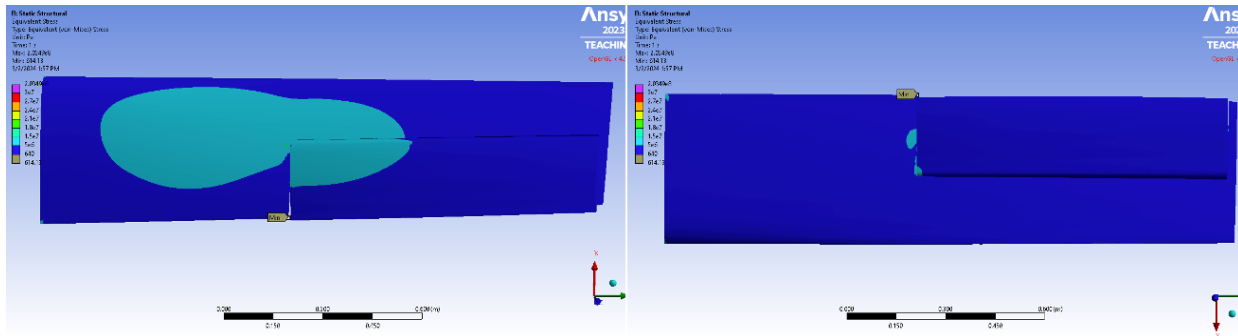


Figure 110: Von Mises stress contour plot of blade top and bottom surface for 15° pitch angle and 13° flap angle case with uniform contour.

Case 3: 30° pitch angle, 0° flap angle:

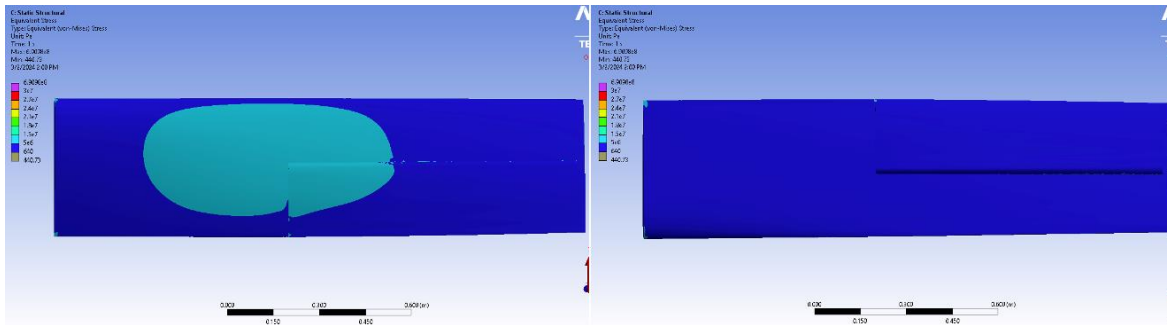


Figure 111: Von Mises stress contour plot of blade top and bottom surfaces for 30° pitch angle and 0° flap angle case with uniform contour.

Case 4: 30° pitch angle, 7° flap angle:

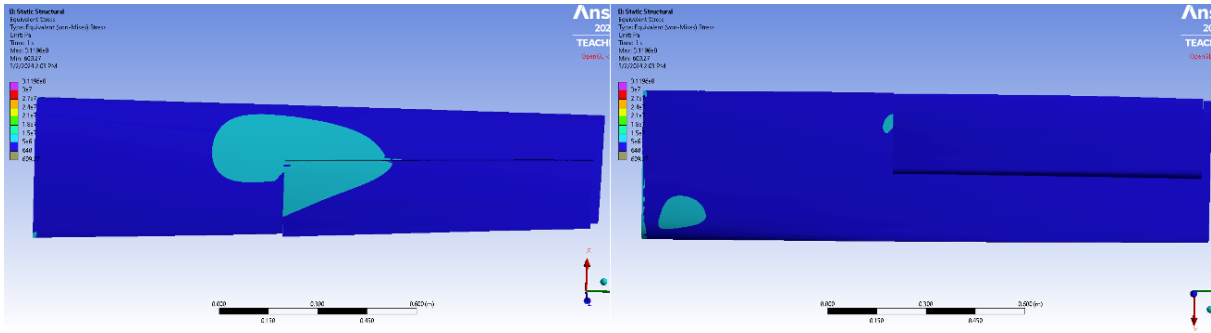


Figure 112: Von Mises stress contour plot of blade top and bottom surfaces for 30° pitch angle and 7° flap angle case with uniform contour.

Case 5: 30° pitch angle, 13° flap angle:

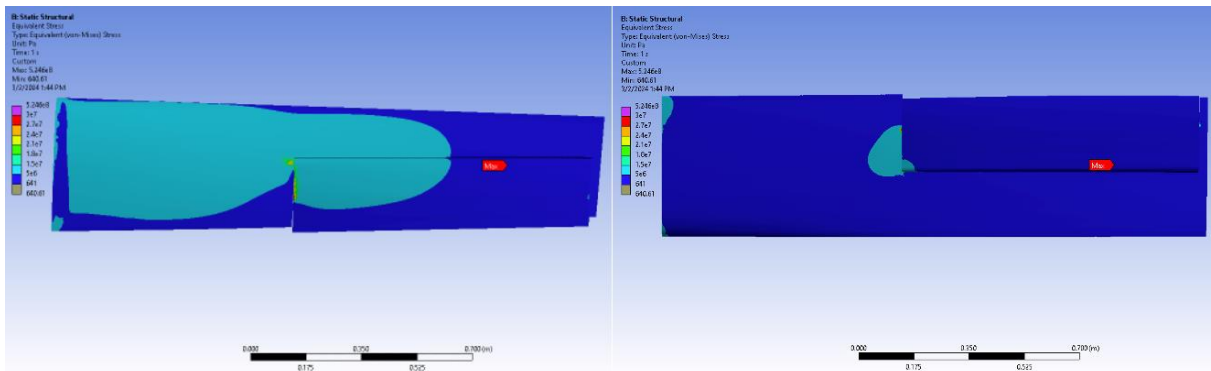


Figure 113: Von Mises stress contour plot of blade top and bottom surfaces for 30° pitch angle and 13° flap angle case with uniform contour.

Case 6: 45° pitch angle, 0° flap angle:

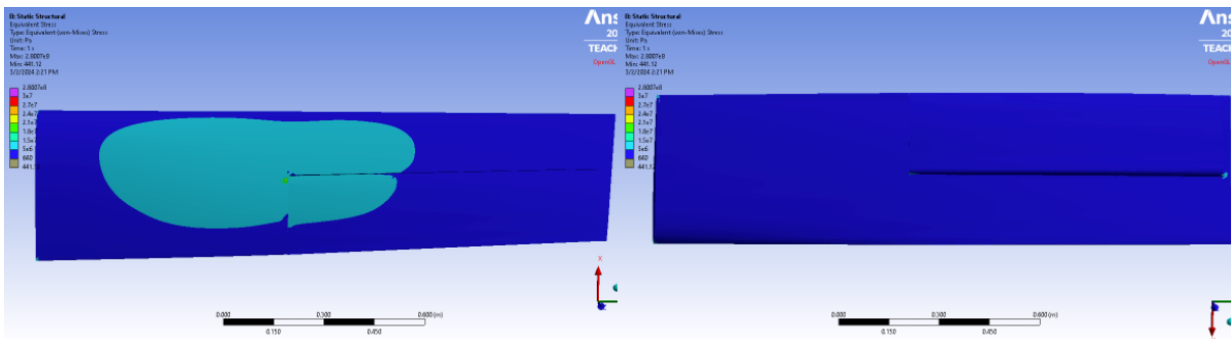


Figure 114: Von Mises stress contour plot of blade top and bottom surfaces for 45° pitch angle and 0° flap angle case with uniform contour.

Case 7: 45° pitch angle, 13° flap angle:

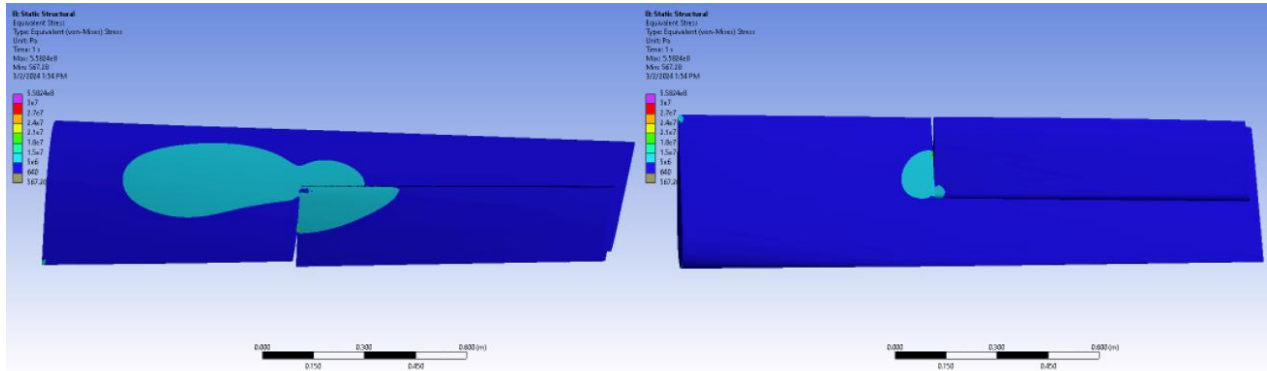


Figure 115: Von Mises stress contour plot of blade top and bottom surfaces for 45° pitch angle and 13° flap angle case with uniform contour.

Based on the results shown above, the effect of pitch angle and collective flap angle on the induced stresses can be analyzed since both were run at multiple angles. The pitch angles run in the seven simulations were fifteen, thirty, and forty-five degrees. The highest stresses on the top of the blade occurred at the fifteen-degree and the thirty-degree pitch angles, and this stress (shown in red) occurred at the corner where the interior edge of the flap and the blade meet; this location is circled in Fig. 109. While the highest stress on the forty-five-degree pitch angle plots occurred near this point, it is not as great a stress. So, based on the range of parameter cases simulated, the forty-five-degree pitch angle caused the lowest stress distribution when examining pitch angle alone. Predicting the stresses for angles outside of the three pitch angles simulated and only considering the effect of pitch angle, a higher pitch angle for the blade is predicted to be generally more conducive to lower stresses based on the results from the seven cases above.

On the bottom surface of the blade, the pitch angle alone did not reveal a certain pattern or behavior in the stress distribution as pitch angle increases. For each flap angle, the behavior of the stress distribution as pitch angle increases or decreases remains relatively constant. So, based on the seven parameter cases run, the stress distribution on the bottom of the blade was not dependent on the pitch angle of the blade.

Considering only the variation due to collective flap angle, three different flap angles were run in the simulations: zero, seven, and thirteen degrees. It is significant to note that the seven-

degree flap angle was only run for the thirty-degree pitch angle, so any conclusions drawn about the seven-degree flap angle will not be as well-informed as those drawn about the zero-degree and the thirteen-degree flap angles. For the fifteen-degree pitch angle simulations, looking at the top surface of the blade, the zero-degree flap angle caused the highest stress which can be seen concentrated on the blade near where the blade meets the interior edge of the flap. The stress on the flap itself, however, remained relatively low and consistent for both the zero-degree and thirteen-degree flap angles. The bottom surface of the blade had slightly higher stresses for the thirteen-degree flap angle.

Looking at the thirty-degree pitch angle, the thirteen-degree flap angle resulted in the highest stresses on the top of the blade on both the blade and flap faces, with the greatest stresses concentrated at the consistent point where the blade meets the interior edge of the flap. The seven-degree flap angle resulted in the lowest stresses on the top of the blade and only slightly higher stresses on the bottom of the blade than those for the zero-degree flap angle. When choosing what parameter cases to run, a case with a seven-degree flap angle was added after original reports stated that a lower flap deflection would be more favorable than a higher one [10]. So, the results for this case show that a seven-degree flap angle was the optimal flap angle tested out of our parameter cases in the prevention of a high stress distribution across the blade. If further cases were to be run, several cases with flap angles above and below seven degrees should be run to see whether the most optimal flap deflection angle is above or below seven degrees. Also, it would be beneficial to see how the stress distribution with a seven-degree flap deflection angle would change at different pitch angles.

Lastly, examining each of the flap angles for the forty-five-degree pitch angle, there was a slight stress decrease as the flap changed from a zero-degree deflection to a thirteen-degree deflection. This change was relatively small, however, and one conclusion to draw from these results is that at a high enough pitch angle such as forty-five degrees, an increase in flap deflection does not impact the stress distribution of the blade.

Considering the combined impact of pitch angle and flap angle on the stress distribution and magnitude of the blade along with the magnitude of stress shown in the plots, we can confirm

that the least stress-inducing case from the seven cases run was the thirty-degree pitch angle and seven-degree flap angle, which echoes what the designers of the K-16B predicted. However, the lack of both number and variety of parameter cases ran for this analysis limits the reliability and accuracy of this statement. To confirm if a seven-degree flap angle results in the least induced stress, other flap angles between zero and thirteen degrees should be tested. Additionally, the seven-degree flap angle was only run at a thirty-degree pitch angle; running more cases at a seven-degree flap angle with varying pitch angles and adding more cases with a variety of pitch angles in general, would help us better understand the relationship between stress distribution on the blade and both pitch and flap deflection.

We also examined the impact of rotational velocity on stress. Case 1 was run without the imported pressure distribution from Fluent and with only the rotational velocity and fixed face applied, and the von Mises stress distribution is shown in Fig. 116.

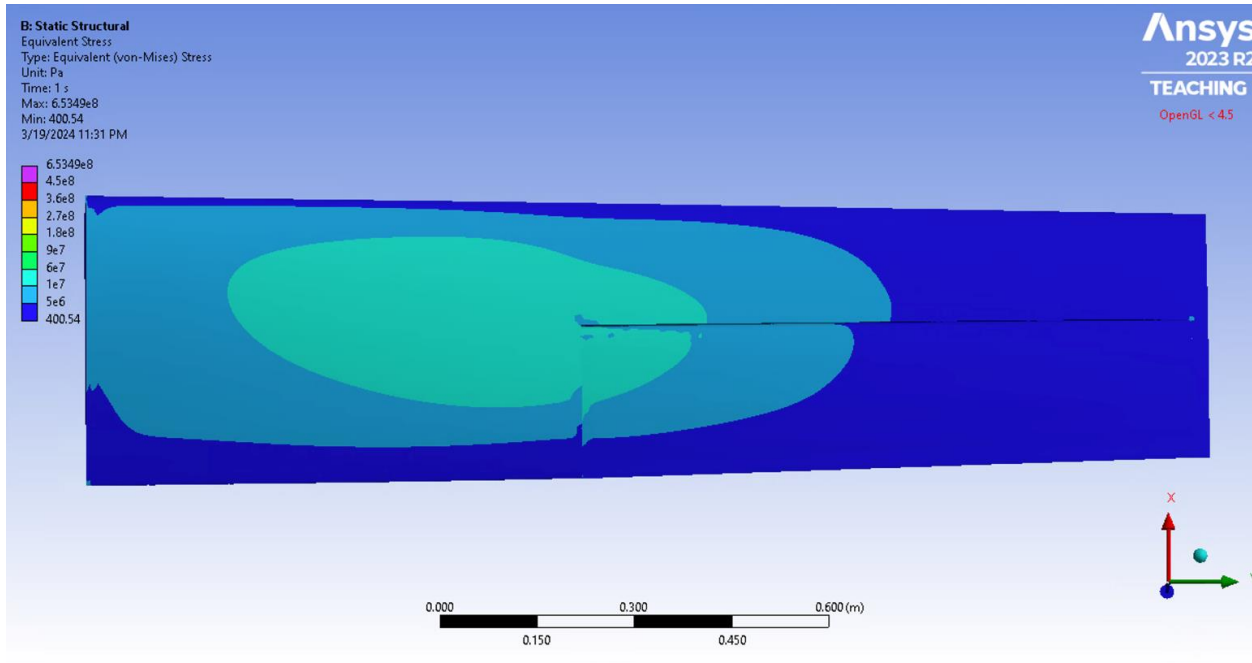


Figure 116: Von Mises stress results with no pressure applied for fifteen-degree pitch angle and zero-degree flap angle.

Comparing Fig. 116 with Fig. 96 which is the same case with both the rotational velocity and pressure distribution applied, a greater area of the blade surface is greater than 10 MPa in Fig. 116 with no pressure distribution than in Fig. 96 with the pressure distribution. This means that

the pressure distribution is inducing a more compressive stress on the blade; however, the blade remains at about the same magnitude of tensile von Mises stresses, meaning that the rotational velocity contributes most of the induced von Mises stress that the blade experiences.

As mentioned previously, these results are for the blade and flap made entirely of spruce, which was chosen over birch plywood since it is the heavier and therefore more conservative option. We can compare the resulting stress distributions to the yield stress of spruce found in *Aircraft Design* [27]; based on Fig. 89, spruce has a tensile yield strength of about 43 MPa and a compressive yield strength of about 28 MPa. Since all the von Mises stresses shown are positive, we need only use the tensile yield strength as a point of comparison. Examining the von Mises plots shown above, the stresses do not reach 43 MPa anywhere; the area of highest stress in Case 1 may contain a point of stress that surpasses 43 MPa, but with plot visibility and given that only the red contour which is up to 30 MPa is clear enough to see, any stresses in that area that could be higher than 43 MPa are negligible. So, the blade body and flap are structurally sound enough to take off in this structural analysis. Further, since we took the conservative approach of applying spruce to the blade and flap when, in reality, the blade is made of several types of lighter wood with a spar in its interior, this adds even more certainty that the blade body could withstand the induced stresses necessary for takeoff. However, we must also examine the rod.

It is important to note that the rod anchoring the flap to the blade consistently experienced the highest stresses for all cases. The structural analysis was run for a steel rod since we could not determine the precise metal material of which the rod was made. Ansys Static defines the structural steel material that was applied to the rod with a tensile yield strength of about 250 MPa. Based on Figs 95-108, all cases except for Case 2 show areas of stress that surpass this tensile yield strength. While these higher stress areas are sporadic and appear throughout the rod rather than being concentrated in one area, it is likely that the rod may experience plastic deformation. So, the K-16B would be unlikely to take off successfully for any case other than Case 2 due to the deformation and eventual failure of the rod in the blade.

The above conclusions are based solely on the materials that we assigned the model to best estimate the actual blade. However, it is likely that modeling the blade with its interior spar and

with the accurate materials would alter these results. With the impact that more accurate material assignment and model creation would have on the stress distribution, this could also impact the stress distribution on the rod.

7. Summary and Recommendations

The results and recommendations resulting from the various steps of this project are shared below.

7.1 Project Summary

As shown in the preceding sections, the team was unable to conclusively address the project's primary goal of determining whether the K-16B could have achieved takeoff in its V/STOL configuration. This was primarily due to the inability to capture many of the K-16B's unique design concepts in quantitative ways. The airflow around the rotoprops impacted by ground effect, in addition to the wing of the aircraft being completely in downwash air meant many of the parameters needed for the takeoff analysis could not be calculated within the scope of the project. After abandoning the analytical, classical takeoff analysis approach, the team decided to model the entire K-16B wing and rotoprop in a CFD simulation in Ansys Fluent to capture all the forces the team were unable to quantify. However, even assuming symmetry so only half of the wing and a single rotoprop needed to be modeled, the CAD model of the K-16B proved to be too large and intricate to be meshed in Fluent. The struggle to mesh this model coupled with the time constraint of the project, the team concluded that it would be unable to determine the takeoff ability of the K-16B using this approach.

After this conclusion was reached, the team shifted focus to performing a fluid and structural analysis on the rotoprop blades rather than the entire K-16B. This analysis would provide the results of a thrust force produced by the blades along with the stress distribution that each blade undergoes for a certain parameter case with a defined pitch angle and flap angle. After the CAD subteam created a model of a single blade and editing it as needed when meshing errors arose, seven different parameter cases, or seven different pitch and flap angle deflections, were run in Ansys Fluent and in Ansys Static to complete a fluid and structural analysis for each case. The thrust capabilities of the blade were able to be calculated for each of the seven parameter cases. The CFD analysis conducted in Fluent was also able to produce a pressure distribution over the entire blade, which was then imported into Ansys Static as a load on the blade. In Static, the von

Mises stress distribution over the blade was then able to be analyzed for each parameter case.

So, while the team was unable to determine the K-16B's takeoff capability through the duration of this project, several important analyses such as a thrust analysis and a stress analysis of the rotoprops blade was accomplished through the development of several CAD models, the debugging of Ansys mesh settings, and the created simulations in Ansys Fluent and Ansys Static in which the model was run. These results are pieces that can contribute to a future, more complete analysis of whether the K-16B could have taken off. Additionally, throughout the duration of the project, the team had adopted several plans of action to arrive at an answer to the question of the K-16B's ability to take off, some of which were unsuccessful. While the team did not achieve its primary goal using the analytical or CFD analysis, due to time constraints, it was able to conclude that the thrust produced by the rotoprops should have been sufficient for a hover, and hence likely a short-distance takeoff as well. In addition, these unsuccessful methods taught the team about 3D scanning, takeoff analysis, and other key aspects of the project process, and they also equip the team to provide significant recommendations that would assist any future engineers attempting to analyze the takeoff capability of the K-16B.

7.2 Project Recommendations

Our first set of recommendations pertain to our initial attempts to implement 3D scanning technology to create a CAD model of the rotoprops. This method was unsuccessful for our project goals because of a combination of issues including the size of the rotoprops blades and the aluminum coating of the blade. After further research, it was discovered that the Revopoint Pop 2 scanner was only designed for objects smaller than the rotoprops blade; Revopoint produces other scanners that are designed to scan larger objects. So, if attempting to implement 3D scanning of a larger object, we recommend using a scanner specifically designed for objects of that size. Additionally, when scanning an object that is aimed to be preserved in its original condition, we recommend using a spray like the AESUB spray described to create a uniform cast for the scanner to detect; while we were unsuccessful using this spray, this was still the best option to preserve the blade while attempting to scan it. It is reasonable to assume a better chance of success if using the

AESUB spray with a more fitting 3D scanner.

Our second set of recommendations pertain to our attempts to quantify the takeoff of the K-16B with equations. Because of both the ground effect due to the V/STOL configuration of the K-16B and the K-16B's wings being in downwash air of the rotoprops, we do not recommend attempting to quantify the takeoff through equations of any aircraft with one or both characteristics. Rather, after both research on analysis of downwash air and deliberation on the CFD analysis which was already needed to produce thrust capabilities and a pressure distribution, we decided to attempt running the full aircraft in a CFD analysis to capture the impacts of both ground effect and downwash air accurately. While our attempt at this method was unsuccessful due to meshing errors and time constraint, we nevertheless recommend using CFD analysis when analyzing ground effect or downwash air. However, it must be noted that attempting to model an entire aircraft and create a viable mesh is extremely time-consuming; so, we only recommend this method for a more long-term project or one without tight time constraints.

7.3 Team Recommendations

Several lessons can be drawn from the team's work on the K-16B analysis. There is a high volume of communication in a larger MQP team. Our team met multiple times weekly to discuss next steps for the project. This way, everyone can stay informed on the team's overall progress and can figure out how to contribute to the team most effectively.

The structural and fluid dynamics subteams both experienced many errors when trying to mesh the models. This caused many setbacks to the project schedule, as team members working in Ansys Static or Ansys Fluent would have to wait to receive an updated CAD model before the analysis could proceed. The CAD team should be physically present with the other subteams when Ansys simulations are first being run, as this allows for the subteams using the Ansys suite to request changes in the CAD models and rapidly receive updated models.

The CAD team ended up communicating frequently with the structural and fluid dynamics subteams, which showed that it is highly beneficial to determine the best path of clear

communication between subteams early in the project's timeline.

8 Conclusion

To conclude this project, the team was not able to determine if the K-16B was capable of V/STOL takeoff using the standard analytical takeoff analysis due to a lack of quantitative information regarding the propeller downwash and ground effects. The team tried using CFD to model half of the aircraft (symmetry could be assumed), but this proved to be impractical as well, primarily because of project time constraints and the complexity of the structure that needed to be meshed. However, the team was successful in performing a CFD analysis on a single rotoprop blade, from which it could infer the thrust of an entire rotoprop assembly (three blades) and therefore the thrust produced by two rotoprops on the aircraft. Accounting for the turning angle of the slipstream the K-16B's wing and full span flap provide in a hover, effective thrust was found to exceed the maximum weight of the aircraft. This leads the team to believe that the aircraft may have sufficient thrust for takeoff, but more analysis must be done. Despite the analytical difficulty in addressing the first project goal, the team was able to achieve several of the other project goals.

The team was able to evaluate the thrust capabilities of the rotoprops over seven different parameter cases, which was the second goal; while these results may not be applicable to the entire K-16B aircraft, the team was still able to determine the thrust force that a rotoprop blade produces for each case. This was accomplished by implementing CFD analysis in Ansys Fluent.

The team was also able to accomplish its third goal, which was to evaluate the induced stresses on the blade over a range of operating conditions. The team accomplished this goal by running a structural analysis in Ansys Static with the documented rotational velocity and the pressure distribution imported from the CFD analysis. The von Mises stress distribution was calculated for each of seven parameter cases.

The team achieved the goal of evaluating the efficacy of 3D scanning to create CAD models from parts; by attempting to use 3D scanning with test objects of various sizes and materials, they were able to analyze the drawbacks and shortcomings of 3D scanning for an object as large as a rotoprop blade on the K-16B. Because of these drawbacks and the subsequent decision to shift their method away from 3D scanning, they also concluded that attempting to fabricate any missing parts with 3D scanning would need to overcome the same issues described in this report.

The team also achieved its last goal, which was to provide team members with specialized software training. The CAD models that the necessary analyses required needed to be as detailed and comprehensive as possible. So, the CAD subteam became proficient in SolidWorks as models needed to be revisited, edited, and debugged. Completing both CFD and structural analyses called for detailed knowledge of how Ansys Fluent and Ansys Static perform these respective analyses. This knowledge was expanded upon as the subteams both dealt with extensive meshing and simulation errors. As a result, the team became extremely familiar with the Ansys suite and SolidWorks, and we gained proficiency in our skills with these software tools that will be useful for a variety of analysis types.

To conclude, valuable analysis and results were produced throughout this project; both the challenges encountered in aspects such as the K-16B's takeoff ability and implementing 3D scanning along with the successes of the CAD model creation, the CFD analysis, and the structural analysis contribute to many lessons learned and recommendations that can inform future engineers who attempt to further analyze the K-16B.

9 References

9.1 General References

1. *Advantages and Disadvantages of CAD*. (2021). Drexel University College of Computing & Informatics. Retrieved October 11, 2023, from <https://drexel.edu/cci/stories/advantages-and-disadvantages-of-cad/>
2. Basile, G., Fitzpatrick, J. E., & Zon, J. (1959). ESTIMATED FLYING QUALITIES OF THE KAMAN K-16B VTOL/STOL AIRCRAFT. The Kaman Aircraft Corporation.
3. Bell X-22 V/STOL Research Aircraft. Retrieved February 6, 2024, from: <https://aerospaceweb.org/aircraft/research/x22/>
4. Bennett, A. (2020, March 26). Point Cloud and 3D Image. Revopoint 3D Technologies Inc. <https://www.revopoint3d.com/point-cloud-and-3d-image/>
5. Bhaskaran, R. (2020, October). Wind Blade Analysis for wind power using Ansys fluent. Ansys Innovation Courses. <https://courses.ansys.com/index.php/courses/wind-blade-analysis-for-wind-power-using-ansys-fluent/>
6. Bowes, M. A. (1978). Engine/Airframe/Drive Train Dynamic Interface Document. Kaman Aerospace Corporation.
7. Boyer, A., Massari, A., Moore, J., Paszczuk, N. Raynowska, E., Tims, G., “Structural Design Analysis of the Burnelli CBY-3 Loadmaster and DC-3,” WPI Major Qualifying Project (MQP) Report 30931, Advisor: J. Blandino, 2023.
8. Chance-Vought/LTV XC-142A. National Museum of the United States Air Force [Internet]. Retrieved February 6, 2024, <https://www.nationalmuseum.af.mil/Visit/Museum-Exhibits/Fact-Sheets/Display/Article/195770/chance-voughtltv-xc-142a/>
9. Chen, H. (n.d.). Fundamentals of Finite Element Method. Retrieved November 18, 2023, from <https://pdhonline.com/courses/s272/s272content.pdf>
10. Egerton, H. S., & Fitzpatrick, J. E. (1967). THE MODEL K-16B V/STOL RESEARCH AMPHIBIOUS AIRCRAFT. Kaman Aircraft.

11. English, T. (2019). What is Finite Element Analysis and How Does It Work? Interesting Engineering. <https://interestingengineering.com/science/what-is-finite-element-analysis-and-how-does-it-work>.
12. "Finite Element Method." *Wikipedia*, 17 Feb. 2024. *Wikipedia*, https://en.wikipedia.org/w/index.php?title=Finite_element_method&oldid=1208377265.
13. Gao, Zizhen et al. Measurement of the Poisson's Ratio of Materials Based on the Bending Mode of the Cantilever Plate; *Bioresources*; 2016; 11(3):5703-5721.
14. Handheld 3D scanner light sources: Laser lines vs structured lights vs infrared. (2022, December 19). <https://www.shining3d.com/blog/handheld-3d-scanner-light-sources-laser-lines-vs-structured-light-vs-infrared/>.
15. How to Choose the Best 3D Scanner to Use With Your 3D Printer. (n.d.). Formlabs. Retrieved October 8, 2023, from <https://formlabs.com/blog/how-to-choose-a-3d-scanner-for-3d-printing/>.
16. ImageJ. Retrieved, February 13, 2024, <https://imagej.net/software/imagej/#:~:text=The%20original%20ImageJ%20has%20been,platform%20version%20of%20NIH%20Image>.
17. Introduction to Ansys Fluent: A beginner's guide to CFD simulation. (n.d.). MR CFD. Retrieved October 7, 2023, from <https://www.mr-cfd.com/introduction-to-ansys-fluent-a-beginners-guide/>
18. K-225 Kaman. (n.d.). New England Air Museum. Retrieved October 13, 2023, from <https://neam.org/pages/kaman>
19. Kaman: A legacy of innovation. (n.d.). New England Air Museum. Retrieved October 13, 2023, from <https://neam.org/pages/enhanced-kaman-exhibit>
20. Kaman K-16B. (2022). *Wikipedia*. https://en.wikipedia.org/wiki/Kaman_K-16B
21. Kaman K-16 in 40-by-80-foot Wind Tunnel [Internet]. NASA Ames Research Center; 1962. Available from: https://ails.arc.nasa.gov/images/ARCHIVE/legacy_scans/255-72-0711/box09/A-29884_folder/A-29884_jpg/highres/A-29884-2.jpg
22. Kaman K-16 in 40-by-80-foot Wind Tunnel [Internet]. NASA Ames Research Center; 1962.

Available from: https://ails.arc.nasa.gov/images/ARCHIVE/legacy_scans/255-72-0711/box09/A-29884_folder/A-29884_jpg/highres/A-29884-5.jpg

23. New England Air Museum. (n.d.). Retrieved October 1, 2023, from <https://neam.org/>
24. Noa(s) 56-549C. Air Systems Command, Department of the Navy; 1957.
25. Principles of Laser Triangulation | Learn About Machine Vision. (n.d.). Hermary. Retrieved October 6, 2023, from <https://hermary.com/learning/principles-of-laser-triangulation/>
26. Rapp, Bastian E. Chapter 31 - Finite Volume Method. *Microfluidics: Modelling, Mechanics and Mathematics*; Elsevier; 2017:633–54.
27. Raymer, D. (2018). *Aircraft Design: A Conceptual Approach (Sixth)*. American Institute of Aeronautics and Astronautics.
28. Revopoint Pop 2 3D Scanner. (n.d.). Retrieved October 7, 2023, from <https://www.revopoint3d.com/pop-3d-scanner-2/>
29. Scanningspray Vertriebs GmbH. (2022, February). Technical Datasheet - AESUB Blue. Recklinghausen, Germany.
30. Structural Analysis in Ansys: Guide to Choosing the Right Simulation Method. Skill-Lync. Retrieved December 9, 2023, from <https://skill-lync.com/blogs/structural-analysis-in-ansys-guide-to-choosing-the-right-simulation-method>
31. Understanding the Finite Element Method. The Efficient Engineer. Retrieved February 15, 2024, from <https://efficientengineer.com/finite-element-method/>.
32. Understanding Laser Scanners. (n.d.). FARO.Com. Retrieved October 6, 2023, from <https://www.faro.com/en/Resource-Library/Article/understanding-laser-scanners>
33. Understanding Inertial Loads—Lesson 5. (n.d.). Ansys Innovation Courses. Retrieved December 16, 2023, from <https://courses.ansys.com/index.php/courses/structural-boundary-conditions/lessons/understanding-inertial-loads-lesson-5/>
34. Wang, Jiehui et al. Application of 3D Laser Scanning Technology Using Laser Radar System to Error Analysis in the Curtain Wall Construction; 2023; 15(1):64-.

35. Wang, Tianxiang et al. In-Plane Mechanical Properties of Birch Plywood; Construction and building materials; 2022;340:127852-.
36. What Is 3D Laser Scanning Technology? [Internet]. 2018. Retrieved October 6, 2023, from <https://www.duncan-parnell.com/blog/what-is-3d-laser-scanning-technology>
37. What Is FEA | Finite Element Analysis? Documentation. SimScale. Retrieved February 19, 2024, from <https://www.simscale.com/docs/simwiki/fea-finite-element-analysis/what-is-fea-finite-element-analysis/>
38. “What Is Von Mises Stress in FEA? | SimWiki.” *SimScale*, <https://www.simscale.com/docs/simwiki/fea-finite-element-analysis/what-is-von-mises-stress/>. Accessed 20 Mar. 2024.
39. What materials are best for 3D scanning? (n.d.). Retrieved October 8, 2023, from <https://www.linkedin.com/advice/1/what-materials-best-3d-scanning-skills-3d-modeling>
40. Wojtas M, Czajkowski Ł, Szumański K. Ground Test Stands for Testing Rotors in Insulated Conditions. *Prace Instytutu Lotnictwa*. 2021; 1:15–23.
41. Ansys, “Ansys Customer Training Support Lecture 6 Turbulence Modeling,” imechanica.org, https://imechanica.org/files/fluent_13.0_lecture06-turbulence.pdf. Retrieved March 21, 2024.

9.2 NEAM Archive Sources

This project incorporated some of the original sources related to the Kaman K-16B program that NEAM possesses on-site. To properly reference these blueprints and other firsthand sources, Table 11 documents the archive location of the sources used in this report.

Reference Number	Box Number	Sheet Number	Item Number	Name of Document
[NA1]	1	1	14	Blade Assy. (Rotor)

				Sheet #1
[NA2]	1	1	15	Blade Assy. (Rotor) Sheet #2

Table 11: NEAM Archive Sources

Appendices

Appendix A: Takeoff Analysis MATLAB Code

```

clc; clear all; close all;
% Call all functions here:
takeoff_distance(80);
% Define all functions below:

%create curve fit of resultant force vs velocity

% lift and horiz_force can just run w arbitrary values - just trig

%function lift(velocity) %from data

%end
%function horiz_force = (velocity) %from data
%function takeoff_velocity
    % use fsolve with aircraft weight, either calculate here or import,
    % find velocity where L=W

function takeoff_distance(V_takeoff) %V_takeoff is the takeoff velocity in m/s

    % y = [v,x]
    tspan = [0 120]; % Set timespan
    y0 = [0, 0]; % Initial conditions [v0=0, x0=0]
    [t,y] = ode45(@myfunc,tspan,y0);

    x_positions=y(:,2)'; %Row vector of x positioions corresponding to t
    velocities=y(:,1)'; %Row vector of velocities corresponding to t

    %Display the results in the command window
    takeoff_index=find(velocities>=V_takeoff, 1, 'first');
    disp(['Takeoff time: ', num2str(t(takeoff_index)), 's'])

```

```
disp(['Takeoff distance: ', num2str(x_positions(takeoff_index)), 'm'])

%Uncomment below to plot results
% figure
% grid on
% xlabel("Time [s]")
% yyaxis left
% plot(t,velocities)
% ylabel("Velocity [m/s]")
% yyaxis right
% plot(t, x_positions)
% ylabel("Displacement [m]")
% legend("velocity", "x displacement", 'location', 'northwest')
end
```

Appendix B: Preliminary Design of the Translational Tripod for Blueprints (TTB)

One of the issues the team had was taking pictures of the blueprints in the most efficient way due to the size. The idea to start the design of a “Photo Rig” or a “translational tripod for blueprints (TTB)” was to make it easier for other MQP teams in the future to take pictures of large-format documents or blueprints. The TTB will have a camera attached to it that will be able to slide on the stand so that even hidden pictures or nomenclature in the corner of the blueprints can be captured with ease.

SOLIDWORKS was used to create the design of the lower assembly. The full assembly is divided into two assemblies, one assembly for the top frame and one assembly for the two side legs.

The top frame consists of four pieces with the first piece being the long horizontal piece and vertical piece which serve as the basic structure. These parts are the T-slotted framing rails from McMaster-Carr (part # 47065T101). The horizontal piece is 42 inches in length (3.5 ft) while the side piece is 12 inches (2 ft) in length. These pieces were mated together on SOLIDWORKS, and the structural brackets are then mated to those pieces. On the top left and right of the top frame, the 90-degree angle surface bracket for single rail is used which is in an L-shape. These are used to connect the horizontal and vertical pieces together. The tee surface bracket for single rails is connected to the bottom left and bottom right. The way the structural brackets are attached will be through screws that slide into the rails and can be screwed into the piece. The structural brackets are connected in such a way that they partially overhang; this is done so that the top part can be clamped down onto the side legs and connected. The reasoning behind doing this was to be able to disassemble this lower structure into three separate assemblies; the top frame and two side legs so assembly and disassembly can be done with ease. To ensure rigidity among the T-slotted framing on top, corner brackets were also added to the corners on the insides of the rails.

The second assembly is for each of the side legs. The side leg assembly consists of the T-slotted framing rails, extended corner brackets, and casters. The structure is similar to the top frame however structural brackets are not used. The top T-slotted framing rail is 26 inches and connects to the 16-inch-long vertical T-slotted rails because of the extended corner brackets which are located on the inside corners. The second horizontal piece was initially going to be placed in the middle of the side legs; however, it was decided that moving it to the bottom was better so that the structure could have more stability. The final piece of the side leg was to attach the casters at the bottom. The casters chosen are rigid so that they don't rotate

but allow for translation in one direction as needed. The side legs are mated with the top assembly so that the top assembly sits on top of the legs and can be connected by screws.

Two single rail sliding sleeve bearings (McMaster-Carr part # 60585K35) are added to the middle of the horizontal T-slotted framing rails on the top assembly across from each other. These pieces will slide along the top frame to allow the camera to be positioned at different angles to take pictures once the design of the final, top part of the structure is finalized. The last piece that the model included was the double T-slotted framing rail which is connected by the ends to the sleeve bearings on top. This was chosen instead of the single T-slotted framing rail because the camera mount and stand will be heavy and also because it allows the rail to be connected to the ends of the bearings. The double T-slotted framing rail specifications were chosen to be 1.5 x 1.5 to meet that requirement. Figure 117 shows the completed, lower assembly design of the TTB.



Figure 117: Alternate View of Model with Mount

The camera mount and stand will be designed as part of a future MQP; they were included in the initial

design, but the focus later switched to completing design of the lower portion of the TTB assembly, with the slides and double T-slotted framing. The model above was the preliminary design, this provides the MQP team next year with a starting point. The continuation of this will be to add the camera mount, that will be the last piece of the model before it can be used to capture pictures of blueprints at NEAM.